Stress-driven melt segregation and reactive melt infiltration in partially molten rocks deformed in torsion with applications to melt extraction from Earth's mantle

A DISSERTATION
SUBMITTED TO THE FACULTY OF THE GRADUATE SCHOOL
OF THE UNIVERSITY OF MINNESOTA
BY

Daniel S. H. King

IN PARTIAL FULFILLMENT OF THE REQUIREMENTS
FOR THE DEGREE OF
Doctor Of Philosophy

October, 2010

Acknowledgements

I am grateful to David Kohlstedt for his personal generosity, wise guidance on the research path presented here, and for creating a world-class laboratory and research group of which I have been fortunate to be a part for the last several years. All of the work I have done follows in some way from earlier generations of experiments (mostly by former members of the group). David's leadership keeps the lab a friendly, cooperative place of vibrant discovery. Hopefully I have done my part to inspire the next set of experiments.

Mark Zimmerman deserves a great deal of credit for the experiments I was able to perform. His patience in the face of a constant barrage of questions keeps the lab running. Mark is the holder of much institutional memory of laboratory tricks and of scientific ideas that have percolated through the lab.

I owe Ben Holtzman many thanks for his help and generosity providing me with a basis of methodology from his previous work, which was the foundation for the work of Chapter 2. Input from his unique perspective has been valuable in all parts of this work. Our collaborations now go beyond the deformation of partially molten rock, and I hope we are able to continue working together well into the future.

Sash Hier-Majumder has been a key collaborator and teacher with his contributions to the comparison of the annealing data with the formulation for surface tension driven flow that he developed with Yasuko Takei. I learned a great deal from our conversations and correspondences.

I have benefited greatly from the cooperative atmosphere in the lab and have recieved a lot of help from my fellow graduate studentes: Amanda Dillman, Lars Hansen, Lauren Larkin, Stephen Schneider, Yang "Will" Li, and Qi Chao; and from post-docs and researchers Ayako Suzuki, Marshall Sundberg, Sylvie Demouchy, Take Hiraga, and

Shengua Mei. I have also been fortunate to work with two undergraduate summer interns while at Minnesota, Kristin Rodzinyak and Kimberlin Schnittker.

I appreciate the guidance and advice provided by all my committee members: David Kohlstedt, Marc Hirschmann, Peter Hudleston, Ben Holtzman, and Martin Saar.

I am grateful for the support of my family, especially my parents, Robert and Jane King; my wife, Anna Henderson; and the new addition to our family Walter Henderson-King.

I also would like to thank all of the organizations that helped fund my time as a PhD student. I have benefited from NSF support through grants awarded to David Kohlstedt. The University of Minnesota Department of Geology and Geophysics has provided generous support in the form of fellowships and research expenses. In particular, I would like to note the the Harold Mooney Fellowship, the V. Rama Murthy/Janice Noruk Fellowship, and the Richard Clarence Dennis Fellowship. A graduate student research grant from the Geological Society of America provided travel support for collaborations with Ben Holtzman. A Doctoral Dissertation Fellowship from the University of Minnesota is gratefully acknowledged for funding the final year of my PhD research.

Abstract

Melt extraction from Earth's upper mantle requires transport of magma from regions of partial melting at depth to the Earth's surface. During its ascent, melt interacts chemically and mechanically with the rock matrix. Melt reduces the viscosity of the partially molten rock compared to that of a melt-free rock. This weakening is a potential mechanism of strain localization that could have significant geodynamical implications. Magma interacts chemically with mineral phases during its ascent, dissolving phases in which it is undersaturated and precipitating phases in which it is oversaturated. Such melt-rock reaction can be a driving force for melt migration. Water and other volatiles also partition into the melt from minerals and are then expelled to Earth's oceans or atmosphere. This process leaves behind stronger dehydrated rocks, and it could be the mechanism by which the oceanic lithosphere (mechanical boundary layer) is formed.

The work presented here is an experimental investigation of several mechanisms that influence the distribution of melt within a viscously deformable partially molten rock. The experiments make use of the torsion geometry, which is a relatively recent addition to techniques used in studies of high-pressure, high-temperature deformation of Earth materials. Three mechanisms are considered, either alone or in various combinations. (1) An applied shear stress causes melt to align and segregate into melt-rich bands with a consistent geometrical relationship to the shear geometry. In Chapter 2, we investigate possible means of scaling the bands that form in experimental samples to Earth's mantle and explore the evolution of melt-rich bands at high shear strain. (2) Interfacial tension driven flow acts to homogenize the distribution of melt within a partially molten sample. Flow of melt, driven by the minimization of interfacial energy within the system, must be coupled with corresponding flow of the solid through compaction/decompaction of the matrix or diffusive transport of matter through the liquid

phase (dissolution/precipitation). In Chapter 3, we investigate the evolution of melt distribution during static annealing of a sample that was previously deformed and in which melt-rich bands developed in response to the shear deformation. We compare the experimental results with models of interfacial tension driven flow to determine which mechanisms control the rate of melt redistribution. (3) A melt source that is undersaturated in some component, when coupled with a sink that is rich in that component, will infiltrate into the sink through reactive flow. This reactive flow can develop into an instability in which fingers of high melt fraction propagate into the sink. In Chapter 4 we investigate this process under static conditions, and we investigate the interactions of this process in combination with stress-driven melt segregation.

Contents

List of Tables

List of Figures

Chapter 1

Introduction

Many fundamental questions in the Earth sciences involve how the flow of material and heat within the mantle is manifested near Earth's surface as the motion of lithospheric plates. These questions include: To what degree are the mantle and crust divided into chemically and/or mechanically distinct layers? How are these layers coupled and how are forces transmitted from one layer to another? How does the rheology of the mantle and crust vary through space and time and what controls these variations? While most of the mantle is believed to be nominally melt-free, and regions containing melt only have small amounts (typically $< 2\%$), the physical properties of partially molten rocks control deformation styles and melt extraction processes at some of the most active plate-tectonic settings — mid-ocean ridges, hot spots, and subduction zones — and therefore play a key role in controlling lithosphere-asthenosphere dynamics. The goal of this dissertation is to investigate fundamental processes involving the interactions among deformation, melt-rock reaction, and surface tension in controlling the evolution of melt distribution and strain localization in partially molten rocks. These observations will help us understand processes through which melt is extracted from Earth's mantle and what role melt extraction plays in facilitating plate tectonics.

1.1 Melt-migration in Earth's upper mantle

Nearly all new oceanic crust is created at mid-ocean ridges from the eruption of magma generated in the upper mantle. The oceanic lithosphere (mechanical boundary layer)

then migrates away from oceanic spreading centers until it is subducted back into the mantle. While the degree of coupling between the mechanical boundary layer and the underlying asthenosphere is under debate (e.g Fischer et al., 2010), leading theories for the formation of 'plates' involve both the direct effects of melt on rock strength and the effects of melt extraction on the strength of the residual rock. The viscosity of olivine is observed to be dramatically reduced by the presence of water within the mineral structure (Hirth & Kohlstedt, 1996). When melt is present, water partitions from the mineral grains into the melt, thus dehydrating the olivine. In this way, melt extraction from the mantle creates a chemical boundary layer of water-depleted mantle that is much stronger than the underlying water-rich mantle. This chemical boundary layer could directly correspond with the mechanical boundary layer. It is also possible that melt is more directly involved in the decoupling at the lithosphere-asthenosphere boundary. Seismic observations point to possible evidence that horizontal melt-rich layers are present along the lithosphere-asthenosphere boundary, which could act as low viscosity layers accommodating strain localization (Kawakatsu et al., 2009).

Understanding mechanisms of melt extraction and the processes that control melt distribution within the upper mantle is critical to evaluating these theories of lithosphere-asthenosphere decoupling. Multiple lines of evidence indicate that melt does not always travel through the mantle by evenly distributed percolation along grain boundaries as it is extracted from the upper mantle. Geochemical evidence indicates that mid-ocean ridge basalt (MORB) is not in chemical equilibrium with upper mantle peridotite. MORBs are under-saturated in pyroxene compared to the equilibrium melt composition at the base of the oceanic crust even though pyroxene is present throughout the column the melt must have traveled through (Stolper, 1980; Elthon, 1983). Additionally, the ratio of light-to-heavy rare earth elements is higher in MORB than in dredged samples of abyssal peridotite (Johnson et al., 1990; Johnson & Dick, 1992) or in samples from ophiolites (Kelemen & Dick, 1995). These observations demonstrate that melt must be organized into channels so that it can travel through $\sim$ 40 km of the mantle without equilibrating with its surroundings. Evidence for channelized melt flow has been documented in many ophiolites. Dunite ($>$ 90% olivine) is a minor component of most ophiolites and is widely recognized to be a depleted zone representing melt pathways.

Primarily occurring as a network of interconnected tabular dikes, dunites could represent the required melt channels. Dunite in the Oman ophiolite has been extensively studied (e.g., Ceuleneer et al., 1988; Boudier et al., 1988; Nicolas & Boudier, 1995; Boudier et al., 1996; Braun & Kelemen, 2002). Using mosaics of air photos and structural data from the Oman ophiolite Braun & Kelemen (2002) demonstrated that the abundance of dunite dikes displays a power law dependence upon width, which ranges from 1 cm to 100 m. Structural analysis of the Josephine peridotite in southwest Oregon also reveals an interconnected network of dunite dikes (Kelemen & Dick, 1995). Dunites in the Josephine peridotite appear to have a syn-tectonic origin, suggesting that melt flowed through actively deforming shear zones.

One mechanism for channelized flow in a porous medium is a reactive infiltration instability process, which is important in a variety of geological processes such as groundwater flow, petrofluid extraction, and magma transport. A reactive instability involving the dissolution of pyroxene has been proposed for melt channel formation in Earth's mantle (Aharonov et al., 1995, 1997; Kelemen et al., 1995; Spiegelman et al., 2001). Because the solubility of pyroxene in melts increases with decreasing pressure, dissolution increases as melt migrates upward, thus increasing the permeability and the melt flux. Reactive infiltration has been demonstrated experimentally in samples in which a source of pyroxene-undersaturated melt is coupled with a pyroxene-rich sink (Daines & Kohlstedt, 1993, 1994; Morgan & Liang, 2003, 2005).

Melt segregation due to an applied stress is another mechanism for the formation of high permeability pathways. Experiments have demonstrated the emergence of patterns in melt distribution when a partially molten rock is sheared (e.g., Zimmerman et al., 1999; Holtzman et al., 2003; Holtzman & Kohlstedt, 2007). Shear stresses causes the melt pockets to align and, in some cases, segregate into an anastomosing network of melt-rich bands angled antithetic to the shear direction that surround lenses of melt-depleted rock. The result is a transformation from an isotropic, homogeneous aggregate to one in which the phase distribution, permeability, and viscosity are highly anisotropic and heterogeneous. Strain is concentrated in melt-rich bands because of a viscosity reduction in regions of elevated melt fraction. The melt-rich bands also provide high-permeability pathways through which melt can migrate more rapidly than by evenly distributed melt percolation. Permeability models presented by Holtzman et al. (2003)

applied to samples of olivine + chromite + 6% melt estimate that the permeability is three orders of magnitude greater parallel to the bands then perpendicular to the bands ($k = 5 \times 10^{-14}\,\mathrm{m}^2$ vs $5 \times 10^{-17}\,\mathrm{m}^2$). For comparison, the model predicts a permeability for a homogeneous material of the same composition of $k = 1 \times 10^{-15}\,\mathrm{m}^2$. This analysis reveals that stress-driven melt segregation creates a highly anisotropic permeability structure in partially molten rocks and that melt can flow at a greater velocity parallel to melt bands than it would during distributed flow.

1.2 Background

1.2.1 High-temperature creep

Deformation of mineral aggregates at high pressure and high temperature is accommodated by diffusion of ions (via a point defect, vacancy, or interstitial mechanism), by glide and climb of line defects (dislocations), and by sliding on planar defects (subgrain and grain boundaries). Ductile flow occurs through a change in shape of grains and relative movement of grains without volume change or the formation of void space. Steady state inelastic deformation can be described by a constitutive equation that describes the strain rate $\dot{\varepsilon}$, in terms of an applied differential stress σ, temperature T, pressure P, grain size d and oxygen fugacity f_{O_2}. In aggregates of olivine, this flow law is typically of the form

$$\dot{\varepsilon} = A\frac{\sigma^n}{d^r} f_{O_2}^m \exp\left(\frac{-(Q+PV)}{RT}\right), \tag{1.1}$$

where A is a material parameter, Q is the activation energy, V is the activation volume, and R is the gas constant. The exponents m, n, and r depend upon the creep mechanism. In the dislocation creep regime, $n = 3.5$ and $r = 0$. In the grain boundary sliding regime, $n = 3.5$ and $r = 2$. In the diffusional creep regime, $n = 1$ and $r = 1$, 2 or 3 when interface reactions, lattice diffusion, or grain boundary diffusion, respectively, controls the creep rate.

1.2.2 Rheological properties of partially molten rock

The presence of melt enhances the strain rate in both the diffusion and dislocation creep regimes. The two primary ways in which melt influences rock strength are (1)

reduced contact area between grains that leads to increased local stress and (2) faster pathways for diffusion. Cooper & Kohlstedt (1984b), Cooper & Kohlstedt (1986), and Cooper et al. (1989) demonstrated that this enhancement is fundamentally dependent upon how melt is distributed, and they developed a model to describe melt enhanced diffusion creep with the addition of a term to the flow law (Equation 1.1) that is a function of the dihedral angle

$$\dot{\varepsilon}_{\phi} \propto \dot{\varepsilon}_{\phi=0} \left(1 - \frac{\Delta d}{d}\right)^{-2}_{\text{stress}} \left(1 - \frac{\Delta d}{d}\right)^{-2}_{\text{diffusion}} \tag{1.2}$$

where d is a characteristic grain boundary diffusion distance and Δd is the proportion by which that distance is shortened due to the presence of melt at triple junctions. The two terms account for strain rate enhancement due to increased local stresses and increased diffusive mass transfer. The term $\Delta d/d$ is a function of both dihedral angle and melt fraction

$$\frac{\Delta d}{d} = 1.05 f(\theta) \phi^{1/2} \tag{1.3}$$

where

$$f(\theta) = \sin(30^\circ - [\theta/2]) \left[\frac{1 + \cos\theta}{\sqrt{3}} - \sin\theta - \frac{\pi}{90}(30^\circ - [\theta/2])\right]^{-1/2}. \tag{1.4}$$

Experiments by Hirth & Kohlstedt (1995a,b) demonstrated that the enhancement was greater than expected at melt fractions greater than ~ 0.05. They suggested that when $\phi > 0.02$ melt is no longer restricted to triple junctions, and a significant amount of melt is present along grain boundaries. Melt along two-grain interfaces provides additional pathways for diffusion not accounted for in the Cooper-Kohlstedt model. Hirth & Kohlstedt (1995a,b) proposed a modified version of the Cooper-Kohlstedt model to take the increased diffusion pathways into account that fits the rheological data at melt fractions up to $\phi \approx 0.15$. It was subsequently demonstrated by Mei et al. (2002) that this formulation provided a good fit to rheological data from samples of partially molten olivine deformed in the presence of water. It takes the form

$$\dot{\varepsilon}_{\phi} \propto \dot{\varepsilon}_{\phi=0} \left(1 - \frac{\Delta d}{d}\right)^{-2n}_{\text{stress}} \left[\left(1 - \frac{\Delta d}{d}\right)(1 - \beta\phi)\right]^{-2}_{\text{diffusion}} \tag{1.5}$$

where $\beta\phi$ is the fraction of two-grain boundaries that are completely wetted by melt. In the diffusion creep regime $n = 1$, so the first term (local stress enhancement) is

equivalent to the Cooper-Kohlstedt model. The second term is modified to account for short-circuit diffusion pathways along wetted two-grain interfaces. When this model is applied to the dislocation creep regime, the diffusion term is removed and $n = 3.5$.

An empirical exponential dependence of the viscosity of olivine-rich partially molten rocks on the melt fraction was proposed by Kelemen et al. (1997). This relationship takes the form

$$\eta = \eta_0 \exp(-\alpha\phi), \tag{1.6}$$

where η_0 is the viscosity in the absence of melt. Kelemen et al. (1997) determined that $\alpha = 45$ based on a compilation of data in both the dislocation and diffusion creep regimes. More recently Mei et al. (2002) determinted that $\alpha = 26$ for the diffusion creep regime and $\alpha = 31$ for the dislocation creep regime.

1.2.3 Melt distribution

The exponential dependence of viscosity on melt fraction in Equation 1.3 applies to a homogeneous melt distribution, but several factors influence how melt is distributed within a partially molten rock. The following sections summarize the effects of deformation and interfacial tension in creating pressure gradients within the fluid phase that can result in melt flow.

Influences of Deformation on Melt Distribution

Examples of homogeneous, but anisotropic, melt distribution have been observed in both triaxial and simple shear deformation experiments on olivine-rich rocks (e.g., Daines & Kohlstedt, 1997; Zimmerman et al., 1999). Bussod & Christie (1991) showed that melt pockets aligned $\sim 30^\circ$ from the maximum principle stress in triaxial deformation experiments on partially molten lherzolite. Observations from samples of olivine + MORB deformed in simple shear reveal that melt pockets preferentially align $\sim 20^\circ$ to the shear plane (Kohlstedt & Zimmerman, 1996; Daines & Kohlstedt, 1997; Zimmerman et al., 1999). Similar alignment of melt relative to applied stresses has also been documented in experiments on granitic rocks (e.g., DellAngelo & Tullis, 1988; Rutter & Neumann, 1995).

The theoretical framework anticipating melt segregation in response to shearing at length scales greater than the grain size was first presented by Stevenson (1989). He developed a model of a fluid dynamical instability in which a homogeneously distributed partial melt in a deforming matrix is demonstrated to be unstable due to the decrease in viscosity of the matrix with increasing melt fraction. He argued that the liquid pressure is lower in regions of higher melt fraction. Because melt will flow to regions of low pressure, more melt will continue to accumulate where it is already concentrated. This instability leads to an amplification of existing variations in melt fraction.

Experiments have since confirmed that stress-driven melt segregation can occur in deforming partially molten rocks. In samples in which the compaction length (defined below) is less than the length of the sample, melt segregates into distinct melt-rich bands (Holtzman et al., 2003). Once formed, melt bands are angled an average of $\sim 20^\circ$ to the shear plane, antithetic to the shear direction.

Holtzman et al. (2003) demonstrated that the width and spacing of melt-rich bands scales with the compaction length, δ_c, a characteristic length scale in two-phase flow theory. Band spacing is greater and bands are thicker with increasing δ_c. The compaction length is the distance over which the compaction rate decreases by a factor of e, or the distance over which a viscously deformable porous solid matrix can sustain gradients in melt fraction (McKenzie, 1984). It is given by

$$\delta_c = \left(\frac{\xi + 4/3\eta}{\mu} k_\phi \right)^{1/2}, \tag{1.7}$$

where ξ and η are the bulk and shear viscosities of the matrix, k_ϕ is the permeability of the rock, and μ is the dynamic viscosity of the melt.

Parallel to these experimental studies, many theoretical studies have investigated the process of stress-driven melt segregation and its implications for Earth. Melt-rich band formation was modeled in simple shear by Spiegelman (2003) and Rabinowicz & Vigneresse (2004). Spiegelman's 2-D linear analysis concluded that melt-rich bands oriented 45° to the shear plane grow fastest, bands rotate passively with increasing strain and bands at an angle $> 90^\circ$ to the shear plane decay. No preferred wavelength for growth rate of melt-rich bands, greater than a compaction length, was found in the linear analysis. Katz et al. (2006) expanded on the linear analysis of Spiegelman (2003) to include the effects of strain-rate weakening with a power-law rheology in addition

to weakening due to increased melt fraction. They demonstrated that, with a stress exponent of $n > 4$, the low angle bands observed in experiments could be numerically simulated. This stress exponent is inconsistent with experimental data, but the authors point out that other nonlinear effects involved with band realignment might lead to a lower band angle for a given stress exponent. A steady-state analysis of viscous energy dissipation presented by Holtzman et al. (2005) concluded that a band angle of $\sim 20^\circ$ is a favorable configuration that minimizes stress differences between band and non-band regions and corresponds to a minimum in viscous energy dissipation. Recently, Takei & Holtzman (2009a,b) presented a model for deformation of partially molten rocks that incorporates contiguity of melt as an internal state variable. They demonstrated that low angle bands can be explained by melt-weakening and viscous anisotropy, without considering a power-law viscosity.

Influences of Interfacial Tension on Melt Distribution

Competing with melt segregation processes is surface tension driven flow, which acts to redistribute melt evenly. A surface energy exists at any grain boundary due to the difference between cohesion (attraction between molecules within the crystal) and adhesion (attraction between molecules of different phases across the grain boundary). The distribution of melt within a granular medium, under hydrostatic conditions, is determined by the relationship between solid-solid γ_{ss} and solid-melt γ_{sm} interfacial energies. The dihedral angle θ, the angle at which solid grains intersect, can be measured in partially molten samples. It is defined as $\cos\theta/2 = \gamma_{ss}/2\gamma_{sm}$. For materials with $0^\circ < \theta \leq 60^\circ$ (as is the case for olivine and the majority of mantle phases), melt is contained within tubes along three- and four- grain junctions that form a fully interconnected network. When $\theta < 60^\circ$, spatial variations in melt fraction lead to a pressure gradient within the melt, with low melt fraction corresponding to low pressure (Stevenson, 1986). Thus, under static conditions, melt fraction perturbations are smoothed out according to a non-linear diffusion equation.

Because interfacial energies contribute to the free energy of the system, and interfacial energies vary spatially when melt fraction varies, melt homogenization can be treated as an energy minimization problem. Melt flows to reduce the overall free energy, but the flow is resisted by matrix compaction/decompaction. That is, any melt flux must

be accompanied by a corresponding solid flux through viscous flow. Based on theory for compaction driven flow in deforming porous media presented by McKenzie (1984), Riley et al. (1990) and Riley & Kohlstedt (1991) developed a model for melt transport in partially molten rocks driven by capillary forces. Similar models have subsequently been developed by Bercovici & Ricard (2003) and Hier-Majumder et al. (2006). These models can be formulated to account for the effects of melt on the viscosity of the solid through (1) reduced contact area between grains and (2) melt-assisted diffusive transport of mass at the grain scale (e.g., Riley & Kohlstedt, 1991, Appendix B). However, no mass exchange driven by a difference in chemical potential between solid and liquid for any component of the system is allowed, and the overall volume of melt is held constant. An extension of this formulation for interfacial tension driven flow presented by Takei & Hier-Majumder (2009) includes terms for mass exchange between solid and liquid through dissolution/precipitation, and for diffusive flux of the component being exchanged through the liquid phase. The dissolution/precipitation is driven by gradients in surface tension through the Thomson-Fruendlich effect. In the formulation of Takei & Hier-Majumder (2009), two separate mechanisms of interfacial tension driven flow – compaction/decompaction (viscous flow of the matrix) and dissolution/precipitation (diffusive transport of mass through the liquid phase) – can be considered to be acting in parallel. The analysis presented by Takei & Hier-Majumder (2009) suggests that at long perturbation length scales and small grain size compaction/decompaction is the dominant process, while at short perturbation length scales and large grain size dissolution/precipitation is the dominant process.

1.3 Torsional deformation

A variety of different deformation geometries exist for testing mechanical properties of materials. Specific geometries, and apparatuses, are most appropriate for exploring different materials or for exploring various properties of the same material. The gas-medium deformation apparatus has been used for several decades in the Earth sciences, primarily in a triaxial deformation geometry (with confining pressure providing two of the three principle stresses) (Paterson, 1990). While capable of modest confining pressures compared to solid medium deformation apparatuses, the high precision of load

and displacement data measured by load cells, strain gauges, and LVDTs housed inside the pressure vessel has lead to well-constrained parameters in olivine flow laws along with many other important discoveries about the physical properties of Earth materials. Compressional deformation is not, however, well suited to deforming samples to high strain. Finite strain is typically limited to ~ 0.2. Also, the limitation to pure-shear deformation does not allow exploration of many interesting phenomena associated with simple-shear deformation such as crystallographic alignment with the shear direction and stress-driven melt segregation.

Angled pistons can be used in a triaxial compression apparatus to produce shear deformation in the direct shear geometry. This method was used by Holtzman et al. (2003) to investigate stress-driven segregation. Though much higher strains can be achieved than in triaxial compression, direct shear samples can only be deformed to $\gamma \approx 3$ before the sample loses contact with the pistons over a significant area of the sample.

Though used in many other materials testing applications, the torsion test is relatively new to high-pressure, high-temperature deformation of Earth materials (Paterson & Olgaard, 2000). The most dramatic benefit of the torsion geometry over previously available methods of inducing shear deformation is the ability to deform samples to extremely high strain. Samples can be deformed to theoretically unlimited strains. Samples can also be significantly larger in torsion than in direct shear (5 mm thick compared to 0.5 mm thick in direct shear). Further, gradients in stress, strain, and strain rate exist within the torsion specimen making it possible to explore a wide range of parameter space in one experiment (though these gradients can also add unwanted complexity to some experiments).

The chapters in this dissertation all take advantage of different aspects of the torsion geometry in order to explore processes that were out of reach using previously available methods. In Chapter 2, we explore the microstructural evolution of partially molten samples to higher finite strains than in any prior study. In Chapter 3, we take advantage of the large size of torsion samples in order to improve the methods for studying the rate of homogenization of perturbations in melt fraction due to surface tension driven flow. In Chapter 4, we use a variety of innovative deformation geometries involving nested cylinders of source and sink material taking advantage of large sample size and

the variability of stress, strain, and strain rate within the sample.

1.4 Outline of work presented here

Chapter 2 is a paper that was published in January 2010 in a special volume of the *Journal of Petrology – Shallow Mantle Composition and Dynamics: Fifth International Orogenic Lherzolite Conference*. The conference was held in Shasta City in September 2008 and was sponsored as a Chapman Conference by the American Geophysical Union (AGU). This chapter presents a series of torsion experiments designed to explore the effects of stress and strain on the process of stress driven melt segregation. Prior studies (Holtzman et al., 2003; Holtzman & Kohlstedt, 2007) have indicated that band spacing and thickness scale with compaction length. The torsion samples provide a rich data set on band spacing, thickness and angle to shear plane. In general, the study confirms prior results that band spacing is $\sim 0.2\delta_c$. The results from high strain samples provide a new look at how band networks may evolve, and how strain localization into melt-rich shear zones progresses at high strain.

Chapter 3 is a paper that will be submitted to *Earth and Planetary Science Letters* on the effects of surface tension driven flow in homogenizing perturbations in melt fraction within a partially molten sample. The goal of this chapter is to provide constraints on the role of surface tension driven flow as a competing process occurring simultaneously with stress-driven melt segregation, and as a process to dissipate bands after they were created. In collaboration with Dr. Saswata Hier-Majumder, the experimental results are compared with the recently developed model of Takei & Hier-Majumder (2009). The results of this study build upon prior studies by Riley et al. (1990), Riley & Kohlstedt (1991), and Parsons et al. (2008). They allow us to more confidently extrapolate surface tension driven flow to conditions in Earth's upper mantle

Chapter 4 is a paper on a series of experiments designed to explore the relationships between two known processes that can lead to the formation of melt-rich channels in a partially molten rock. One mechanism is the stress-driven melt segregation explored in Chapter 2, the other mechanism is a melt infiltration instability that occurs due to the solubility of orthopyroxene in a silica-undersaturated basalt. Several different

methods of coupling a melt-rich source with a melt-free (or melt-poor) sink were employed. The result is the first experimental evidence for the interaction between these two mechanisms of melt segregation/migration acting simultaneously. The experiments provide evidence that stress-driven melt segregation is an effective way to create the perturbations in melt fraction that are necessary for the initiation of the infiltration instability.

In Chapter 5 I present a final discussion of the analyses presented in the dissertation and outline promising future directions to pursue based on the results from this body of work.

Chapter 2

Stress driven Melt Segregation in Partially Molten Olivine rich Rocks Deformed in Torsion

This chapter has been published in the *Journal of Petrology*, vol. 51 (1-2) pp. 21-42 (2010) with co-authors Mark E. Zimmerman and David L. Kohlstedt and is used in this dissertation with permission from the Oxford University Press.

Torsion experiments on partially molten aggregates of olivine + chromite + 4 vol. % mid-ocean ridge basalt provide new insights into the interactions between deformation and melt segregation. When samples are sheared, melt segregates into distinct melt-rich bands oriented $\sim 20^{\circ}$ antithetic to the macroscopic shear plane. In one series of experiments, samples were deformed at similar shear strain rates (or stresses) to a range of finite shear strains to explore the evolution of melt-rich bands. In another series of experiments, samples were deformed to similar finite shear strains at a range of strain rates to explore the effect of strain rate (or stress) on band spacing and microstructure. We relate variations in strain rate to the compaction length and show that band spacing increases with increasing compaction length. These experiments provide new information on the evolution of melt distribution, the partitioning and localization of strain, and the scaling of experimental results to Earths mantle.

2.1 Introduction

Many locations in the Earth experiencing significant amounts of deformation, such as mid-ocean ridges, subduction zones and mantle plumes, are also places where melt is produced and transported to the Earths surface. Melt segregation is useful in explaining both recent seismic and geochemical observations. Based on seismic observations, a partially molten asthenosphere consisting of thin, horizontal melt-rich layers has been proposed as one mechanism to create the sharp viscosity and mechanical decoupling at the lithosphere-asthenophere boundary (Kawakatsu et al., 2009; Rychert & Shearer, 2009). Geochemical evidence reveals that mid-ocean ridge basalt (MORB) is not in chemical equilibrium with upper mantle peridotite. MORBs are under-saturated in clinopyroxene compared to an equilibrium melt composition for the top of the oceanic mantle even though clinopyroxene is present throughout the bulk of the region of the mantle through which the melt must have traveled (Stolper, 1980; Elthon, 1983). Additionally, the ratio of light-to-heavy rare earth elements is higher in MORB than in dredged samples of abyssal peridotite (Johnson et al., 1990; Johnson & Dick, 1992) or in samples from ophiolites (Kelemen & Dick, 1995). These geochemical observations require that melt must be organized into channels so that it can travel through 40 km of the mantle without equilibrating with its surroundings. Proposed mechanisms to create heterogeneous melt distribution in the upper mantle include a reactive instability (e.g., Daines & Kohlstedt, 1994; Aharonov et al., 1995) and stress-driven segregation of melt (e.g., Holtzman et al., 2003; Katz et al., 2006). In this study, we present new experimental results related to stress-driven melt segregation.

Stevenson (1989) concluded that small perturbations in the spatial distribution of melt fraction in a deforming partially molten rock are amplified due to the decrease in viscosity of the rock with increasing melt fraction. He argued that the liquid pressure is lower in regions of higher melt fraction. Since melt flows to regions of low pressure, melt will continue to accumulate in regions where it is already concentrated. He predicted, and demonstrated in a 1-D numerical model, that this positive feedback produces an instability that leads to segregation of melt into melt-rich bands in a deforming partially molten rock.

High-pressure and high-temperature experiments on partially molten aggregates

have confirmed that an applied stress leads to the emergence of patterns in the distribution of melt (e.g., Kohlstedt & Zimmerman, 1996; Zimmerman et al., 1999; Rosenberg & Handy, 2001; Holtzman et al., 2003; Holtzman & Kohlstedt, 2007). A shear stress causes melt pockets to align and, in some cases, causes melt to segregate into a network of melt-rich bands angled $\sim 20^\circ$ antithetic to the shear plane that surround lenses of melt-depleted rock. Important effects of phase rearrangement on the deforming partially molten rock include the following: 1) Because the viscosity within the melt-rich bands is significantly lower than in the neighboring melt-depleted areas, the bands become zones of localized deformation. Phase segregation could be an underlying process leading to the formation of shear zones, which are a fundamental component of plate tectonics. 2) The melt-rich bands are high-permeability pathways through which melt can flow, possibly facilitating the observed chemical disequilibrium between MORB and peridotite. Magma dynamic theory has been developed to describe the flow of melt through a partially molten rock (e.g., McKenzie, 1984; Scott & Stevenson, 1986; Spiegelman, 1993; Bercovici et al., 2001). The compaction length (δ_c) is the characteristic length scale for problems involving fluid flow along with compressible matrix deformation. It is the length over which a viscously deformable porous solid matrix can maintain low-viscosity fluid flow without compacting and expelling the fluid. Following McKenzie (1984), δ_c is given by

$$\delta_c = \left[\frac{\xi + 4/3\eta}{\mu} k_\phi \right]^{1/2}, \tag{2.1}$$

where ξ is the bulk viscosity, η is the shear viscosity of the partially molten rock, k_ϕ is the permeability of the matrix (which is a function of melt fraction, ϕ), and μ is the viscosity of the melt.

Several theoretical studies have since expanded on Stevenson's (1989) analysis of melt-rich band formation. Hall & Parmentier (2000) demonstrated that the instability is amplified due to an increase in viscosity in melt-depleted regions associated with partitioning of water into the melt. Melt-rich band formation was modeled in simple shear by Spiegelman (2003) and Rabinowicz & Vigneresse (2004). Spiegelman's 2-D linear analysis demonstrated that melt-rich bands oriented 45° to the shear plane grow fastest, bands rotate passively with increasing strain and bands at an angle $> 90^\circ$ to the shear plane decay. No preferred wavelength for growth rate of melt-rich bands, greater

than a compaction length, was found in the linear analysis. A steady-state analysis of viscous energy dissipation presented by Holtzman et al. (2005) concluded that a band angle of $\sim 20^{\circ}$ is a favorable configuration that minimizes stress differences between band and non-band regions and corresponds to a minimum in viscous energy dissipation. Katz et al. (2006) expanded on the linear analysis of Spiegelman (2003) to include the effects of strain-rate weakening with a power-law rheology in addition to weakening due to increased melt fraction. They demonstrated that, with a stress exponent of $n > 4$, the low angle bands observed in experiments could be numerically simulated. This stress exponent is inconsistent with experimental data, but the authors point out that other nonlinear effects involved with band reconnection and realignment might lead to a lower band angle for a given stress exponent. Butler (2009) found that buoyancy forces can be similar to or greater than forces driving stress-driven melt segregation in the mantle, which could lead to a second set of bands at a high angle to the shear plane. Recently, Takei & Holtzman (2009a,b) presented a model for deformation of partially molten rocks that incorporates contiguity of melt as an internal state variable. They demonstrated that low angle bands can be explained by melt-weakening and viscous anisotropy, without considering a power-law viscosity.

With this considerable progress in the theory of melt-rich bands, experimental studies of stress-driven melt segregation remain critical to provide more detailed constraints for modeling efforts. One important goal of experimental studies has been to develop a relationship to estimate the scale at which such features might form in Earth's mantle (Holtzman et al., 2003; Holtzman & Kohlstedt, 2007; Kohlstedt & Holtzman, 2009; Kohlstedt et al., 2010). In the context of magma dynamics theory, bands are low-pressure zones of decompaction, while the melt-depleted lenses between bands are zones of compaction. Holtzman et al. (2003) varied δ_c in a series of experiments by changing the sample materials in order to change the permeability and the contrast between solid and melt viscosities. Similarly, Kohlstedt et al. (2010) varied δ_c in experiments on feldspathic rocks by controlling the melt fraction. Holtzman & Kohlstedt (2007) varied δ_c by carrying out experiments at different stresses or strain rates. If stress and strain rate are related non-linearly, the shear viscosity ($\eta = \tau/\dot{\gamma}$) decreases with increasing stress according to the relation $\eta \propto \tau(1-n)$, where n is the stress exponent. In all of these studies a systematic relationship between δ_c and band spacing was observed.

In the present study, we utilize torsional deformation experiments to investigate the dynamics of melt segregation and organization. This paper focuses on the spacing of melt-rich bands and the evolving structure of the band network with increasing strain. The torsion geometry has several advantages over the direct shear geometry in studies of stress-driven melt segregation. Torsion samples are larger, with a height of 5 mm vs 1 mm for direct shear experiments. The greater thickness yields a greater number of bands in each sample leading to more robust statistics on band spacing. Unlike the direct shear geometry, there is no limit to the amount of shear strain the sample can accommodate without losing contact with the pistons. Because stress, strain, and strain rate vary along a radius from the center to the outside of a cylindrical torsion sample, a wide range of deformation conditions can be observed within a single sample. Also, torsion deformation approximates to simple shear, while direct shear involves components of both simple shear and pure shear. In the experiments presented here, δ_c is varied by deforming a set of samples in torsion at different constant strain rates, similar to the approach used in the direct shear experiments of Holtzman & Kohlstedt (2007).

2.2 Experimental design

2.2.1 Sample preparation and assembly

Samples were prepared by mechanically mixing San Carlos olivine (72 vol.%), chromite from the Samail Ophiolite, Oman (24 vol.%), and powdered MORB glass (4 vol.%). The mixture was cold pressed into a nickel capsule before hot isostatic pressing for at least 2 h at 1200°C and 300 MPa in a gas-medium pressure vessel (Paterson, 1990). A portion of the starting material was then polished to optically verify the homogeneity of the phase distribution throughout the sample. The starting grain diameters were $\sim 6\,\mu m$ for olivine and $\sim 2\,\mu m$ for chromite. During hot-pressing the olivine grain size grew to $\sim 8\,\mu m$. The starting material was cut into cylinders 3-6 mm in height and ~ 9 mm in diameter and inserted into a ~ 1 mm thick Ni sleeve. Dunite spacers were placed above and below the sample to create a non-reactive, impermeable boundary. The sample, spacers, and Al_2O_3 pistons were enclosed in an iron jacket as described in Paterson & Olgaard (2000).

2.2.2 Apparatus

Samples were deformed in a gas-medium deformation apparatus equipped with a torsion actuator (Paterson & Olgaard, 2000). Experiments were performed at a constant rate of angular displacement as measured by a rotational variable displacement transducer (RVDT) outside the pressure vessel. Torque was measured by a torque cell housed inside the pressure vessel. Temperature was monitored near the sample using a Pt-Pt/Rh thermocouple. Furnace calibrations confirm variation of $< 1°C$ along the length of the sample. Methods for determining shear stress and shear strain rate from torque and angular displacement as a function of time are described in Paterson & Olgaard (2000).

2.2.3 Procedure

Experiments were designed to explore the melt distribution in a series of samples deformed at different strain rates to approximately the same finite strain (strain rate series) and in a series of samples deformed at approximately the same strain rate to different finite strains (strain series). Shear strain rates in the strain rate series range from $\dot{\gamma}_R = 1.8 \times 10^{-5}$ to $1.4 \times 10^{-4}\,s^{-1}$ where $\dot{\gamma}_R$ is the strain rate at the outer radius of the sample. As described in the introduction, varying the strain rate is one experimental approach that can be taken to vary δ_c for a non-Newtonian material. Due to the long run time of the low strain rate experiments and due to the importance of observing the band structure early in its evolution, these samples were quenched at relatively low finite shear strains of $1.3 < \gamma_R < 1.8$ where γ_R is the strain at the outer radius of the sample. Samples in the strain series were all deformed at a strain rate close to $\dot{\gamma}_R = 2 \times 10^{-4}\,s^{-1}$ and were quenched at finite strains of $1.6 < \gamma_R < 6.8$. All experiments were preformed at a temperature of 1200°C and a confining pressure of 300 MPa.

After deformation, the samples were cut in half through their central axis perpendicular to the piston-sample interface. Observations were then taken from a polished radial section and from a polished tangential section at the outer radius of the sample, as indicated in Figure 1. Radial and tangential sections were polished using diamond lapping film to 0.5 μm and finally using colloidal silica. Samples were then chemically etched with a weak solution of HF and HCl, which preferentially etches the quenched

melt phase.

2.2.4 Image analysis method and band spacing statistics

To analyze the distribution of the melt phase, we used image processing techniques similar to those described in Holtzman & Kohlstedt (2007). A set of optical reflected-light images were taken to cover each face and stitched together. Lower resolution images (1.5 pixels/μm) were taken of the entire tangential and radial faces, and higher resolution images (6 pixels/μm) were taken of vertical strips on both sample faces, as presented in Figure 1b. By applying a threshold to the high-resolution images to remove pixel values corresponding to olivine and chromite, a binary image was created with only the melt appearing as black. After the binary image was created, the image resolution was reduced to 2 pixels/μm due to computational limits for the following image processing steps. These images were smoothed by centering a 2-D Gaussian filter matrix on each pixel in the image. The filter was convolved with the overlapping region of the image and then divided by the number of pixels in the smoothing matrix. Several sizes of filters ranging in radius from 10 to 50 μm were tested to assure that the results of band spacing analyses were not affected by filter size. A 20 μm radius filter, which is several times the average grain diameter, but significantly less than the band spacing, was found to be the optimum filter. This filter size yields smoothly varying grayscale images without blurring important details in the melt distribution.

The angle between a melt-rich band and the macroscopic shear plane (α) and the band thickness (δ_{th}) were measured from the lower resolution images of the entire tangential face. Two to three lines were drawn on the images perpendicular to the shear plane. At each intersection between the line and a melt-rich band, the angle of the band to the shear plane was measured as was the thickness of the band perpendicular to its length, as illustrated in Figure 1b.

Grain size within the bands was measured by a linear intercept method. High resolution optical images were taken of bands of etched samples. The grains were traced by hand, and straight lines were drawn across the tracing. The distance across each grain where it intersected the line was measured. A correction factor of 1.5 was applied to these measurements to convert the measurements to an estimate of grain diameter (Gifkins, 1970).

The 2-D autocorrelation function (ACF) was calculated from smoothed images taken on the tangential faces of samples, as summarized in Figure 2. The input matrix is a smoothed image mapped for melt fraction, pictured in Figure 2a. The ACF calculates the degree of correlation between an image and a copy of that image centered at each pixel in the image. Therefore, the resulting ACF matrix in Figure 2b is four times larger than the input matrix. The linear decay in the correlation coefficient moving away from the center of the ACF matrix in all directions, as observed in Figure 2b, is a function of decreased overlap of the input matrix with an increasingly shifted version of itself. A profile through the ACF matrix perpendicular to the shear plane (Figure 2c) yields the preferred band spacing. We removed the linear trend from the profile and plotted just the first 500 μm of lag from the center of the ACF in Figure 2d. The repeating peaks at evenly spaced intervals are interpreted to be the phase shift at which melt-rich bands preferentially line up with one another. The results are then compared with visual inspection of the original images. In addition to providing a method for quantifying the preferred spacing between melt-rich bands, the ACF method provides a simple, robust means for determining the average band angle to the shear plane. The preferred trace of the bands is revealed in asymmetries in the array of correlation coefficients.

2.3 Results

2.3.1 Strain rate series

In this section we describe the band morphology in the series of samples deformed at different constant strain rates of $1.8 \times 10^{-5} < \dot{\gamma}_R < 1.4 \times 10^{-4}\,s^{-1}$ all to a finite shear strain of $1.3 < \gamma_R < 1.8$. Rheological data for the sample deformed at the lowest strain rates (PT0323) are plotted in Figure 3. One rate step was performed in the high strain rate sample. The purpose of this set of experiments was to compare observations of the microstructure and melt distribution early in the evolution of the melt-rich band network in samples deformed across a range of strain rates.

Microstructural observations

The reflected-light images of the etched tangential sections in Figure 4 reveal characteristics of the sample shape and melt distribution. In this set of experiments, the samples

remained close to their original, post hot-press shape as a right circular cylinder. The tapered appearance of the tangential sections of the samples in Figure 4a and b is a result of the sample being slightly tilted relative to the axis of the cylinder during polishing through the nickel jacket. The sample deformed at $\dot{\gamma}_R = 3.3 \times 10^{-5}\,s^{-1}$ (PT0297) is slightly necked in the center. At a finer scale, the sample-jacket interface is somewhat irregular in all of these samples with places where the nickel jacket follows offsets in the sample due to shear on melt-rich bands. This irregularity of the sample-jacket interface is often, but not always, associated with a melt-rich band. There are bands without an associated indent and indents without an associated band.

The sample in Figure 4b deformed at $\dot{\gamma}_R = 5.5 \times 10^{-5}\,s^{-1}$ (PT0308) is unique in this series because it contains a strain marker. After hot-pressing and prior to deformation, the sample was cut in half axially to insert a thin piece of nickel foil ($\sim 10\,\mu m$) along the central axis to act as a strain marker. The one macroscopically visible offset in the strain marker visible in Figure 4b occurred along a band at an angle of 24° to the macroscopic shear plane. This sample also has the greatest sample height in the series (see Table 1). Bands are clearly visible, but they are somewhat thinner or more wispy than the other samples in this series. Fewer of the bands are continuous across the entire view on this polished section than in the samples in Figure 4a,c&d. The one band along which the strain marker is offset is clearly continuous across the entire tangential face.

The value of the angle between melt-rich bands and the macroscopic shear plane within each sample and among the set of samples in the images in Figure 4 is plotted in histograms of the band angles measured from these tangential faces in Figure 5a-d. The four samples in the strain rate series have relatively narrow distributions of band angles with means between 15° and 19°. The distribution corresponds well to the visual observation that the intersections of bands with the polished surface form straight, laterally extensive lines. Deeper polishing on tangential sections and observations from the radial sections confirm that bands in these relatively low strain samples are flat planes that form a cork-screw-like structure within the sample. The angles measured from the tangential sections agree well with the average band angle determined from the 2-D ACF.

Measurements of band thickness from each location where a measurement of band angle was made allow us to look for a correlation between these two quantities, as

presented in Figure 6a-d. The relatively narrow distribution of band angles in the strain rate series apparent in Figure 5 is also clear in these plots. Significant variations in band thickness are not clearly apparent across the narrow range of band angles determined within each of these samples, but the thickness of bands in the sample deformed at $\dot{\gamma}_R = 3.3 \times 10^{-5}\,s^{-1}$ (PT0297) does increase with increasing band angle.

The thickness of the bands varies among the samples both as a function of grain size and strain rate. In Figure 7a, band thickness is plotted vs the average grain diameter in the band. The band thickness increases with increasing grain diameter. In Figure 7b band thickness is plotted as a function of strain rate. The samples follow a clear trend of increasing band thickness with decreasing strain rate. Grain size within the bands also varies as a function of strain rate, as plotted in Figure 7c. The average grain diameter increases with decreasing strain rates and the grain size, at least near the outer radius of the sample, is less than the starting grain size. These results suggest that dynamic recrystallization lead to decreasing grain size with increasing stress. High resolution optical images in Figure 8 illustrate the increase in both band thickness and grain size with decreasing strain rate (i.e., decreasing stress). Bands are consistently 3-5 grains wide.

Band spacing analysis

Visual inspection of polished sections of these samples suggests that melt-rich bands are more widely spaced and less penetrative in samples deformed at lower strain rates. The difference is particularly clear in comparing the sample deformed at the lowest strain rate in Figure 4d to the others in the series in Figure 4a,b,c. The sample deformed at $\dot{\gamma}_R = 1.8 \times 10^{-5}\,s^{-1}$ (PT0323) in Figure 4d has well-defined, high melt fraction bands that have a spacing of $\sim 500\,\mu m$ and thinner, lower melt fraction bands with closer spacing. The other samples in the series have more closely spaced bands with less variation in amplitude (melt fraction).

Results from the ACF analyses correspond well with visual inspection of the optical images and quantify a trend of increasing band spacing with decreasing strain rate. The first peak in the ACFs plotted in Figure 9a-d is at the lag at which a shifted version of the image lines up well with itself, which should correspond to the dominant wavelength of the bands. The lag at which the first peak appears increases in samples

deformed at decreasing strain rates. The amplitude difference between the peaks and troughs in the ACF also increases with decreasing strain rate. This pattern correlates with the visual observation that bands are more pronounced in the samples deformed at lower strain rates. Interestingly, the first peak in the ACF does not necessarily have the greatest value of correlation coefficient. In the plots of correlation coefficient vs lag for three samples in Figure 9a,c&d, the peak at approximately double the lag of the first peak is as great as or greater than the first peak. This observation is consistent with the observations described above for the sample deformed at $\dot{\gamma}_R = 1.8 \times 10^{-5}\,s^{-1}$ (PT0323) and suggests that melt-rich bands may be growing simultaneously at multiple wavelengths, or that there are multiple generations of bands growing out of phase with one another. The relatively poor resolution of peaks in the sample deformed at $\dot{\gamma}_R = 5.5 \times 10^{-5}\,s^{-1}$ (PT0308) corresponds well with the observation that melt is less segregated in this sample than in the others.

2.3.2 Strain series

In this section, we describe the microstructure of the band network in a series of samples deformed to increasing shear strain. The samples in this series were deformed over a narrow range of constant shear strain rates from $\dot{\gamma}_R = 1.2 \times 10^{-4}$ to $2.2 \times 10^{-4}\,s^{-1}$. The lowest strain sample in this series is the high strain rate sample from the strain rate series, which was quenched at $\gamma_R = 1.6$. The other three samples in this series were deformed to shear strains of $\gamma_R = 2.2$, 4.2, and 6.8. A typical stress-strain curve, for the sample deformed to $\gamma_R = 2.2$ (PT0313), is plotted in Figure 3.

Microstructural observations

Images of polished and etched tangential sections in Figure 10 allow us to examine macroscopic changes in shape and melt distribution with increasing shear strain. The shape of the samples is increasingly irregular with increasing shear strain. The asymmetric outline of the tangential sections in the high-strain samples cannot be explained by tilting of the sample during polishing. Significant strain partitioning during deformation must have lead to macroscopic shape change of the samples. The sample deformed to $\gamma_R = 2.2$ (PT0313) has significant irregularities along the sample-jacket interface at its outer radius. The two largest irregularities coincide with especially high

melt fraction bands, which appear very dark in the images of the etched sample. Sections of the sample-jacket interface in the sample deformed to $\gamma_R = 6.8$ (PT0329) are highly serrated, as highlighted in Figure 10d. In significant regions of all of the samples deformed to shear strains of $\gamma_R > 2$, the intersection of the bands with the polished surface is curved, though bands generally remain parallel. That is, many adjacent bands are kinked with a similar curvature. This behavior is particularly clear in the central portion of Figure 10b.

The histograms of band angles measured from the tangential sections in Figure 5e-h reveal the increased variation in band angles that results from the curved morphology of the band network. The range of band angles observed in high-strain samples is significantly larger than in the series of samples quenched at $\gamma_R > 2$. The mean angle between the bands and the shear plane also decreases with increasing strain.

In Figure 6e-h, plots of band thickness vs band angle for each of the samples reveal the wider range of band angles for the strain series compared to the strain rate series; this tendency was also apparent in Figure 5e-h. In the sample deformed to $\gamma_R = 4.2$ (PT0276), a weak trend of increasing band thickness with increasing band angle is apparent. The other samples do not reveal a clear relationship between these two quantities.

The grain size within the melt-rich bands does not vary systematically with increasing strain. The measured grain diameters are similar in all of the samples in the strain series with $5 < d < 8\,\mu m$. When plotted as a function of strain rate in Figure 7c, the measured grain size corresponds well with the results from the strain rate series.

The inclusion of a strain marker in the sample deformed to $\gamma_R = 6.8$ (PT0329), combined with its particularly high shear strain, make it an interesting sample to observe how strain is partitioned in samples with melt-rich bands. As in sample PT0308 described in the strain rate series, after hot-pressing and before deformation the sample was cut in half to insert a thin piece of nickel foil ($\sim 10\,\mu m$) between the two halves. In Figure 10d, the strain marker appears twice because the sample was twisted nearly two complete revolutions. Both deflections and offsets of the strain marker occurred. Though the average band angle observed in this sample is $\sim 9°$, the bands accommodating offsets in the strain marker are consistently between 15° and 18°.

Band spacing analysis

The curved morphology of the bands and the increased strain partitioning in the higher strain samples lead to more variability in all of the measurable properties of the bands, including the band spacing. Spatial variation in band spacing in the high-strain samples is greater than in the low-strain samples in the strain rate series. For example, the region near the center of the sample in Figure 10b, deformed to $\gamma_R = 2.2$ (PT0313), has more closely spaced bands than the region with the high melt fraction bands that are coincident with a highly irregular sample-jacket interface. In the following analysis, we used images that encompassed a large section of the sample incorporating the variability in band morphology.

The ACFs plotted in Figure 11a-d for the four samples deformed at the same strain rate reveal that band spacing is independent of strain. For samples plotted in Figure 11c&b, deformed to $\gamma_R = 2.2$ and 4.2, the first peak in their correlation coefficients indicate a preferred band spacing of $\sim 70\,\mu m$. This result is consistent with the first peak in the ACF for the sample analyzed in the strain rate series deformed at a similar strain rate but quenched at $\gamma_R = 1.6$ in Figure 11d. The ACF for the highest strain sample deformed to $\gamma_R = 6.8$ (PT0329) in Figure 11a has a preferred spacing of $\sim 145\,\mu m$, approximately double that for the other samples in this series.

The preferred band spacing for all of the samples in both the strain rate series and the strain series are plotted as a function of strain rate in Figure 12. With the exception of the sample deformed to $\gamma_R = 6.8$ (PT0329), the samples define a clear trend in which band spacing increases by approximately a factor of four as strain rate decreases by a factor of ten. The nickel foil placed in this high-strain ($\gamma_R = 6.8$) sample as a strain marker may have affected the development and evolution of the melt-rich band network, or this very high strain sample could contain multiple generations of melt bands.

2.3.3 Observations from radial sections

In the previous sections we summarized observations taken from the tangential sections of samples deformed at different strain rates and to different finite strains. In the torsion geometry both of these parameters vary within the volume of the sample, though not independently. From the radial section of a torsion sample, a cut through the center

of the sample, we can observe the microstructure across a gradient in both strain and strain rate within one sample.

The distance that the bands extend from the outer radius toward the center varies among the samples as a function of strain. Samples from two deformation experiments (PT0268 and PT0276) in Figure 13 deformed at similar constant rates to different finite strains $\gamma_R = 1.6$ and 4.2) illustrate the relationship between band extent and shear strain. The vertical dashed lines are drawn at the radius corresponding to $\gamma = 1$ in both images. This line approximates well the extent of the most prominent bands from the outer radius toward the center of the sample. The shear stress as a function of radius (r) is also plotted on the images according to the relation from Paterson & Olgaard (2000)

$$\tau_r = M \frac{4(3 + 1/n)}{\pi(2R)^3} \left(\frac{r}{R}\right)^{1/n}, \tag{2.2}$$

where M is the measured torque, R is the maximum sample radius and n is the stress exponent. A stress exponent of $n = 1.6$ was determined from rate steps performed in several experiments. Since n is linearly related to M, the log-log plot of $\dot{\gamma}_R$ vs M in Figure 14 can be used to determine the stress exponent. This determination is a useful estimate for n, and it is consistent with the olivine flow law of Hirth & Kohlstedt (2003), which predicts an intermediate stress exponent for the strain rates at which these experiments were performed. The stress exponent actually varies as a function of strain rate (radius), but the measured torque is most representative of the outer portion of the sample because that is where most of the volume of the sample is. (For a complete discussion see Paterson & Olgaard (2000).) For comparison, we plot shear stress profiles for the measured value of n and for $n = 3.5$, which is the expected stress exponent for dislocation creep in olivine and thus defines a reasonable upper limit for shear stress. For a stress exponent of $n = 1.6$ the shear stress at the radius to which the bands extend into the sample varies from 15 to 100 MPa among the various samples. The use of a larger stress exponent ($n = 3.5$) makes the stress profiles flatter towards the outer radius and therefore reduces the range of stresses among the different samples. With either value for the stress exponent, the observation remains the same that the radius to which bands extend into the radial section occurs across a broad range of stresses but at $\gamma \approx 1$. This is consistent with observations from Holtzman et al. (2003) that samples quenched before reaching a shear strain of $\gamma \approx 1$ do not display visible

melt segregation at length scales greater than the grain size.

More detailed analysis of the band front reveals a more complex relationship among band propagation, stress, and strain. The band front is not a sharp boundary between segregated and unsegregated regions. As visible in Figure 13a, some faint bands penetrate farther into the sample than the most prominent bands that extent to the dashed line corresponding to $\gamma = 1$. We define this region as the band front. The band front is wider in lower strain samples and narrower in high strain samples. The band front, normalized to the sample radius, is plotted vs γ_R in Figure 15 with a line on the plot that indicates the radius at which $\gamma = 1$. The strain series, solid lines, reveal the increasing penetration with increasing strain and the narrowing of the band front at higher strains. Results from the lower stress samples of the strain rate series, dashed lines, indicate that bands do not penetrate as far into samples deformed at lower stress. The approximation that the band front corresponds with $\gamma = 1$ holds, but these results suggest that band propagation may decelerate at higher strain and that the band extent varies somewhat as a function of stress. The variation of band front with stress is consistent with observations from the rheological data, presented in Figure 3, that demonstrate that the peak stress occurs at lower strain in samples deformed at higher strain rates.

To determine if band spacing changes from the outside toward the center of a sample, micrographs were taken at different distances from the outer radius on a radial section, as summarized in Figure 16. One image is from near the interface between the jacket and the sample, a second image is from half the distance to the radial extent of the bands, and a third image is from near the termination of the bands. The 2-D ACF was calculated for each of these images. The ACFs indicate some increase in band spacing from image 1 to image 2 in Figure 16, but band spacing does not systematically increase moving toward the center of the sample. These results are consistent with visual inspection where we observe that the number of bifurcations opening towards the center of the sample is similar to the number of bifurcations opening towards the outside of the sample.

2.4 Discussion

We have presented observations of the development and evolution of melt-rich bands that form in response to an applied shear stress in samples deformed torsion. One purpose of this study was to investigate the dependence of the melt-band network on shear strain rate (or shear stress). Since these experiments were done at constant twist rates the observations are reported as a function of strain rate, but the variation in microstructural properties is really due to the difference in applied force or energy input to maintain these constant rates. A second purpose of this study was to investigate the evolution of the melt-band network with increasing strain. Visual observations and analyses using the 2-D ACF demonstrate that band spacing decreases as strain rate increases. With increasing strain, the variability in band angle increases while the average angle between bands and the macroscopic shear plane decreases. Questions that arise from this set of experiments include the following: (1) What mechanisms permit the melt to continually reorganize to maintain the low angle of melt-rich bands to the shear plane? (2) How is strain partitioned between melt-rich and melt-depleted regions within the samples, and how does strain partitioning evolve with increasing strain? (3) Do melt-rich bands occur in the mantle, and how can the dependence of band spacing on strain rate be scaled to predict the spacing of melt-rich bands in the Earth?

2.4.1 Evolution at high strains

Evolving Band Network

In the samples in the strain rate series, all of which were quenched at relatively low strains ($\gamma_R = 1.3 - 1.8$), the intersections of the bands with the tangential face form straight, parallel lines. Few junctions where melt-rich bands intersect one another exist. The melt fraction is still high enough in the lenses between the bands to support a fully interconnected network of melt pathways along olivine triple junctions, but the permeability within these melt-depleted lenses is significantly smaller than the permeability in the melt-rich bands. The one sample in the strain rate series with a strain marker, which was deformed at $\dot{\gamma}_{\mathrm{R}} = 5.5 \times 10^{-5}\,\mathrm{s}^{-1}$ (PT0308), contains evidence for a minor amount of strain partitioning into melt-rich bands by a strain of ($\gamma_R = 1.8$. We interpret this observation to suggest that, at relatively low strains ($\gamma_R < 2$), strain

is relatively homogeneously distributed through the sample with a small amount partitioning of strain into the melt-rich bands, but without any single band developing into a shear zone with large offset.

In samples in the strain series deformed to $\gamma_R > 2$, bands remain close to parallel but with much more variation in band angle along any individual band than in the sample deformed to $\gamma_R = 1.6$. The planes that define the melt-rich bands are warped in some regions of the samples as highlighted by the box in Figure 10d. We refer to the region in which several parallel bands deviate from their usual orientation as a kink. These features are analogous to kink bands that have been described in materials with anisotropic layering and σ_1 at a low angle to this layering (e.g., Stewart & Alvarez, 1991; Kirschner & Teixell, 1996; Debacker et al., 2008), but we will not refer to them as (kink) bands to avoid confusion with melt-rich bands. In general, melt-bands with a higher melt fraction are more straight and they often bound regions of bands with a lower melt fraction that are kinked. If the bands in the kink were originally flat planes, as observed in the low-γ samples, the sense of rotation required to create these kinked zones of bands is consistent with deformation involving localization within the higher melt fraction bands that remain flatter. A tracing of melt-rich bands in Figure 17 from a region of the sample that was deformed to $\gamma_R = 2.2$ (PT0313) reveals the anastamosing structure of the network of melt-rich bands with thin, low-angle bands that appear to be propagating through the lenses linking higher angle bands together (see Figure 10b for the location of this tracing). We interpret this region to be one in which melt from bands that were kinked to a high angle was reorganizing and flowing into lower angle bands at the time of quenching. Another example of a high-angle kink, perhaps earlier in its evolution, is visible in Figure 18a, which illustrates the aligned rotation of several bands in the sample deformed to $\gamma_R = 6.8$ (PT0329). The kink in the melt-rich bands is at an angle of $\sim 70^\circ$ to the macroscopic shear plane. In this example, it appears to be in a forward-rotated orientation relative to the shear direction, but in other cases it is observed in a back-rotated orientation.

Information from strain markers strain partitioning

From the strain markers that were placed in two of the samples in this study, we can learn about the shear offset that occurs on some, but not all, of the melt-rich bands. As

discussed above, the sample deformed to $\gamma_R = 1.8$ (PT0308) does not show significant partitioning of deformation in to bands as evidenced by few distinct offsets in the strain marker. In the highest strain sample deformed to $\gamma_R = 6.8$ (PT0329), many offsets occurred in the nickel strain marker. In both figures 4b and 10d, the shear angle of the strain marker in the homogeneously deforming regions is similar between the two samples. Therefore, in the high strain sample much more strain must have been accommodated as discrete offsets along melt bands. In other words, strain partitioning increases with increasing strain. This observation is consistent with rheological data indicating that samples continuously weaken at strains higher than $\gamma = 1$ rather than reaching a steady state strength.

The observation that average band angle decreases with increasing strain could be related to the increased strain partitioning observed in samples deformed to higher strains. The analysis of Holtzman et al. (2005) includes a partitioning factor that quantifies the ratio of energy dissipated within the bands to the energy dissipated in the lenses. The microstructural and rheological results from torsion experiments to high shear strain suggest that this partitioning factor evolves with increasing strain. Some of the offsets of the strain marker coincide with the presence of melt-rich bands, suggesting that these offsets occurred relatively close to the termination of the experiment. Offsets that do not coincide with a melt-rich band must have formed when melt-rich bands were in these locations; these bands have subsequently rotated relative to the matrix or the melt from them drained during a reorganization of the band network. In places where a band corresponds with an offset in the strain marker, the band tends to have a higher melt fraction than other bands that have not accommodated any visible offset indicating a feedback linking increased strain localization and the driving force for melt segregation.

These observations lead to several new questions. (1) What determines if a melt-rich band becomes a shear zone? The development of shear zones from bands could involve both influences from sample geometry and variations in melt fraction among the bands. (2) Is there a preferred spacing between bands that develop into shear zones? The spacing between bands that develop into shear zones in the sample deformed to $\gamma_R = 6.8$ (PT0329) is several times greater than the observed spacing between the full population of melt-rich bands. It is unclear from this sample if there is a preferred length

scale between shear zones. The sample deformed to the highest strain has anomalously high preferred spacing between bands for the strain rate at which it was deformed. It is possible that some length scale for localized deformation or geometrical constraint is influencing spacing between bands in this high-strain sample.

2.4.2 Dynamics of melt organization

Holtzman et al. (2005) presented a pumping mechanism through which melt is continually redistributed, also discussed in Katz et al. (2006) and Holtzman & Kohlstedt (2007). The pumping mechanism relies upon an interconnected network of melt-rich bands to redistribute melt in order to maintain the energetically favorably orientation. The model suggests that at a critical angle of $\sim 30^\circ$, the melt is forced out of higher angle bands into lower angle bands that then grow and rotate until they reach the critical angle. Alternatively, bands could maintain the low angle to the shear plane by rotating relative to the matrix, propagating as waves of high melt fraction.

In the present study, we observe many aspects of band morphology consistent with the pumping mechanism. The absence of bands, except in some kinks, at an angle greater than 35° in any of our samples is consistent with the suggestion of a critical angle above which bands are unstable. The greater variability of band angle with increasing strain is consistent with low angle bands forming in response to the draining of high-angle bands.

The high-angle kinks described above, which are a pervasive feature in torsion samples deformed to shear strains of $\gamma_R > 2$, provide an additional aspect to the pumping mechanism for the redistribution of melt and reorientation of melt-rich bands. Melt-rich bands in regions adjacent to a melt-rich band accommodating localized deformation are kinked into a high angle to the macroscopic shear plane. These regions of high-angle bands are unstable and melt flows from these regions as depicted in Figure 17. The bands then grow parallel to the overall preferred angle of $\sim 20^\circ$ to the macroscopic shear plane in the adjacent non-kinked region and may link with bands with which they were not previously connected in the region across the kink. The ubiquitous presence of kinks in polished tangential sections of samples deformed to $\gamma_R > 2$ suggests that kinks at transient features that propagate through the torsion samples as waves of band

reorganization. This could reflect another instability at a greater length scale than the bands.

2.4.3 Scaling by δ_c

Previous studies on stress-driven melt segregation have utilized δ_c as a scaling parameter to predict the scale at which melt-rich bands might form within Earth based on observations from laboratory experiments (Holtzman et al., 2003; Holtzman & Kohlstedt, 2007; Kohlstedt & Holtzman, 2009). To compare our results to those of Holtzman & Kohlstedt (2007), we have used their method of calculating δ_c for our samples. Following the approximation used by Daines & Kohlstedt (1993), Holtzman et al. (2003), and Holtzman & Kohlstedt (2007), the bulk viscosity (λ) is dropped from the expression for δ_c:

$$\delta_c = \left(\frac{4/3\eta}{\mu} k_\phi \right)^{1/2} \tag{2.3}$$

Developments in theory (Katz et al., 2006; Takei & Holtzman, 2009a) point to the importance of bulk viscosity in the physics of the deformation of partially molten rocks, so it should not be thought of as insignificant. However, because the exact compaction length is difficult to determine in these samples (largely due to uncertainty in the permeability), the priority in this study is to represent the variation in compaction length among these samples and to provide a meaningful comparison with existing experimental data. Permeability in the melt-depleted lenses is estimated using the following relationship:

$$k_\phi = \frac{\phi^m d^2}{b} \tag{2.4}$$

where d is the grain diameter, ϕ is the melt fraction and b and m are geometric factors. To calculate the permeability in melt-depleted lenses, we use $m = 2$, which is appropriate for an aggregate in which melt is interconnected along three-grain triple junctions (von Bargen & Waff, 1986). Following Holtzman et al. (2003), a value of $b = 10^4$ is used.

In this set of experiments, because shear stress and shear strain rate are related non-linearly, the shear viscosity is a function of strain rate. The shear viscosity and thus δ_c increase from the outer radius toward the center of each sample. This change in viscosity occurs because the strain rate varies linearly with radius while the stress varies non-linearly with radius. Initially, δ_c varies only as a function of radius within

each sample, but as soon as melt begins to segregate, δ_c becomes spatially variable for a given radius, as δ_c increases in the melt depleted lenses and decreases in the melt-rich bands. We calculate the value of δ_c in the lenses between the bands at the outer radius (corresponding to the tangential sections) through the following method. The stress in the non-band regions is calculated from the imposed strain rate using the Hirth & Kohlstedt (2003) combined flow law for dry olivine with a melt fraction of 0.01. The strain rates in this study correspond to the transition in the flow law between diffusion ($n = 1$) and dislocation ($n = 3.5$) creep, which is consistent with the intermediate stress exponent of $n = 1.6$ determined from rate steps in torsion experiments. The band spacing is plotted as a function of the shear stress calculated for the lenses in Figure 19. The sample viscosity (η) can then be calculated for the lenses in each experiment. The permeability for the lenses is calculated from Eq. 4, and δ_c is calculated from Eq. 3 for a melt viscosity of $\mu = 10$ Pa s.

The band spacing based on the first peak in the 2-D ACF (δ^1_{sp} is used to denote spacing based upon the first peak) is plotted as a function of δ_c in Figure 20a. The samples follow a clear trend of increasing spacing between bands with increasing δ_c. A least squares fit to the data through the origin, excluding one outlier (PT0329, which contained a Ni strain marker), gives a slope of 0.2. This slope is similar to the result presented in Holtzman et al. (2003), but in that study δ_c was varied by changing the melt fraction or composition, and δ_c was calculated for the initial homogeneous melt distribution rather than for the melt depleted lenses. The same data are plotted again in Figure 20b with the results of Holtzman & Kohlstedt (2007). The method for calculating δ_c in Holtzman & Kohlstedt (2007) was similar to the approach used here except that they calculated strain rate based on the measured shear stress. In the present study we calculate the shear stress in the melt-depleted lenses based on the controlled shear strain rate. The same Hirth & Kohlstedt (2003) flow law was used in both studies. The slope of a fit to the data in the Holtzman & Kohlstedt (2007) data, excluding one outlier at $\delta_c \approx 1000\,\mu$m, is 0.5, or about twice the slope calculated from the data set in this study.

The first peak in the ACF may not, however, be representative of the wavelength of maximum growth rate that would dominate in an open system. Harmonic peaks are expected in the ACF, but the strength of the correlation should decay with increasing

lag. In the results, we noted that the second peak in the ACF has a consistently higher correlation coefficient than the first peak. In Figure 20c the peak with the greatest correlation coefficient in the ACF (δ_{sp}^{max}), which is approximately double that of the first peak in each of the samples in the strain rate series, is plotted as a function of δ_c. If this peak is interpreted as the preferred band spacing rather than the first peak in the ACF, then both studies yield the relationship $\delta_{sp}^{max} \approx 0.5 \times \delta_c$ where δ_{sp}^{max} is the preferred band spacing based on the maximum peak. This analysis is probably the most appropriate comparison with the spacing between the largest bands as identified in Holtzman & Kohlstedt (2007). We interpret these results to indicate a preferred length for formation and growth of bands of $0.5\delta_c$, but that melt reorganization also leads to multiple overlapping generations of growing and decaying melt bands.

2.4.4 Band thickness

The range of band thicknesses in this set of torsion experiments was small, making it difficult to determine what controls band thickness. From the relationships among band thickness, grain size, and strain rate presented in Figure 7, we are unable to determine which relationships are causal. Band thickness increases with decreasing strain rate, which is equivalent to band thickness increasing with increasing δ_c. Because all samples exhibit a similar extent of segregation with lenses depleted in melt to $\phi \approx 0.01$ and bands enriched in melt to $\phi \approx 0.2$, this pattern is consistent with the result that bands spacing increases with increasing δ_c. However, because grain size also increases with decreasing strain rate (or stress), we cannot rule out a direct relationship between band thickness and grain size as observed in shear bands in materials deforming by granular flow (Gourlay & Dahle, 2007).

The thickness of melt-rich bands in our torsion experiments are similar to the thickness of bands in the constant rate direct shear experiments of Holtzman & Kohlstedt (2007), with thicknesses of $\sim 20\,\mu m$ across the range of experimental conditions. However, the constant load direct shear samples from of Holtzman & Kohlstedt (2007) exhibit greater variation in band thickness, with an average band thickness of $\sim 40\,\mu m$ in the low stress sample. This difference suggests that boundary conditions (sample size, deformation geometry, constant stress vs constant rate) play an important role in some aspects of band formation and evolution. It is most likely that this difference

in band thickness between torsion samples and direct shear samples is related to the sample height. In direct shear samples many bands terminate against pistons at both ends allowing them freedom to grow only in width, while in torsion bands can always grow in length at the band front propagating into the sample.

2.4.5 Band spacing on the radial section

While the band spacing from different experiments in the strain rate series varies systematically with δ_c, the analysis of band spacing as a function of radius within a single sample does not yield a clear relationship between spacing and δ_c, as summarized in Figure 16. Bands initially form at the outer radius of the cylindrical torsion sample and propagate inward, with the band front near $\gamma = 1$. Even though δ_c increases from a minimum value at the outer radius to a maximum value at the center of the sample, the preferred band spacing does not systematically increase. The bands are continuous high-permeability structures across a range of strain rates (or a range of δ_c) while the permeability within the melt-depleted lenses connecting bands at the same strain and strain rate conditions is significantly reduced after segregation has occurred. Our observations suggest that because propagation of the melt-rich bands is more efficient parallel to existing highly permeable pathways than perpendicular to them, the initial spacing that is set where the bands first develop is important in controlling band spacing throughout the entire sample.

2.4.6 Scaling to conditions in Earths mantle

Applying the scaling relationship based on laboratory experiments to natural conditions in Earths mantle requires extrapolating δ_c to the larger grain size and lower stress levels appropriate for the upper mantle. For grain sizes of 1-10 mm, Holtzman et al. (2003) calculated compaction lengths on the order of $\delta_c = 300 - 3000$ m for a differential stress of 1 MPa and $\delta_c = 60 - 600$ m for a differential stress of 10 MPa. The results presented in this study, consistent with the results from Holtzman & Kohlstedt (2007), predict a maximum band spacing of $10 - 1500$ m in the upper mantle. The results from torsion experiments, however, suggest that in a well developed band network bands could be spaced closer together than this preferred length scale for band development.

The reorganization necessary for bands to maintain the low angle to the shear plane could lead to multiple, overlapping generations of bands.

Other effects related to grain size and stress are important to consider when extrapolating experimental results to the Earth. Is there some critical stress below which forces due to surface tension (which re-homogenize the melt distribution) are greater than the driving forces for segregation? The torsion experiments presented here are consistent with the approximation that bands form at $\gamma \approx 1$ across a range of stresses, but rheological data and analysis of the band front suggest that segregation occurs faster at higher stresses. Holtzman & Kohlstedt (2007) presented an analysis that demonstrated that surface tension becomes negligible at the larger grain sizes in the mantle such that melt will still segregate at very low stresses. In Figure 13b bands are observed to propagate almost to the center of a torsion sample where the stress is very low ($\tau \leq 10$ MPa). These bands may not have been present there if they were not propagating inward from higher stress regions, but their presence shows that regions of high melt fraction are relatively stable against surface tension forces at low stresses even at the small grain size in these experiments.

The effects of buoyancy are negligible at the scale of experiments, but could play a significant role in the mantle. Butler (2009) found that buoyancy forces could lead to a second set of bands at high angle to the stress-driven bands. These results complicate the findings of Katz et al. (2006) who demonstrated the ability for melt-rich bands to focus melt at mid-ocean ridges. The effects of buoyancy should also be carefully considered in exploring the hypothesis of thin, melt-rich layers in the asthenosphere (Kawakatsu et al., 2009).

2.5 Conclusions

We have demonstrated that melt-rich bands form in response to an applied shear stress in samples deformed to high strains in torsional deformation. Segregation initiates at the outside of the sample and propagates inward with increasing strain. Melt segregation leads to strain partitioning within the partially molten rock with melt-rich shear zones accommodating a large portion of the overall deformation in samples deformed to high strain. Melt is continuously redistributed within the sample to maintain a low angle

to the macroscopic shear plane that is independent of strain rate (stress) and decreases slightly with increasing strain. Transient, high-angle kinks propagating through the sample may aid in the process of redistributing melt. Consistent with prior studies, we have demonstrated that band spacing varies as a function of compaction length leading to predicted maximum spacing between bands in the mantle of 10-1500 m. Stress-driven melt segregation could be of great importance in focusing melt at mid-ocean ridges and in creating the sharp viscosity contrast that defines the lithosphere-asthenosphere boundary.

Table 2.1: Experimental Parameters

Sample	$\dot{\gamma}(s^{-1})$	γ	τ_f (MPa)	d (mm)	h (mm)	Notes
Strain Rate Series						
PT0323	1.8×10^{-5}	1.3	50	9.18	3.90	
PT0297	3.3×10^{-5}	1.5	35	9.20	5.60	
PT0308	5.5×10^{-5}	1.8	100	9.20	5.75	strain marker
PT0268	1.4×10^{-4}	1.6	105	8.41	3.65	also in strain series
Strain Series						
PT0313	1.2×10^{-4}	2.2	80	8.73	4.23	
PT0276	2.0×10^{-4}	4.2	90	8.60	3.89	
PT0329	2.2×10^{-4}	6.8	80	9.01	5.30	strain marker

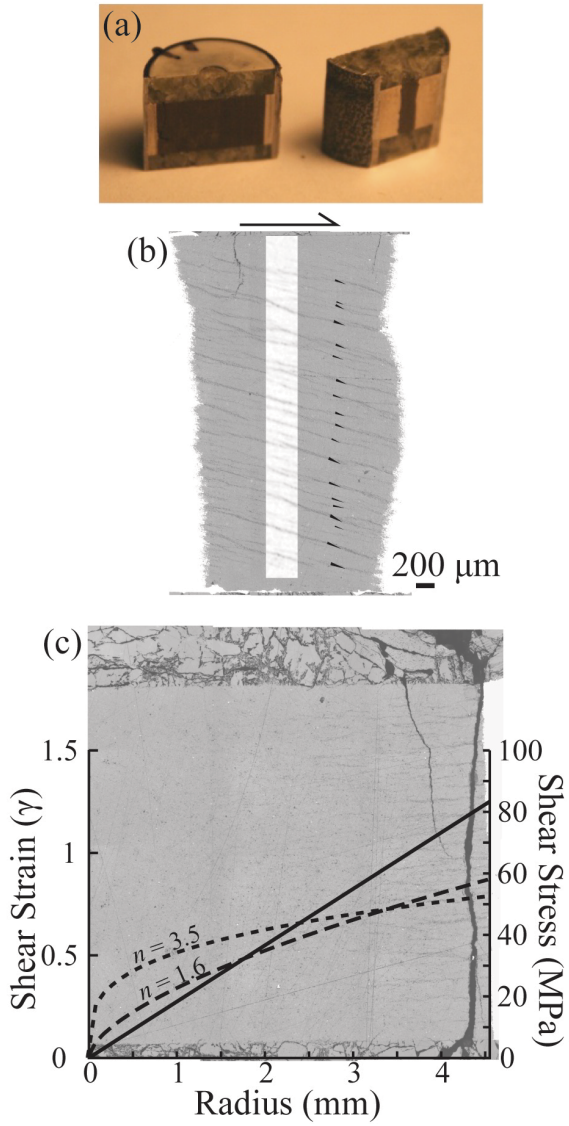

Figure 2.1: (a) Photograph of the post-deformation sample after polishing. The radial face is on the left and the tangential face is on the right. (b) Reflected light image of the tangential face of the sample deformed at $\dot{\gamma} = 1.8 \times 10^{-5}\,\mathrm{s}^{-1}$ (PT0323) with the smoothed binary image superimposed. Black triangles to the right of the smoothed image are locations where band angle and thickness were measured. (c) One half of the radial section of the same sample. The strain as a function of radius is plotted with the solid line (left axis), and the stress is plotted for two different values of n in the dashed lines (right axis).

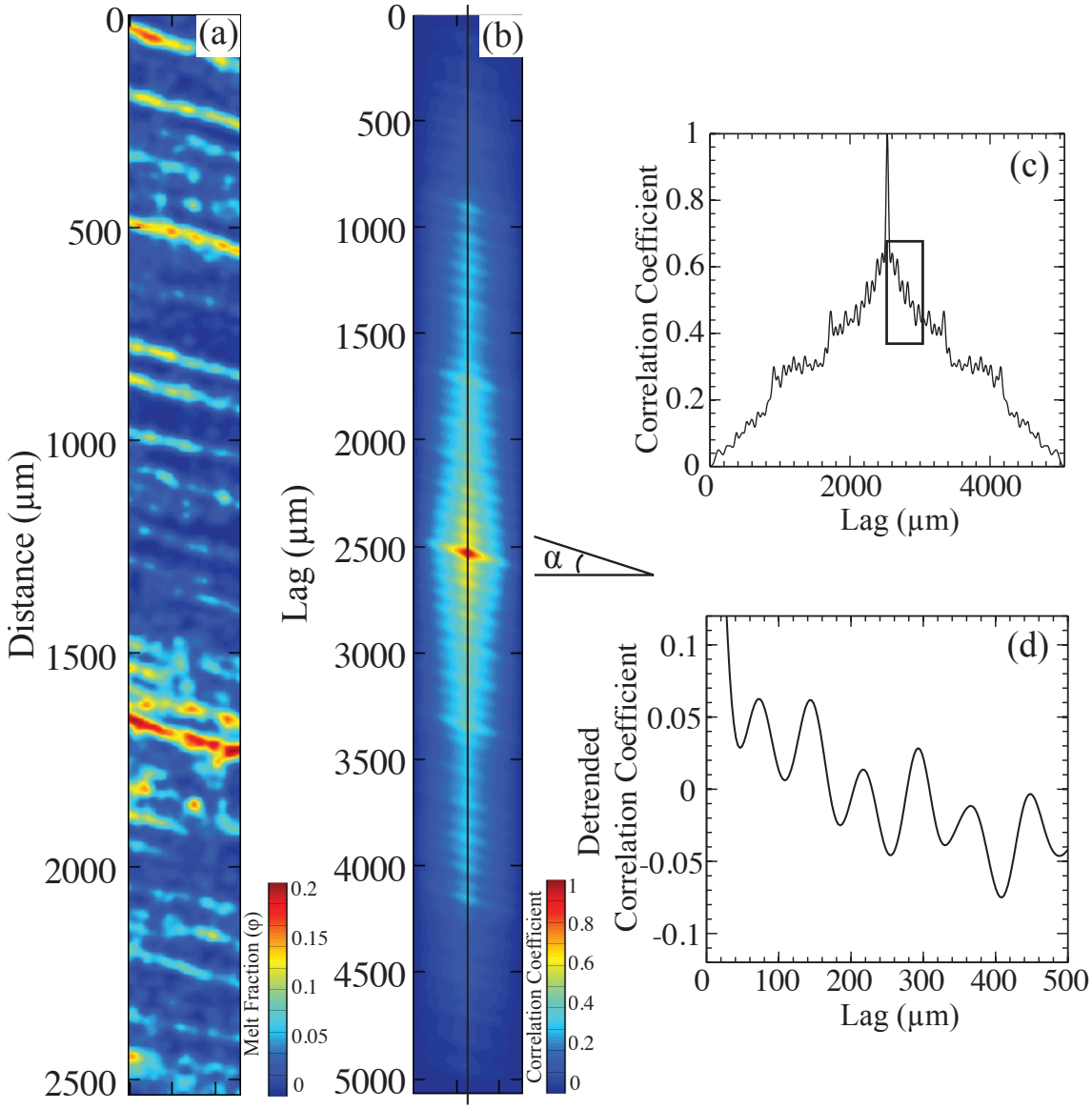

Figure 2.2: Summary of the 2-D ACF method for analyzing the spacing between bands. The example here is for the sample deformed at $\dot{\gamma} = 1.4 \times 10^{-4}\,\mathrm{s}^{-1}$ to $\gamma = 1.6$ (PT0268) (a) A smoothed binary image of a section of the tangential face mapped for normalized melt fraction. (b) The resulting matrix from the 2-D ACF of the input image in (a). The average band angle (α) determined from the ACF is indicated. (c) A profile through the 2-D ACF along the vertical line in (b). (d) The first 500 μm of Lag from (c) plotted with the linear trend removed.

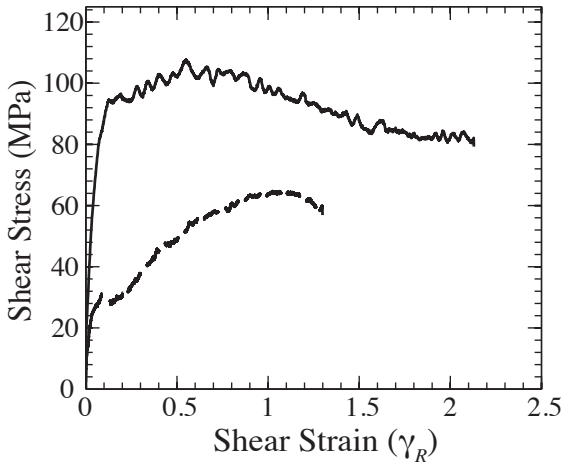

Figure 2.3: Stress-strain curves for PT0313 (solid line) and PT0323 (dashed line). The shear stress was calculated for the outer radius of the sample using Eq. 2 and n = 1.6 (see Figure 14).

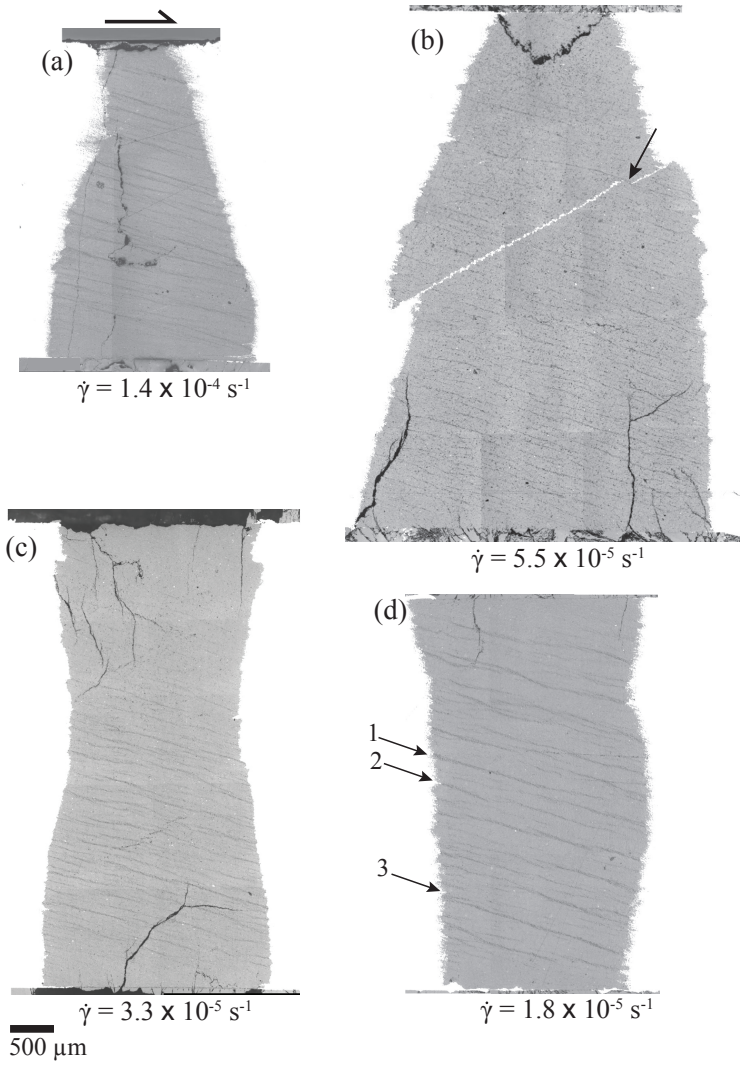

Figure 2.4: Reflected light mosaic images of tangential sections for samples in the strain rate series. All samples were sheared top-to-the-right. (a) Sample PT0268. (b) Sample PT0308. The arrow indicates an offset in the nickel foil (bright line) placed through the center of the sample before deformation as a strain marker. (c) Sample PT0297. (d) Sample PT0323. Arrow 1 points to a location where a melt-rich band is in contact with the nickel jacket and there is no indent. Arrow 2 points to a location where an indent coincides with a band. Arrow 3 points to a location where there is an indent without an associated band.

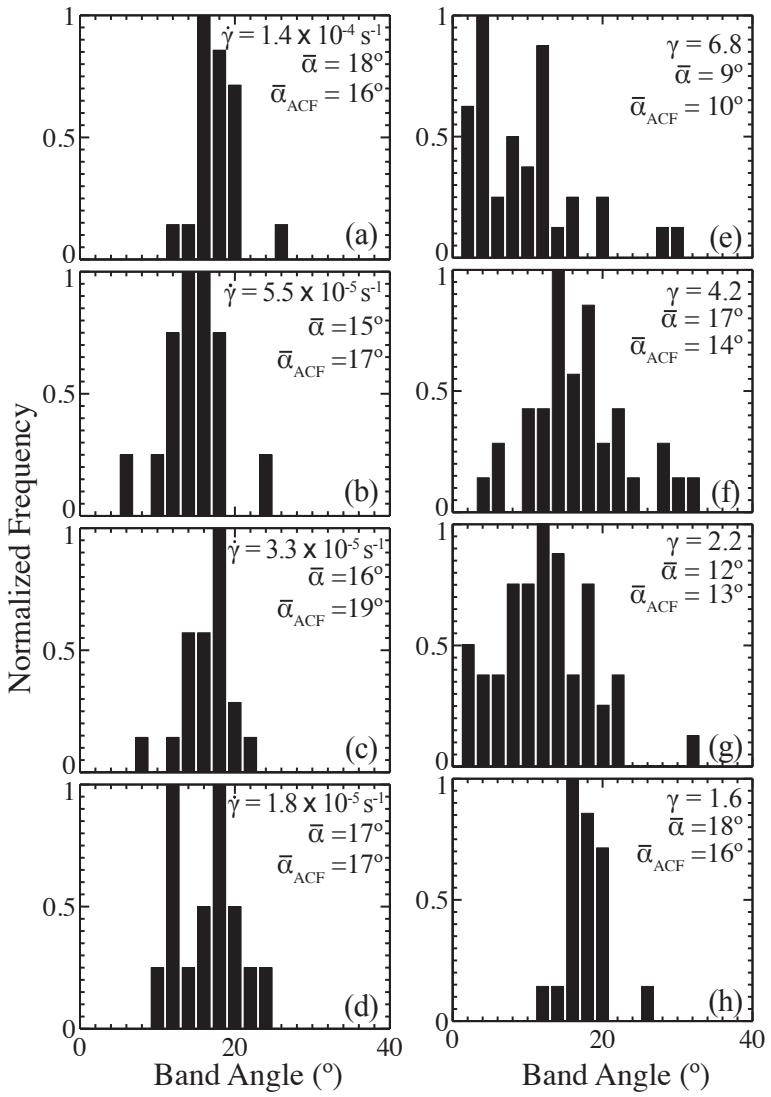

Figure 2.5: Histograms of the angle between bands and the shear plane measured from the tangential sections. The mean from the plotted data ($\bar{\alpha}$) and the mean angle determined from the 2-D ACF ($\bar{\alpha}_{ACF}$) are indicated. Results from the strain rate series are plotted in (a)-(d) and results from the strain series are plotted in (e)-(h). (a) Sample PT0268. (b) Sample PT0308. (c) Sample PT0297. (d) Sample PT0323. (e) Sample PT0329. (f) Sample PT0276. (g) Sample PT0313. (h) Sample PT0268.

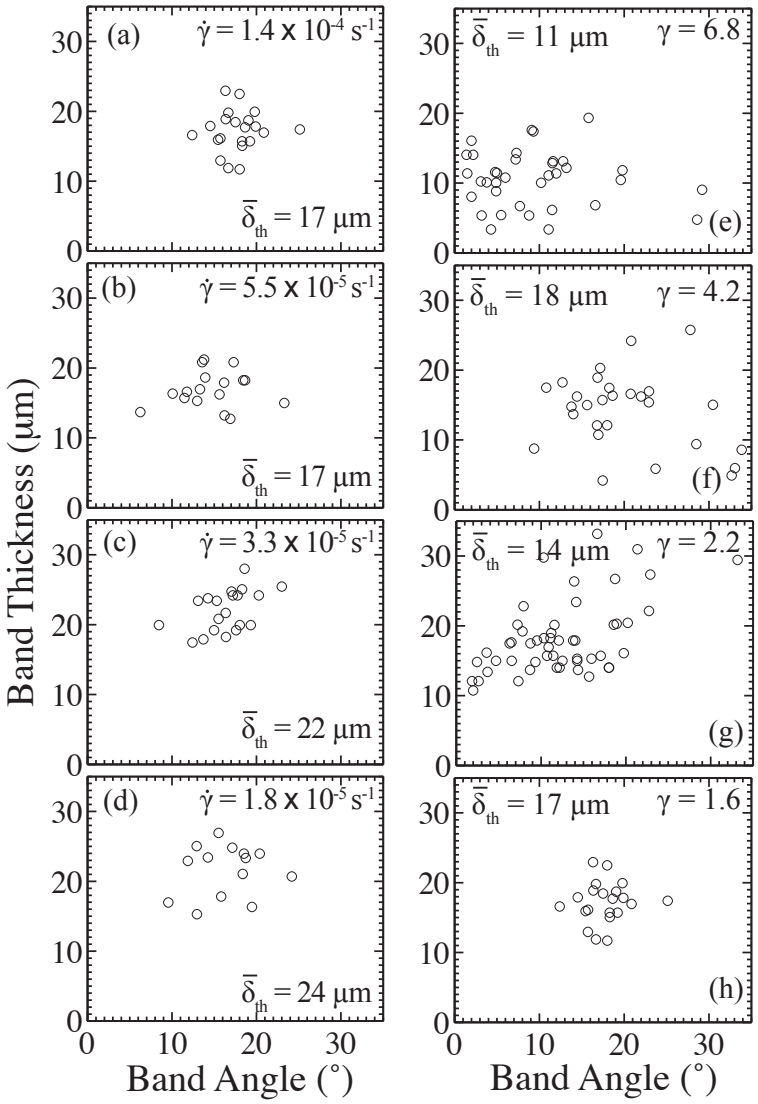

Figure 2.6: Band thickness plotted vs band angle. The mean thickness from the plotted data ($\bar{\delta}_{th}$) is indicated. Results from the strain rate series are plotted in (a)-(d) and results from the strain series are plotted in (e)-(h). (a) Sample PT0268. (b) Sample PT0308. (c) Sample PT0297. (d) Sample PT0323. (e) Sample PT0329. (f) Sample PT0276. (g) Sample PT0313. (h) Sample PT0268.

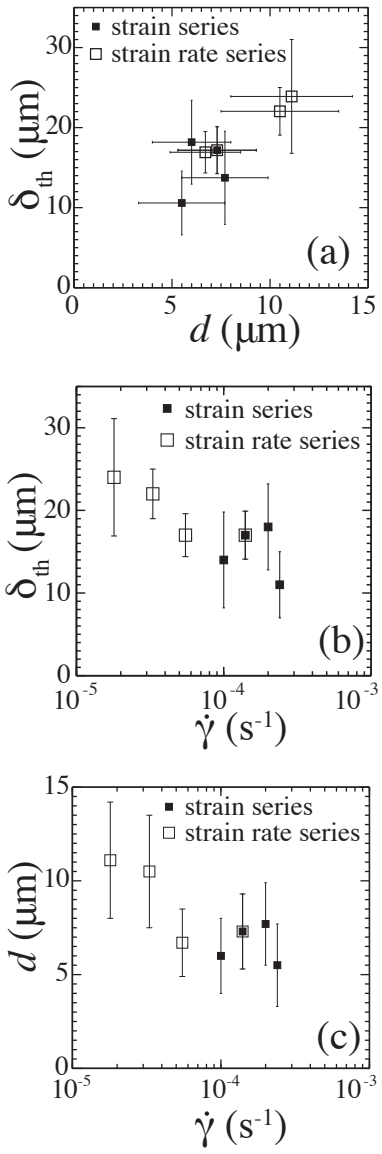

Figure 2.7: (a) Band thickness (δ_{th}) plotted vs mean grain diameter (d) measured within the bands. (b) Band thickness plotted vs shear strain rate. (c) Mean grain diameter measured within the bands plotted vs shear strain rate.

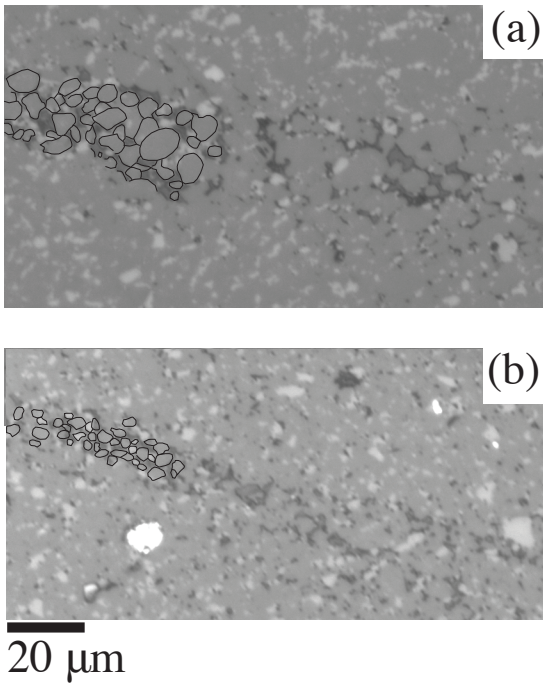

Figure 2.8: Reflected light images of melt rich bands. The brightest phase is chromite, light gray is olivine, and dark gray is quenched melt. Grains are traced in a portion of each image. Both images are at the same scale. (a) The sample deformed at $\dot{\gamma} = 1.8 \times 10^{-5}\,\mathrm{s}^{-1}$ to $\gamma_R = 1.6$ (PT0323). (b) The sample deformed at $\dot{\gamma} = 1.4 \times 10^{-4}\,\mathrm{s}^{-1}$ to $\gamma_R = 1.6$ (PT0268).

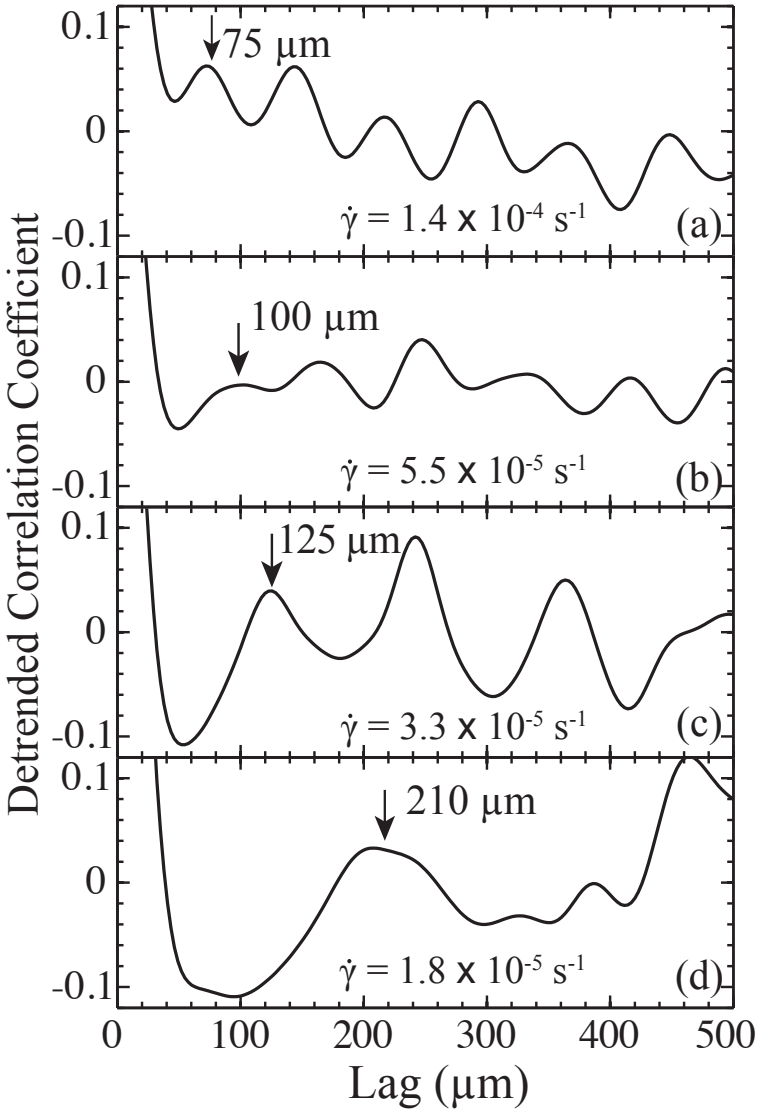

Figure 2.9: The first 500 μm of lag from a profile through the center of the 2-D ACF for the strain rate series. The arrow in each plot indicates the first peak in the function that corresponds with the preferred band spacing. (a) Sample PT0268. (b) Sample PT0308. (c) Sample PT0297. (d) Sample PT0323.

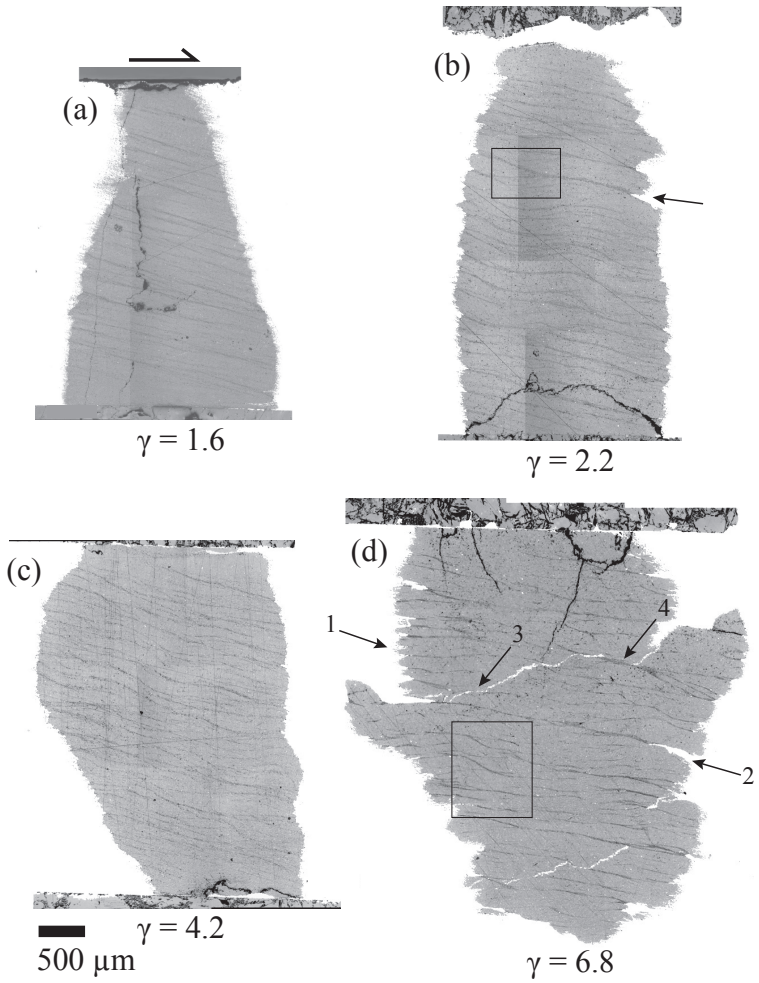

Figure 2.10: Reflected light mosaic images of tangential sections for samples in the strain series. All samples were sheared top-to-the-right. (a) Sample PT0268. (b) Sample PT0313. The melt distribution of the area inside the box is traced in detail in Figure 17. The arrow indicates a large indent along the sample jacket-interface that coincides with a thick band. (c) Sample PT0276. (d) Sample PT0329. Figure 18a is a larger image of the area inside the box. Arrow 1 points to a highly serrated region of the sample-jacket interface where all but one of the indents clearly coincides with a band. Arrow 2 indicates a large indent along the sample jacket-interface that coincides with a thick band. Arrow 3 points to a deflection of the nickel strain marker that does not clearly coincide with the presence of a band at the time of quenching. Arrow 4 indicates an offset in the nickel strain marker that coincides with a relatively thick melt-rich band.

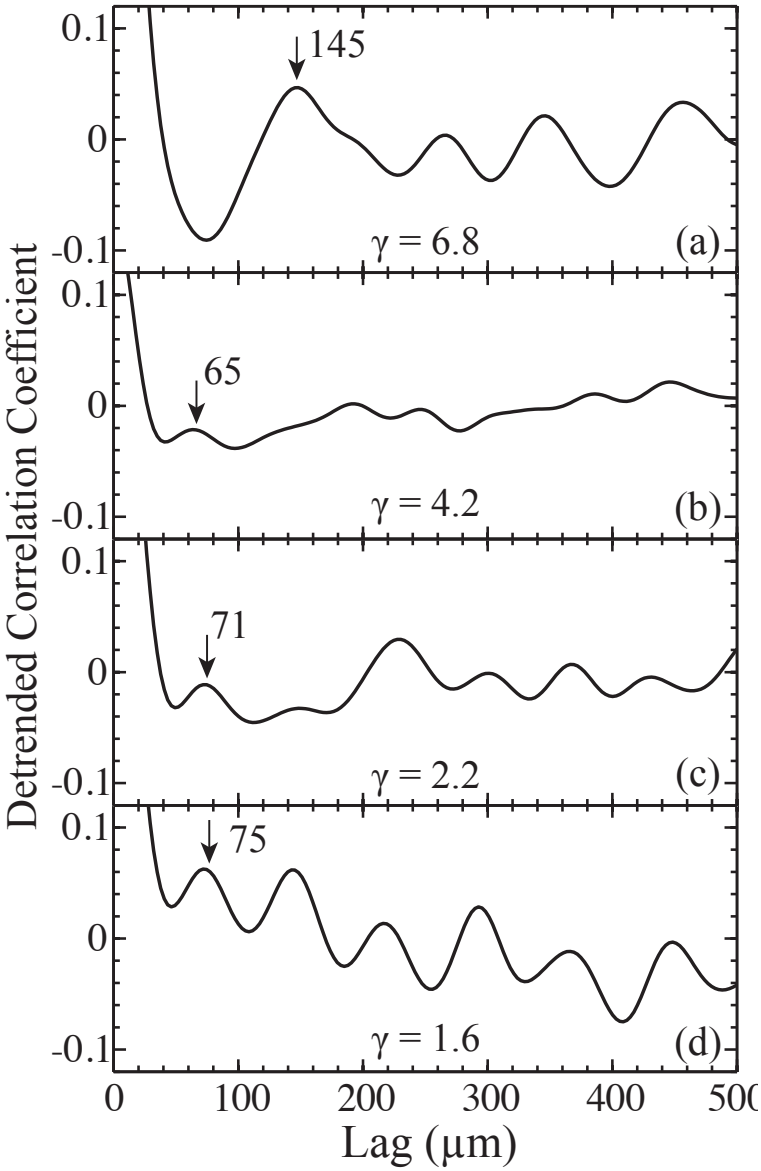

Figure 2.11: The first 500 μm of lag from a profile through the center of the 2-D ACF for the strain series. The arrow in each plot indicates the first peak in the function that corresponds with the preferred band spacing. (a) Sample PT0329. (b) Sample PT0276. (c) Sample PT0313. (d) Sample PT0268.

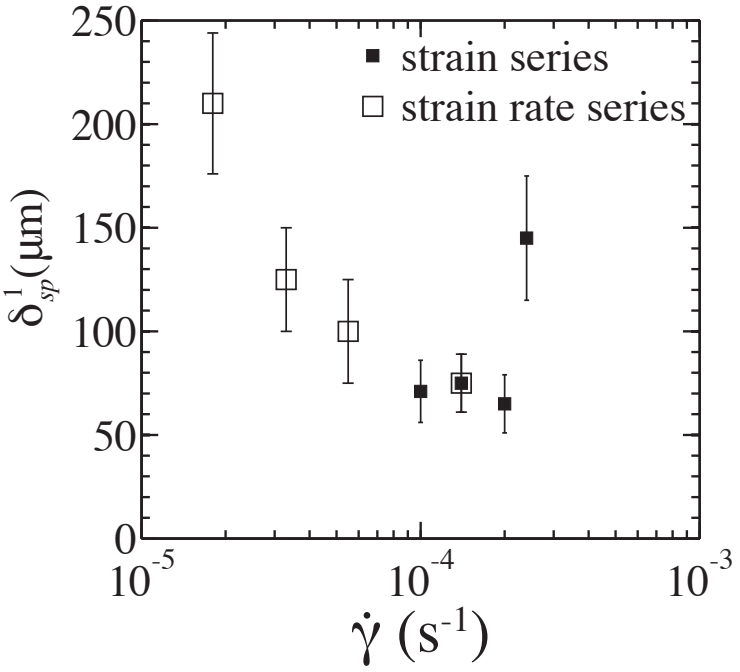

Figure 2.12: Band spacing determined from the first peak in the 2-D ACF plotted as a function of strain rate for all samples. The one outlier from the trend of decreasing band spacing with increasing strain rate is the sample deformed at $\dot{\gamma} = 2.2 \times 10^{-4}\,\mathrm{s}^{-1}$ to $\gamma_R = 6.8$ (PT0329). The error bars are the standard deviation of a normal distribution fit to the first peak in the ACF.

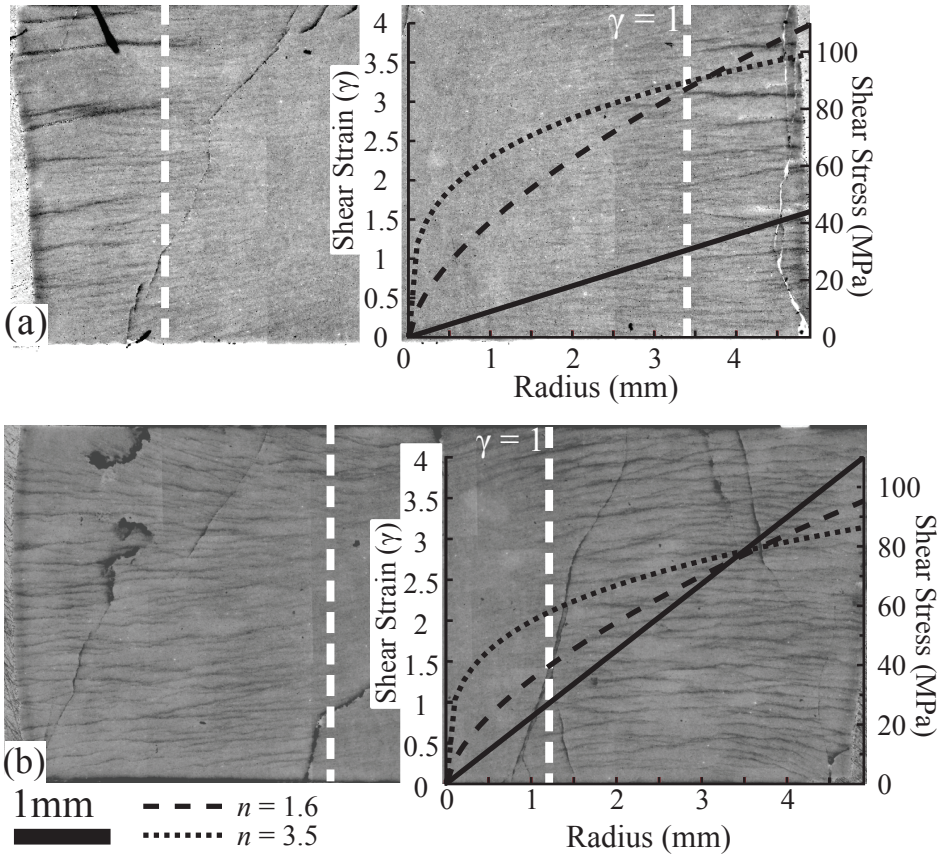

Figure 2.13: Images of two radial sections (see Figure 1a), PT0268 (a) and PT0276 (b). The strain profile is plotted in the solid line (left axis), and the stress is plotted in dashed lines (right axis) for n = 1.6 and 3.5. The vertical white dashed line is drawn at $\gamma = 1$ in both of the images. The same behavior of the band front extending to $\gamma \approx 1$ is observed in all samples in this study.

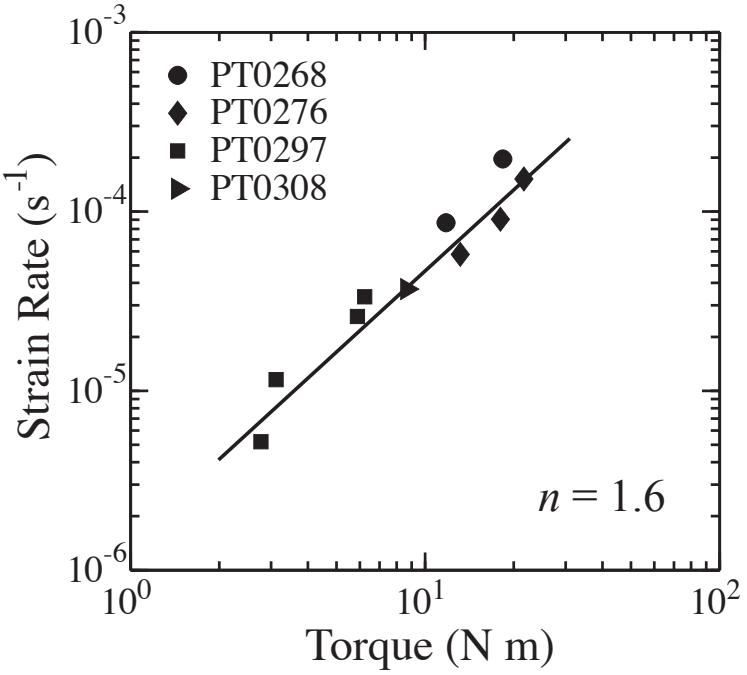

Figure 2.14: A log-log plot of strain rate ($\dot{\gamma}$) vs torque M for four samples. A least-squares fit to all of the data define a stress exponent of n = 1.6, consistent with the stress exponent defined by rate steps within individual experiments.

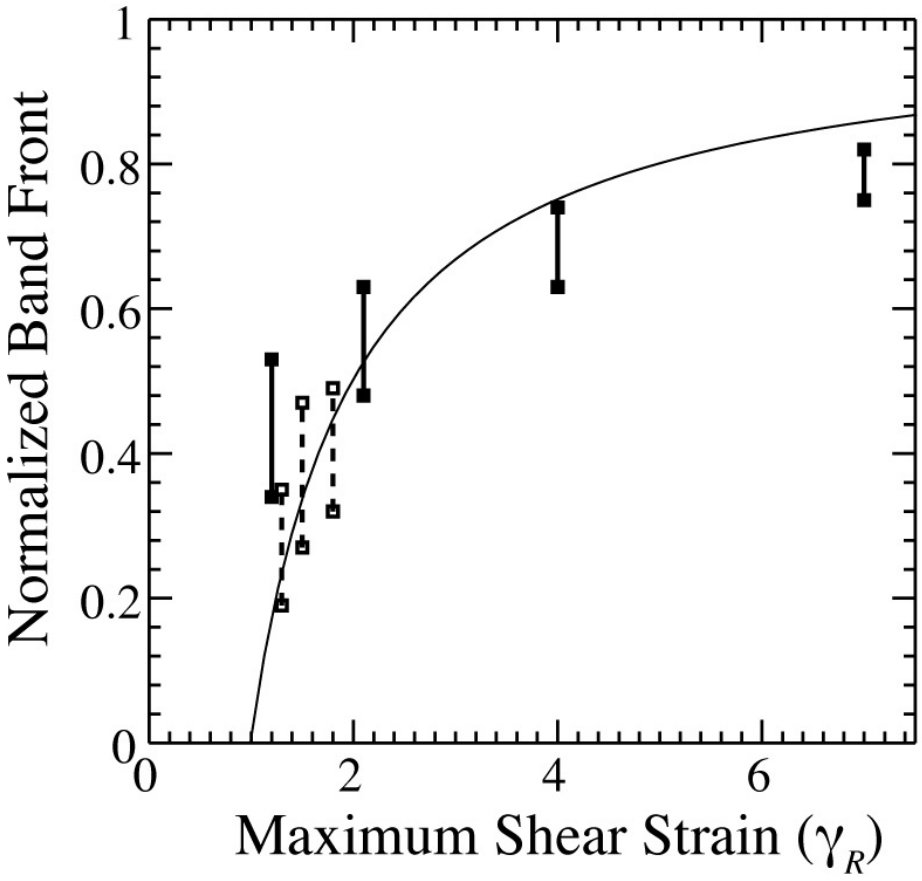

Figure 2.15: A plot of the band front vs shear strain at the outer radius of the samples. The band front is normalized to the radius of the sample, R. The line is the normalized radius at which $\gamma = 1$. Data from the strain series are plotted as solid lines and data from the strain rate series are plotted as dashed lines.

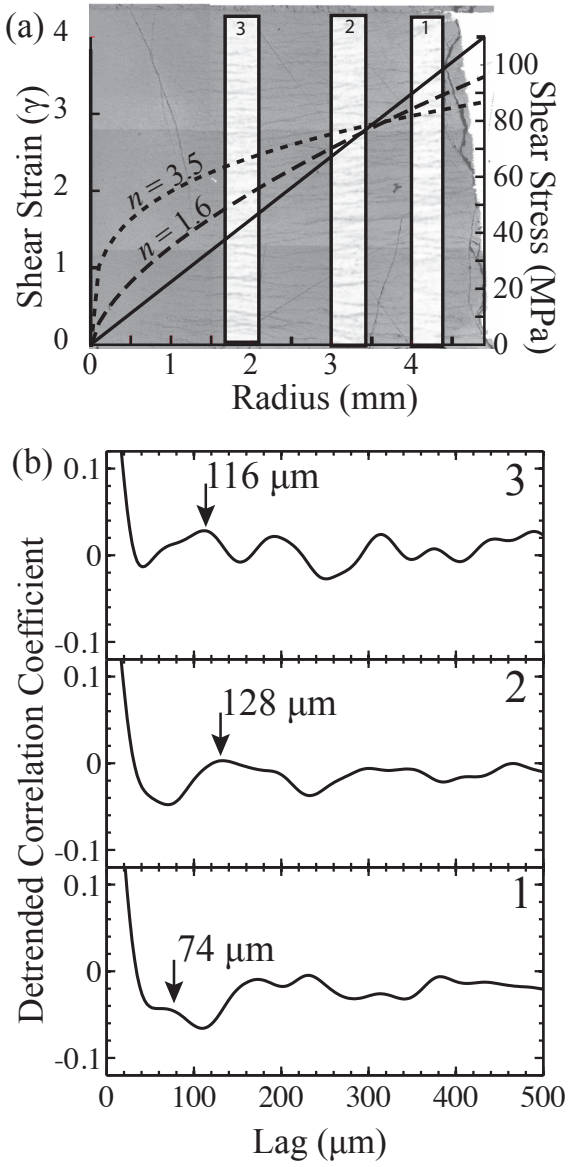

Figure 2.16: Analysis of band spacing for multiple images from the radial section of sample PT0276. (a) One half of the radial section. The strain profile is plotted in the solid line (left axis), and the stress is plotted in dashed lines (right axis) for two different stress exponents. Three smoothed binary images are superimposed. (b) The first 500 μm of Lag from a profile through the center of the 2-D ACF for the images in (a). The numbers on the plots correspond to the numbers on the images in (a) The arrow in each plot indicates the first peak in the function that corresponds with the preferred band spacing.

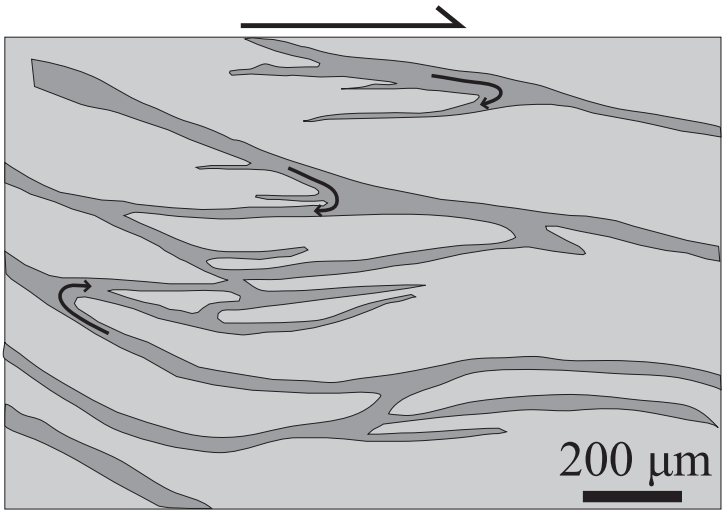

Figure 2.17: A detailed tracing of melt-rich bands from the tangential section of the sample deformed to $\gamma_R = 2.2$ (PT0313). This may be a section of the sample where the melt is reorganizing after the melt-rich bands were warped by a high-angle kink. The location where this tracing is from is indicated by a box in Figure 10b. Arrows indicate how we interpret the melt to be flowing from higher to lower angle bands.

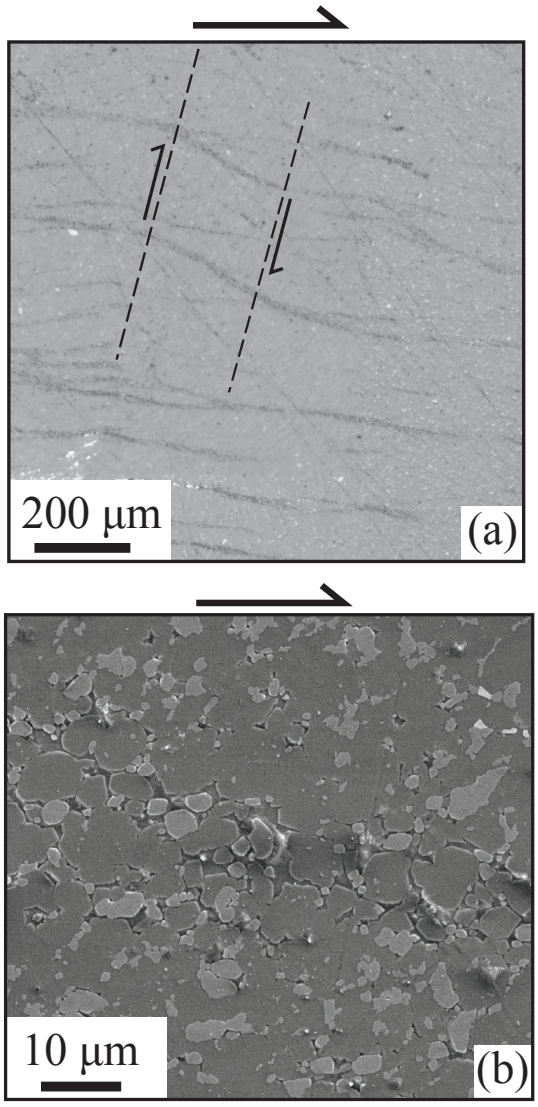

Figure 2.18: Images from PT0329 at two different scales. The brightest phase is chromite, light gray is olivine, and dark gray is quenched melt. (a) A high angle kink that warps several adjacent melt rich bands. (b) An SEM image (secondary electron) of a melt-rich band from sample PT0323. Light gray is chromite, darker gray is olivine. The bright phase in the upper right is nickel from the jacket.

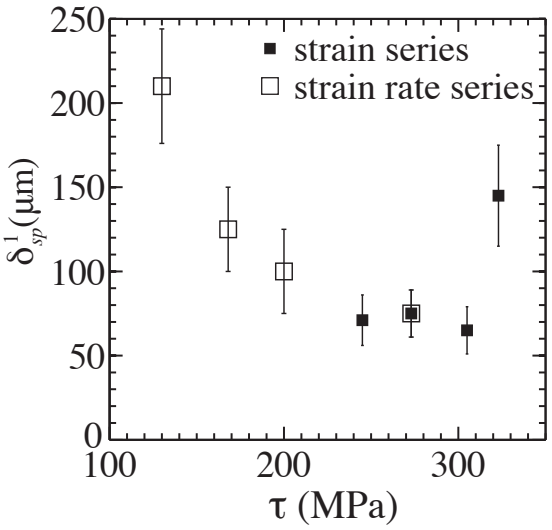

Figure 2.19: Plot of band spacing as a function of the shear stress calculated from the Hirth and Kohlstedt (2003) flow law for the lenses with reduced melt fraction. These are not the stresses calculated from the measured torque data.

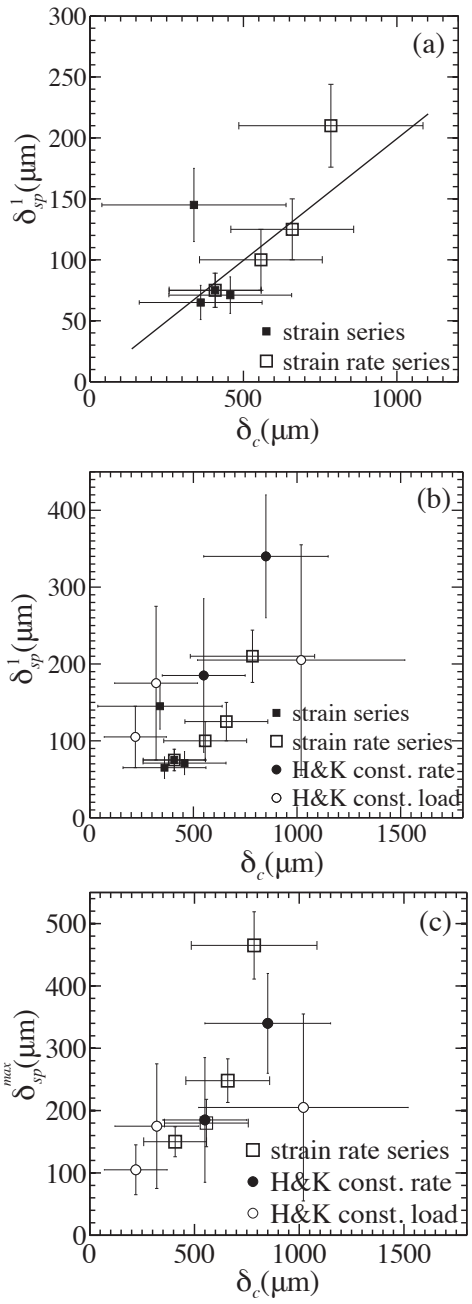

Figure 2.20: Band spacing plotted as a function of compaction length. (a) The first peak in the ACF from analyses of torsion experiments in the present study. The least squares fit through the origin with a slope of 0.2 is plotted. (b) The first peak in the ACF from the present study plotted with data from the direct shear experiments of Holtzman & Kohlstedt (2007). (c) The maximum peak in the ACF from the strain rate series plotted with data from Holtzman & Kohlstedt (2007).

Chapter 3

Stability of Melt-rich Bands: Effects of Surface Tension

Static annealing experiments were conducted on fine-grained samples of partially-molten, olivine-rich rock to determine the effects of interfacial tension driven flow in redistributing melt within the sample. A sample of fine-grained olivine + 20% chromite was prepared with an initially homogeneously distributed melt fraction of 0.04. When this sample was deformed in torsion, the melt segregated into distinct melt-rich bands uniformly spaced throughout the sample, as demonstrated in prior studies. Portions of this sample were then statically annealed for different lengths of time to observe the homogenization of melt distribution. The experimental results were compared to numerical models based on formulations for interfacial tension driven flow that do or do not include the effect of a chemical potential gradient associated with the curvature of solid-liquid phase boundaries at triple junctions. The results indicate that, at the grain size and perturbation length scales in these samples, the dissolution/precipitation and diffusive mass transfer through the liquid phase associated with the chemical potential gradient plays a significant role in accommodating interfacial tension driven flow. These experiments provide a valuable test for theory and allow us to place some constraints on the homogenization rate of melt-rich bands acting as high-permeability pathways in Earth's upper mantle.

3.1 Introduction

Interfacial tension is a critical factor in determining the distribution of melt in a multiphase aggregate. Melt distribution and grain-scale pore geometry (controlled by surface energies at grain and phase boundaries) are primary controls on melt interconnectivity and permeability (e.g., Wark & Watson, 1998), which in turn control the mechanisms and rates of melt transport in the lower crust and mantle. A small amount of melt can also significantly influence the rheological properties of a partially molten rock (Hirth & Kohlstedt, 1995a,b; Kohlstedt & Zimmerman, 1996). The effects of the melt can be especially pronounced if the melt distribution is inhomogeneous and/or anisotropic (Holtzman et al., 2003; Holtzman & Kohlstedt, 2007; King et al., 2010). Depending upon the dihedral angle, interfacial tension can either amplify or homogenize perturbations in melt fraction (Hier-Majumder et al., 2006). Improved constraints on interfacial tension driven flow are of fundamental importance to improving our understanding of the mechanisms that drive melt extraction and the formation of Earth's chemical and mechanical boundary layers.

A number of models describe the coupling of matrix deformation and fluid flow necessary to explore the rate of homogenization of perturbations in melt fraction or infiltration of melt from a source region into a sink region (e.g., Stevenson, 1986; Riley et al., 1990; Riley & Kohlstedt, 1991; Hier-Majumder et al., 2004, 2006; Takei & Hier-Majumder, 2009). Riley & Kohlstedt (1991) developed a model for melt transport in partially molten rocks driven by capillary forces in which melt transport is accommodated by coupled compaction and decompaction of the rock matrix. Riley & Kohlstedt (1991) also conducted experiments on melt migration from a melt-rich source to a melt-poor sink as a calibration of this model. Parsons et al. (2008) employed another experimental approach to explore melt migration in which partially molten samples were statically annealed after they had been deformed in direct shear to produce melt-rich bands. In these annealing experiments, the melt fraction within the bands decreased significantly, and the width of the band increased moderately. Analysis of the experimental results from the static annealing experiments using the equations from Riley & Kohlstedt (1991) yielded the permeability of the aggregate and the viscosity of the matrix that best fit the experimental data. More recently Takei & Hier-Majumder

(2009) extended existing models of surface tension flow to include the effects of dissolution/precipitation and diffusive transport of matter through the fluid phase driven by a chemical potential gradient at solid-liquid phase boundaries arising from the curvature of the interface. In their analysis, Takei & Hier-Majumder (2009) identify a diffusion length scale δ_{d}. For perturbations at a length scale longer than δ_{d} the homogenization rate from matrix compaction/decompaction is the rate controlling process, yielding results similar to those of Riley & Kohlstedt (1991). However, for perturbations at length scales shorter than δ_{d}, dissolution/precipitation with diffusive mass transport through the fluid phase is the rate controlling process, and the evolution of melt fraction is governed by a nonlinear diffusion equation.

We present data from a set of annealing experiments similar to those of Parsons et al. (2008) but with refined experimental design and improved image analysis. In Parsons et al. (2008) three different samples (of the same material used in this study) 0.5 mm in height were deformed in direct shear to a shear strain of $\gamma \approx 3.5$ and either quenched or allowed to anneal after deformation. In this study, a sample of partially molten olivine-rich rock was deformed in torsion, resulting in segregation of melt into distinct melt-rich bands (King et al., 2010). Portions of the sample were then annealed for different lengths of time to explore the evolution of the perturbations in melt fraction. The larger sample size of torsion samples ($\sim$ 4.5 mm in height) compared to direct shear samples (0.5 mm in height) allowed (1) all of the annealing experiments to be performed on portions of the same original deformation sample (2) analysis of a larger area of the sample with more melt-rich bands than in the direct shear samples used in Parsons et al. (2008). We compare the results to the model of Takei & Hier-Majumder (2009) and explore the relationship between δ_d and the perturbation length scale in the deformed and annealed samples to determine if incorporating diffusive mass transport through the fluid leads to better representation of experimental results.

3.2 Methods

3.2.1 Sample preparation and assembly

Samples were prepared by mechanically mixing olivine from San Carlos, Arizona (72 vol. %), chromite from the Semail Ophiolite, Oman (24 vol. %), and powdered MORB

glass (4 vol. %) (Holtzman et al., 2003; Holtzman & Kohlstedt, 2007; Parsons et al., 2008; King et al., 2010). The mixture was cold pressed into a nickel capsule before hot isostatic pressing for 3 h at 1200°C and 300 MPa in a gas-medium pressure vessel (Paterson, 1990). A portion of the starting material was then polished and examined by optical microscopy to verify the homogeneity of the phase distribution throughout the sample. The mean starting grain diameter of the powders was 6 μm for olivine and 2 μm for chromite. During hot-pressing, the olivine grain size grew to ~ 8 μm.

3.2.2 Experimental procedure

Experiments were performed in a gas-medium deformation apparatus equipped with a torsion actuator (Paterson & Olgaard, 2000). The initial deformation experiment was controlled at a constant torque as measured by a torque cell housed inside the pressure vessel. The rate of angular displacement to maintain this torque was controlled by a servomotor feed back loop and monitored by a rotational variable displacement transducer (RVDT) outside the pressure vessel. Temperature was monitored near the sample using a Pt-Pt/Rh thermocouple. Furnace calibrations confirm variation of < 1°C along the length of the sample. Methods for determining shear stress and shear strain rate from torque and angular displacement as a function of time have been described by Paterson & Olgaard (2000).

The experiments were designed to investigate the role of surface tension in homogenizing the melt distribution after the driving force for segregation has been removed. A cylindrical sample was deformed at a constant torque corresponding to a shear stress at the outer radius of $\tau_{max} = 90$ MPa to an angular displacement corresponding to a shear strain at the outer radius of $\gamma_{max} = 2$. After deformation the sample was cut perpendicular to the sample-piston interfaces into four wedge-shaped quarters as illustrated in Figure 3.1a. One quarter was polished on the radial section and on a longitudinal tangential section (Figure 3.1b) using diamond lapping film to 0.5 μm followed by 10 min of polishing with colloidal silica (30 nm). The other parts of the sample were each wrapped with 0.1 mm nickel foil, and spacers of Al_2O_3 the same height as the sample were prepared to fill the missing three quarters of a cylinder (Figure 3.1a). Each of these three portions of the sample was then loaded into a separate sample assemblies similar to that used for the deformation experiment. The three portions were then

annealed separately for 1, 10, and 50 h at 1200°C and 300 MPa. After annealing, the samples were polished following the same procedure used for the quenched sample. To make the melt and grain boundaries more visible in reflected light images, samples were then etched with a weak solution of HF and HCl, which preferentially etches the quenched melt phase and the grain boundaries. Mosaic images of tangential sections of the as-deformed and annealed samples are presented in Figure 3.2.

3.2.3 Image analysis

To quantitatively analyze changes in the distribution of melt with increasing anneal time, strips of optical micrographs were taken of portions of each tangential section and stitched together into a mosaic image at least 1.5 mm long and $\sim$ 0.4 mm wide. A threshold was then applied to the image to create a binary image representing the distribution of the quenched melt as illustrated in Figure 3.3. The area fraction of melt in the binary images corresponds with the volume fraction of MORB that was initially put into the sample (0.04) with error of 0.002. The images were then smoothed by centering a 2-D Gaussian filter matrix on each pixel of the image. The filter was convolved with the overlapping region of the image and then divided by the number of pixels in the smoothing matrix. Because one of the goals of this analysis was to determine the peak melt fraction within the bands, it was important to use a smoothing filter with a diameter less than the width of the bands. As reported in King et al. (2010) band thickness in a suite of similar deformation experiments is typically $\sim$ 20 μm, similar to the thickness observed in the quenched sample. A filter diameter of 16 μm was determined to be an appropriate size. A filter with a 32-μm diameter yielded significantly lower peak melt fractions in the bands.

After a smoothed image was created, five profiles were extracted similar to the profiles displayed in Figure 3.3c,f,i, and l. Peak melt fractions were tabulated for each band in each profile, with bands defined as a peak in melt fraction above the overall average melt fraction of 0.04. This method is different from that used by Parsons et al. (2008) in which three profiles were averaged together to create one average profile for the image. Because not all the bands are precisely parallel, averaging the profiles leads to averaging peaks that are out of phase with one another. The method used here accounts for variation in melt fraction along the trace of the band while measuring the

true peak from each profile.

3.2.4 Model formulation

The governing equations used in the model, non-dimensionalization scheme and details of numerical methods are given in Takei & Hier-Majumder (2009); (a summary of the governing equations are given in Appendix A). Here we summarize the key parameters that determine the growth rate λ of the initial perturbation and that determine whether the matrix deformation accommodating interfacial tension driven flow is dominated by viscous compaction/decompaction or dissolution/precipitation and diffusive mass transport through the liquid.

The critical nondimensional parameters are Pe, which is the ratio of the rate of advection to the rate of diffusion, and W, which is a measure of the driving force for dissolution/precipitation arising from a chemical potential difference. They are defined as

$$\begin{cases} Pe = \frac{Lv_0}{D_{\rm L}} \\ W = \frac{\gamma_{\rm sl}}{d}\frac{\Omega}{E} \end{cases} \tag{3.1}$$

where E is a constant (see Equation **??**), the characteristic length scale L is given by

$$L = \left(\frac{7\eta_0 k_0}{3\eta_{\rm L}}\right)^{\frac{1}{2}} \tag{3.2}$$

and the characteristic velocity v_o is defined by

$$v_0 = \frac{\gamma_{\rm sl}\phi_0 L}{d\eta_0}. \tag{3.3}$$

When $W \to 0$ and/or $Pe \to \infty$, dissolution/precipitation is negligible and interfacial tension driven flow is accommodated by matrix compaction/decompaction. In this end-member case, the nondimensional growth rate is given by

$$\lambda^*_{\rm c/d} = \frac{\frac{1}{2}(1-\phi_0)f(\theta)\phi_0^{-3/2}}{(\xi^*_0 + \frac{4}{3}\eta^*_0)(1+\frac{1}{(1-\phi_0)\phi_0^n k^{*2}})} \tag{3.4}$$

where k is the wave number and the non-dimensional bulk and shear viscosities for a reference melt fraction $\phi = \phi_0$ are given by

$$\begin{cases} \eta^*_0 = e^{-\Lambda\phi_0} \\ \xi^*_0 = \frac{1}{\phi_0^2} \end{cases} \tag{3.5}$$

and $f(\theta)$ is given by

$$f(\theta < \frac{\pi}{3}) = \left[8\cos\left(\frac{\phi}{2}\right)\sin\left(\frac{\pi}{6} - \frac{\phi}{2}\right) - 2\sqrt{3}\left(\frac{\pi}{3} - \phi\right)\right]^{\frac{1}{2}}. \tag{3.6}$$

In the other end-member case where $Pe \to 0$, dissolution/precipitation is the dominant mechanism and the nondimensional growth rate is given by

$$\lambda_{\mathrm{d/p}}{}^{*} = -k^{*2}\frac{1}{Pe}\frac{Wb\phi_0^{-1/2}}{1 - Wb\phi_0^{-1/2}}. \tag{3.7}$$

When both mechanisms are active (finite W and Pe) the growth rate of a perturbation in melt fraction is given by

$$\lambda^{*} = \frac{1 - 2bW\phi_0^{-1/2}}{1 - bW\phi_0^{-1/2}}\lambda^{*}_{\mathrm{c/d}} + \lambda^{*}_{\mathrm{d/p}}. \tag{3.8}$$

Because $bW\phi_0^{-1/2} << 0$, λ^{*} is almost equivalent to the sum of $\lambda^{*}_{\mathrm{c/d}}$ and $\lambda^{*}_{\mathrm{d/p}}$. The dimensional growth rate is calculated from this value as $\lambda = \lambda^{*}v_0/L$. Both $\lambda^{*}_{\mathrm{c/d}}$ and $\lambda^{*}_{\mathrm{d/p}}$ are negative for $\theta < 60^{\circ}$ and positive for $\theta > 60^{\circ}$.

Because $\lambda^{*}_{\mathrm{c/d}}$ and $\lambda^{*}_{\mathrm{d/p}}$ depend differently upon k^{*}, the dominant mechanism depends not only upon the material parameters but also upon the perturbation wavelength. The diffusion length δ_{d} is defined as the wavelength at which $\lambda_{\mathrm{c/d}} = \lambda_{\mathrm{d/p}}$ for $\phi = \phi_0$. It is given in dimensional form by

$$\delta_{\mathrm{d}} = 2\pi\left(\frac{dD_{\mathrm{L}}}{\gamma_{sl}} \cdot \frac{Wb\phi_0^{-1/2}}{1 - Wb\phi_0^{-1/2}} \cdot \frac{\xi(\phi_0) + \frac{4}{3}\eta(\phi_0)}{\frac{1}{2}(1-\phi_0)f(\theta)\phi_0^{-3/2}}\right)^{\frac{1}{2}}. \tag{3.9}$$

To illustrate the regions of parameter space in which the different mechanisms of interfacial tension driven flow dominate, the log of the homogenization rate ($-\lambda$) is plotted in Figure 3.4 as a function of perturbation length scale for two representative grain sizes (10 μm and 1 mm). The compaction length (δ_c) and diffusion length scale (δ_d) are plotted for each grain size. The plot demonstrates that the combined homogenization rate is controlled by the faster mechanism (compaction/decompaction or dissolution/precipitation) and that δ_d represents the length scale at which the dominant mechanism switches.

3.3 Results

3.3.1 Formation of melt-rich bands

Consistent with theory and prior studies on the same materials (Stevenson, 1989; Holtzman et al., 2003; Holtzman & Kohlstedt, 2007; King et al., 2010) and different multiphase systems with two phases of contrasting viscosity (Hustoft & Kohlstedt, 2006; Kohlstedt et al., 2010), when the sample is sheared, melt pockets first align at an angle $\sim 20^\circ$ to the shear plane antithetic to the shear direction. With increasing shear strain ($\gamma > 1$ for the materials and deformation conditions in this study), melt segregates into distinct melt-rich bands of approximately the same orientation as the melt pockets leaving behind lenses of material depleted in melt. For more details of observations of melt segregation in a suite of torsion samples see Chapter 2.

3.3.2 Evolution of melt-rich bands during static annealing

Results from image analyses of the quenched and annealed samples are presented in Table 3.2. The average melt fraction in the melt-rich bands after deformation is 0.34, with some of the most melt-rich bands reaching a maximum melt fraction of 0.50 over a small portion of the band. Other quenched torsion samples from King et al. (2010), which were polished on multiple tangential sections, revealed that on average the melt distribution is identical at a given radius around the whole sample. On this basis, we conclude that the properties observed in the quenched sample represent the starting microstructure for the subsequently annealed portions of the deformed sample.

The melt distributions in samples annealed for different lengths of time are compared in the reflected light and binary images of representative bands in Figure 3.5. During 50 h of anneal time, the mean peak melt fraction in the bands decreased from 0.34 to 0.14, with the final melt fraction in the bands still more than three times the average starting melt fraction before deformation. The background melt fraction in the non-band regions increased during the 50 h anneal from 0.0053 to 0.027, as it must since the overall melt fraction in the sample remains constant throughout the experiment. The peak melt fraction, plotted as a function of anneal time in Figure 3.6, drops more rapidly at the beginning of the anneal than later in the anneal.

The mean thickness of many bands from each of the annealed samples as measured from the full width at half maximum in the melt profiles, is presented in Figure 3.7. The data reveal that band thickness increases systematically with increasing anneal time, but the increase in thickness is minimal, that is, the mean band thickness remains nearly constant. Though the bands in the images from annealed samples in Figure 3.5 could have started with slightly different thicknesses in the quenched sample, these images of typical melt-rich bands visually demonstrate the consistent band thickness.

3.3.3 Grain size

Because grain size is an important parameter in the permeability and a critical length scale in the model, it is important to determine if the grain size evolved significantly during the long-anneal experiment. Grain size was obtained by a linear intercept method. Several lines were drawn across optical reflected light images of polished sections that had been etched with a weak acid solution. The distance was then measured between each intersection of a line with grain boundaries. At least 100 measurements were used for each sample. The measurements were multiplied by a factor of 1.5 to estimate the average grain diameter (Gifkins, 1970). As illustrated in the histograms of grain diameter plotted in Figure 3.8, the mean grain size increases systematically with increasing anneal time but only by 1 μm during the 50 h anneal. These results indicate that chromite pins olivine grain boundaries and prevents much of the grain growth that would occur in a single phase material.

3.3.4 Model results

Model runs were performed to explore surface tension driven flow accommodated by matrix compaction/decompaction alone and with dissolution/precipitation. Results of numerical simulations for two different reference shear viscosities are plotted as differential melt fraction versus anneal time in Figure 3.9, with differential melt fraction defined as the difference between the peak melt fraction in the bands ($\phi_{\max}$) and the minimum melt fraction in the non-band region ($\phi_{\min}$) normalized to the initial difference between peak and background melt fraction:

$$\Delta\phi = \frac{\phi_{\max} - \phi_{\min}}{\phi^0_{\max} - \phi^0_{\min}}. \tag{3.10}$$

For the compaction/decompaction end-member, the model predicts a more gradual decrease in differential melt fraction with increasing anneal time than in the model runs incorporating dissolution/precipitation. With decreasing reference viscosity for the melt-free solid, the bands drain more rapidly. Model runs that include the effects of dissolution/precipitation predict more rapid draining of the bands than compaction/decompaction alone.

Along with the model results, $\Delta\phi$ vs anneal time is plotted for this study and for Parsons et al. (2008). In Figure 3.9a, ϕ^0_{max} and ϕ^0_{min} are taken from the quenched sample, while in Figure 3.9b they are taken from the 1 h hour anneal. For the Parsons et al. (2008) data set a value for $\Delta\phi$ at 1 h is projected by a linear interpolation between the values for the quenched sample and the 10-h anneal. The significance of this comparison in Figure 3.9a and b is discussed below.

3.4 Discussion

3.4.1 Comparison of model results with experimental data

Predicted mechanism of surface tension driven flow

As discussed in the methods section, the predicted rate-controlling mechanism of surface tension driven flow (compaction/decompaction or dissolution/precipitation) depends upon viscosities of the solid and fluid, the permeability of the aggregate, interfacial energy, grain size and the wavelength of the perturbation in melt fraction. In Figure 3.10, δ_d is plotted as a function of grain size for $\phi_0 = 0.01$. The dashed box on the plot indicates the range of δ_d for the grain size and melt fraction in the experimental sample. The model of Takei & Hier-Majumder (2009) predicts that interfacial tension driven fluid flow is dominated by compaction/decompaction for melt perturbations with wavelengths longer than δ_d, while dissolution/precipitation is the dominant mechanism for perturbations with wavelengths shorter than δ_d. The value of δ_d calculated for the sample is significantly longer than the thickness of and spacing between melt-rich bands. Therefore, the dissolution/precipitation mechanism is predicted to be dominant.

Evolution of differential melt fraction

Although the absolute measurements of melt fraction are significantly different between this study and that of Parsons et al. (2008), the differential melt fraction records similar patterns in the evolution of melt distribution. In both studies, the rate of decrease in differential melt fraction decreases with increasing anneal time. Comparison of the evolution of $\Delta\phi$ with anneal time measured from the samples with the model results indicates that the incorporation of dissolution/precipitation is important to accurately represent the experimental data. The model results for a reference viscosity of $\eta_0 = 4 \times 10^{12}$ Pa s fit the experimental data quite well, particularly when $\Delta\phi$ is calculated using reference values from the 1 h anneal (Figure 3.9b). As discussed in more detail below, the melt distribution in the 1-h anneal may be the most appropriate starting condition when comparing the results to the model because different processes may be acting at very short anneal times compared to anneal times > 1 h due to the very high melt fraction in portions of the bands immediately after quenching.

Perturbation wavelength

Using the first-order growth rate of a perturbation (derived in Appendix A), where t^* is nondimensional time dimensionalized by $t = t^* \frac{L}{v_0}$,

$$\Delta\phi = e^{\lambda^* t^*} \tag{3.11}$$

(homogenization rate for $\lambda^* < 0$) for λ corresponding to a variety of perturbation wavelengths, it is possible to determine the perturbation wavelength that best fits the experimental data. A least squares fit of perturbation wavelength to the experimental data yields 4×10^{-4} m. The perturbation dissipation is plotted in Figure 3.11. This best fit perturbation wavelength is very close to the average band spacing in the sample of 2×10^{-4} m, suggesting that it is the spacing rather than the thickness of the melt-rich regions that determines the mechanism and rate of homogenization and that the rate limiting step is the flow of melt through the low melt fraction non-band regions. The implication of this result is that the value of δ_d, which gives the length scale that separates the two regimes of surface tension flow, should be calculated for the melt fraction in the non-band region. The value of δ_d in the non-band region, indicated by the dashed

box in Figure 3.10, is close to 2×10^{-3} m. The fact that the best fit perturbation wavelength is less than the estimated value of δ_d is consistent with the results of the model fit to the experimental data. This result is consistent with the conclusion in Chapter 2 that the spacing of melt-rich bands that form from stress-driven melt segregation is controlled by the compaction length within the non-band regions.

The disaggregation melt fraction

One possible reason why the model provides a better fit to the data normalized to $\Delta\phi$ in the 1-h anneal rather than to the data normalized to the quenched sample is that, due to the very high melt fractions in the melt-rich bands, a different physical mechanism could allow for rapid draining during the early stages of annealing. Above the disaggregation melt fraction the geometry of the melt phase changes from tubules connected along triple junctions to sheets of melt along interfaces between two grains. The theoretical disaggregation melt fraction ϕ_c for hexagonal grains from Takei & Hier-Majumder (2009) is given by

$$\phi_c = \left[\frac{f(\theta)}{4\sin(\frac{\pi}{6} - \frac{\pi}{2})}\right]^2. \tag{3.12}$$

For dihedral angles of $25-31^\circ$ as observed by Mei et al. (2002), the disaggregate melt fraction is expected to be 0.38-0.42. However, a dramatic change in rheological behavior of partially molten peridotite was observed at lower melt fractions between 0.25 and 0.30 by Scott & Kohlstedt (2006) suggesting that a significant change in the nature of the melt network occurs at this rheologically critical melt fraction. The disaggregation melt fraction based on Equation 3.8 is plotted as a function of dihedral angle in Figure 3.12. The observed mean peak melt fraction in the bands of the quenched sample is marked with error bars representing one standard deviation. The average olivine-olivine-basalt dihedral angle observed in Mei et al. (2002) is also indicated on the plot. While the mean peak melt fraction in the bands is below the disaggregation melt fraction for the expected dihedral angle, some of the bands with the highest melt fraction are in the disaggregation regime. After 1-h of anneal time all measurements of melt fraction within the bands were below the disaggregation melt fraction.

Predictions from numerical modeling are unclear regarding the pressure gradients that exist in association with a region of material above the disaggregation melt fraction.

The formulation of Hier-Majumder et al. (2006) predicts that above the disaggregation melt fraction regions enriched in melt become low pressure zones into which more melt flows, amplifying the perturbation in melt fraction. However, numerical models of a deforming crystal suspension demonstrate a regime in which the yield strength of the material depends upon the crystal fraction, even when the melt fraction is well above the rheologically critical melt fraction (Saar et al., 2001). This behavior results from the formation of load-bearing networks of solid grains within the crystal suspension. The experimental results presented here suggest that it may be important to incorporate such behavior into models of surface tension-driven flow.

3.4.2 Implications

Formation and stability of melt-rich channels in Earth's oceanic upper mantle

One question we can address with the results of this study is whether or not melt-rich conduits can remain stable over geologically significant time scales without a continuous driving force to sustain them. In an analysis of the thickness of melt-rich bands formed from stress-driven melt segregation, Takei & Hier-Majumder (2009) determined a minimum band thickness below which the homogenization rate resulting from interfacial tension driven flow is greater than the segregation rate resulting from deformation. At a grain size of 1 mm and a differential stress of 10 MPa, this minimum band thickness is ~ 1 cm. But, over what time scales are thicker bands stable?

The model results can be scaled to the region of partial melting beneath an oceanic spreading center in peridotite upper mantle by extrapolating in grain size, perturbation wavelength, and viscosity using the first-order approximation of dissipation rate (Equation **??**). In Figure 3.13, the dissipation rate of $\Delta\phi$ with time is plotted for a grain size of 1 mm as a function of perturbation wavelength. We can define a value of $\Delta\phi = 0.1$ for which the perturbation in melt fraction is considered to be homogenized. The time to homogenization is plotted on the left axis of Figure 3.13. Across a wide range of length scales (from 10 m to 100 m), the homogenization time is relatively constant at ~ 150 My; at longer wavelengths, the homogenization time is even greater. For these wavelengths, surface tension driven flow should be very small compared to the driving force

for segregation. Even if the initial mechanism forming the bands (some combination of deformation-driven and reaction-driven infiltration) was relatively short-lived, surface tension driven flow would not homogenize these high-permeability pathways within the length of time they are at high temperature. For perturbations less than $\sim$ 10 m, dissolution/precipitation plays a significant role in homogenizing the melt distribution and the homogenization time depends significantly upon the perturbation wavelength. Surface tension driven flow for perturbations at the shortest length scales ($\leq$ 1 m) may compete with the driving force for segregation and prevent channels at this scale from developing.

By comparing this calculation with observations of the width distribution of dunites from natural ophiolites, we can determine if the wavelength dependence of homogenization rate appears in the geological record. Based on measured thicknesses of dunite bands in the Oman ophiolite, Braun & Kelemen (2002) determined a scale-invariant power law distribution across several orders of magnitude in band thickness. Though their observations span from 3 mm to 100 m, the power law distribution applies most robustly to band thickness of $\sim$3 cm to 50 m. The calculation plotted in Figure 3.13 demonstrates that the significant effects of surface tension driven flow at short perturbation length scales could account for the deviation from the power law distribution at small length scales.

Lower crustal migmatites

The same type of analysis described above could be extended to other systems, such as lower crustal granulites. Migmatites are often observed in which evidence for segregation of melt into layers of very high melt fraction is recorded (e.g., Brown, 2006). Consider an aluminous metapelitic granulite for which many studies of pressure temperature paths exist (e.g., White & Powell, 2002). While melt generation depends upon many factors, most importantly the availability of H_2O, observations from natural rocks indicate that a significant amount of melt ($>$ 10 vol%) is present only at temperatures above 800°C (Brown, 2006). A typical clockwise P-T path for a granulite facies metapelite brings the rock above 850°C at pressures ranging from 400-800 MPa (White & Powell, 2002). The solidus at which melt quenches (or at which an assemblage indicative of melt would be preserved) depends upon the rate of melt loss during cooling. This solidus is predicted

to be 680°C for low melt loss (less than 70% melt loss) and 740°C for higher melt loss (White & Powell, 2002). We can use the model of surface tension driven flow to estimate the cutoff cooling rate between "fast cooling", which would allow the preservation of evidence for melt-rich layers, and "slow cooling", which would allow time for melt to be homogenized. Taking the same material parameters used in the analysis above, we determine that a perturbation at a 1-m length scale would homogenize in $\sim$ 10 My. From this estimate, we can determine that migmatite features would be preserved in rocks with low melt loss when they cool faster than 17°C/My and in rocks with high melt loss when they cool faster than 9°C/My.

3.5 Conclusions

The experiments presented here demonstrate the nonlinear dissipation of differential melt fraction driven by surface tension during static annealing of a sample in which melt distribution was inhomogeneous due to stress-driven melt segregation. At the grain size in the experimental samples and with the perturbation length scale of either the band thickness or the band spacing, the model of Takei & Hier-Majumder (2009) predicts that dissolution/precipitation and diffusive transport of matter through the fluid phase is the dominant and rate-controlling mechanism of surface tension driven flow. Numerical simulations of the formulation incorporating dissolution/precipitation provides a much better fit to the data than does the formulation consisting of surface tension driven flow accommodated only by matrix compaction/decompaction. Extrapolation of the model to the upper mantle predicts that surface tension driven flow should not inhibit the preservation of melt-rich pathways with a wide range of perturbation length scales > 1 m over geologically significant time scales. However, surface tension could prevent the formation of the smallest length-scale melt-rich channels.

Table 3.1: Material Parameters

Parameter	Units	Physical Meaning	Value
k_ϕ	m^2	Permeability	$k_\phi = \frac{d^2\phi^2}{b_k}$
b_k	nondim.	Permeability Constant	10^3 (10^4 with chromite)
η	Pa s	Solid viscosity (for $d = 10\mu m$)	$4 \times 10^{13} e^{-\Lambda\phi}$
Λ	nondim.	Constant in η	26
D_L	m^2/s	Diffusion coefficient	5×10^{-11}
η_L	Pa s	Liquid viscosity	10
γ_{sl}	J/m^2	Surface energy of solid/liquid interface	0.5
Ω	m^3/mol	Molar volume of solid phase component	0.5×10^{-4}
$E \simeq RT$	J/mol	Energy constant	1.2×10^4
b	nondim.	constant in eq. 7	0.216
ϕ_0	nondim.	Reference melt fraction	0.01

Table 3.2: Experimental Results

Sample	ϕ_{max}	ϕ_{min}	grain size (μm)	FWHM (μm)
Quench	0.34 ± 0.11	0.0053 ± 0.0025	7.8 ± 3.1	17.7 ± 5.7
1 hour	0.27 ± 0.09	0.015 ± 0.0052	8.0 ± 3.1	18.5 ± 4.4
10 hour	0.19 ± 0.08	0.018 ± 0.0095	8.7 ± 3.6	19.2 ± 5.9
50 hour	0.15 ± 0.06	0.027 ± 0.0051	9.0 ± 3.4	20.0 ± 6.6

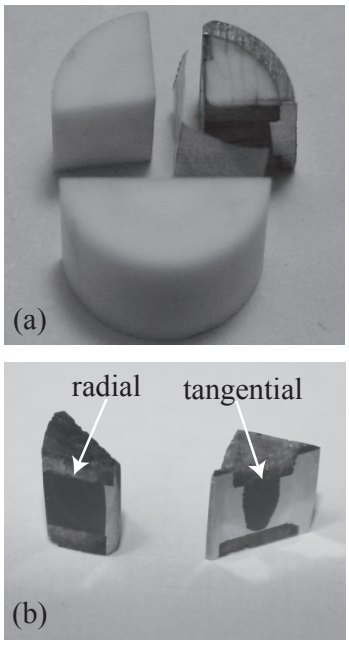

Figure 3.1: After deforming a cylindrical sample in torsion, the sample was cut into quarters. (a) Photo of the setup for annealing each quarter separately. Exposed surfaces are covered with nickel foil and alumina spacers are used to recreate a cylinder. (b) After annealing, longitudinal radial (left) and tangential (right) sections are polished.

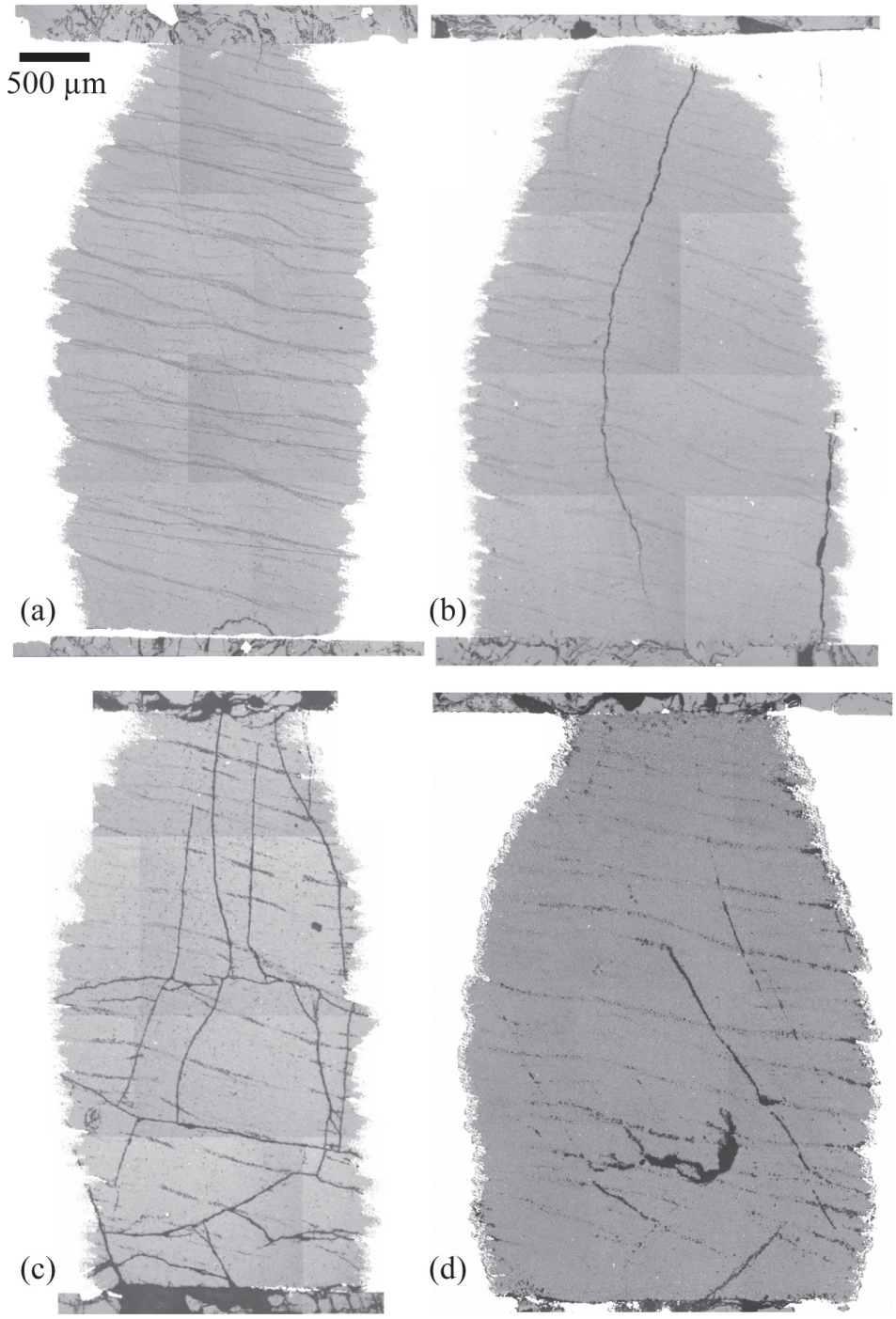

Figure 3.2: Reflected light optical images of longitudinal tangential sections of portions of the sample annealed for different lenths. (a) Quenched sample. (b) 1 hour anneal. (c) 10 hour anneal. (d) 50 hour anneal.

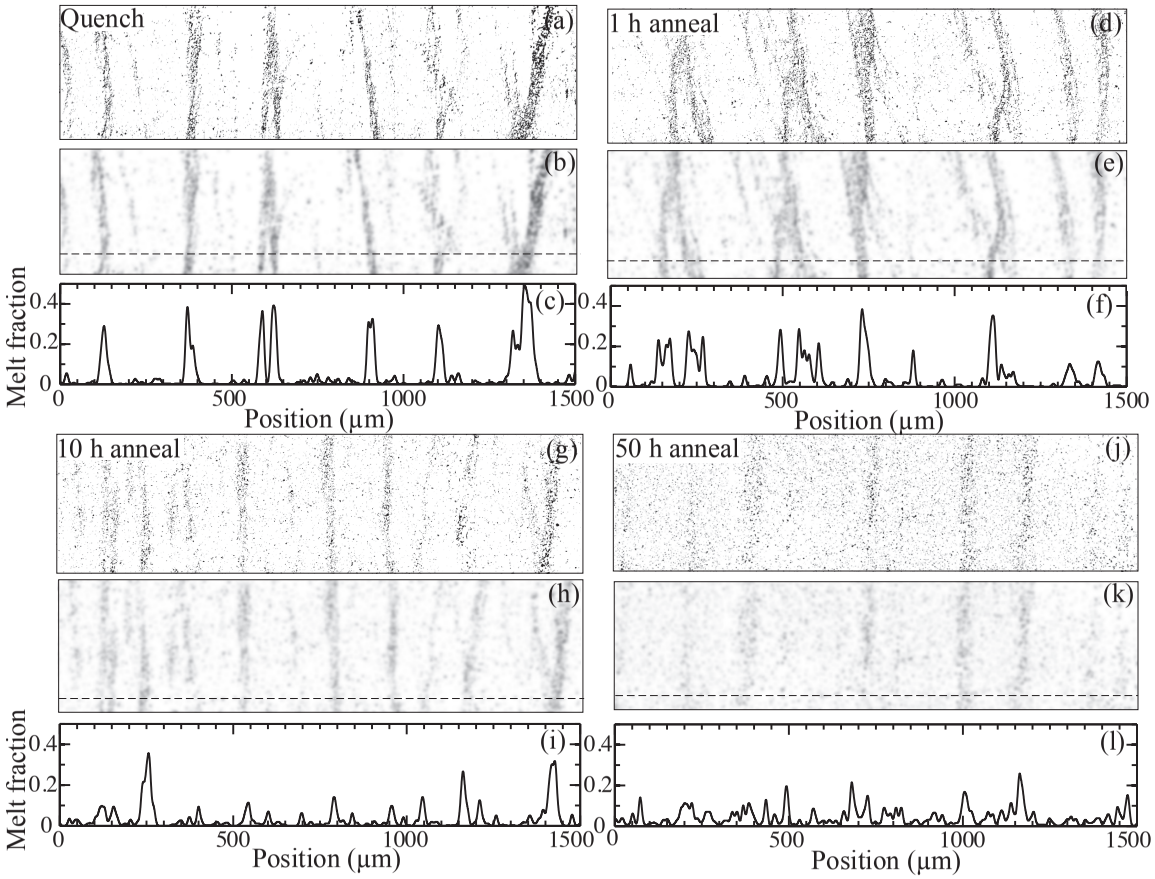

Figure 3.3: Method of extracting data from images. Binary images (a,d,g,& j) were created by applying a threshold to reflected light micrographs of polished and etched sections. Smoothed images (b,e,h, & k) were created by applying a 2D Gaussian smoothing filter to the image. Representative plots of the melt fraction as a function of distance (in μm) are displayed for the dashed line on the smoothed images (e,f,i, & l). Several plots like these were used to account for variability along the trace of the bands in the images.

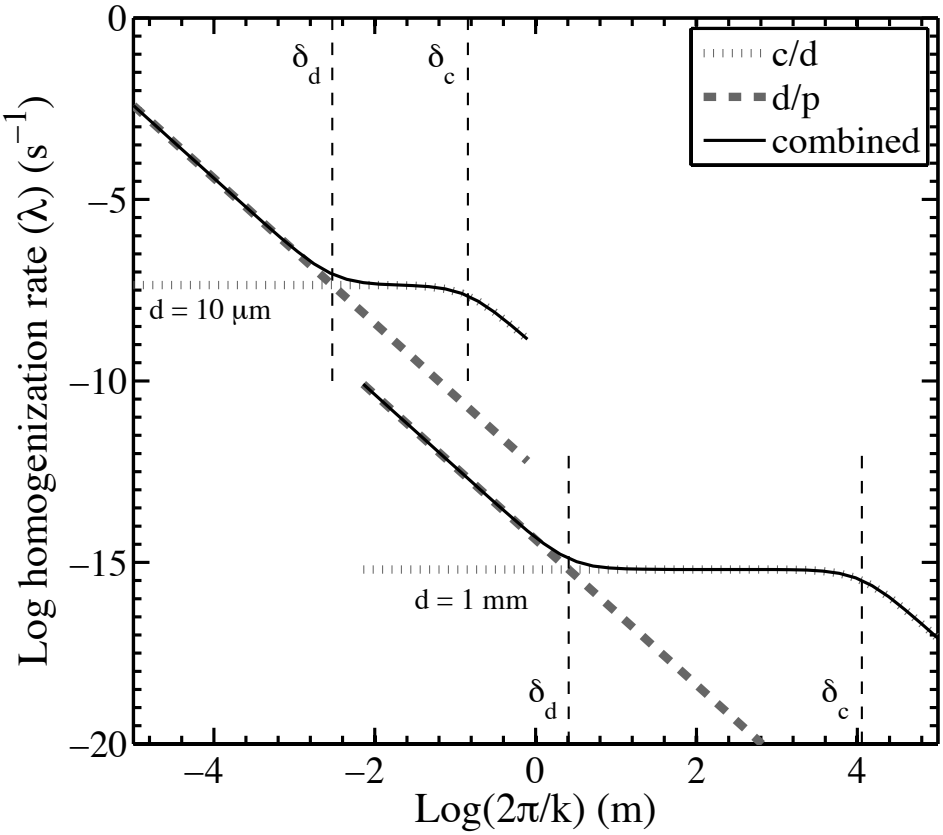

Figure 3.4: Perturbation homogenization rate ($-\lambda$) plotted as a function of perturbation length scale ($2\pi/k$) for compaction/decompaction, dissolution/precipitation, and both processes combined for grain sizes of 10 μm and 1 mm. The diffusion length (δ_d) and compaction length (δ_c) are plotted for each grain size as vertical dashed lines. At length scales shorter than δ_d, dissolution/precipitation is the dominant mechanism of surface tension driven flow, while compaction/decompaction dominates at longer length scales. (Modified from Takei & Hier-Majumder (2009) Figure 3).

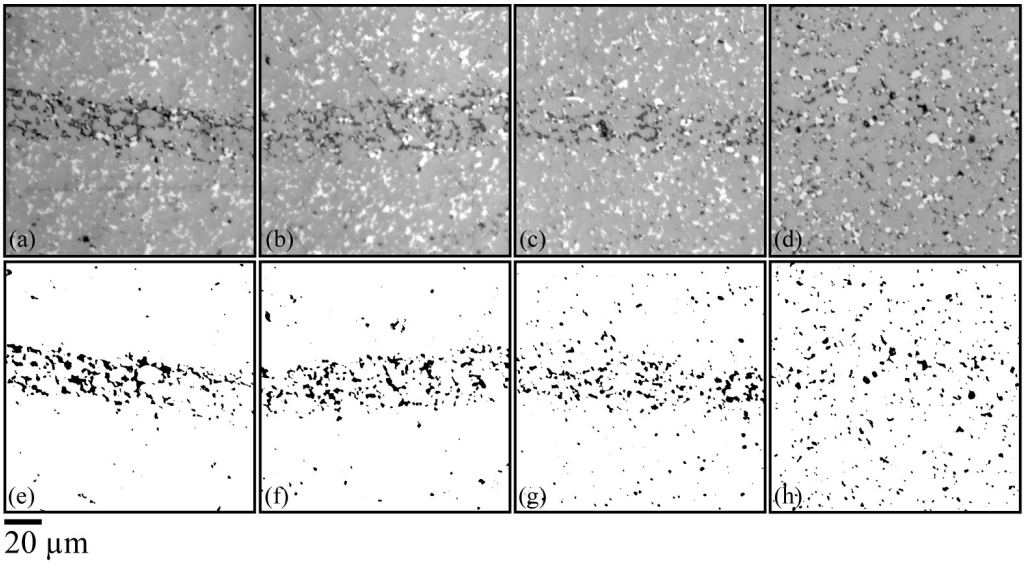

Figure 3.5: Reflected light optical images (top row) and binary images with melt shown as black created from them (bottom row) for representative bands from the quenched sample (a & e) the 1 hour anneal (b & f) the 10 hour anneal (c & g) and the 50 hour anneal (d & h). In the optical images, white is chromite, light grey is olivine, and the darkest color is where quenched glass has been chemically etched.

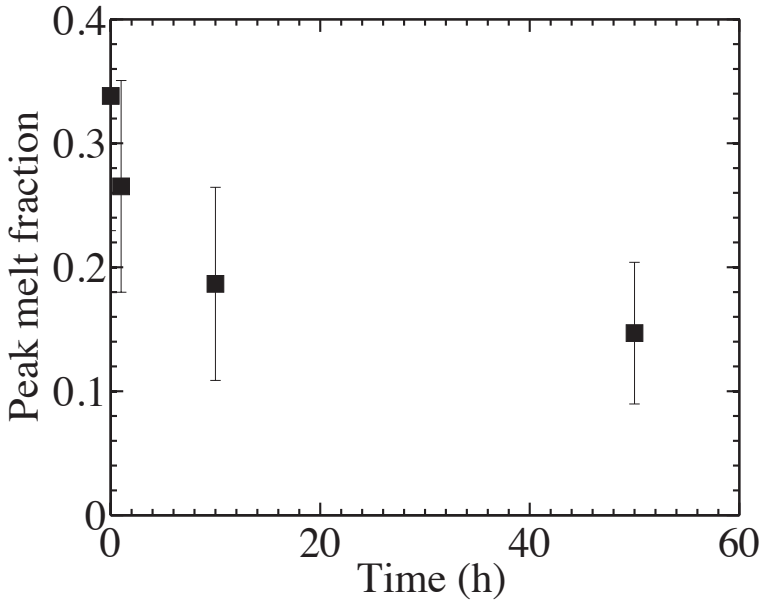

Figure 3.6: Mean value of the peak melt fraction in the bands plotted vs anneal time for the samples in this study. Error bars are one standard deviation

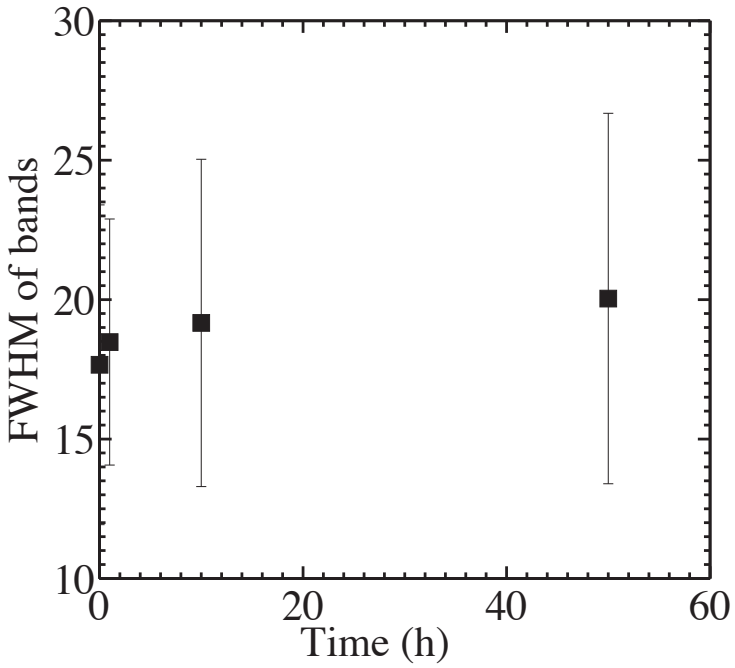

Figure 3.7: Mean band thickness as measured by the full width at half maximum of the bands for different lengths of anneal.

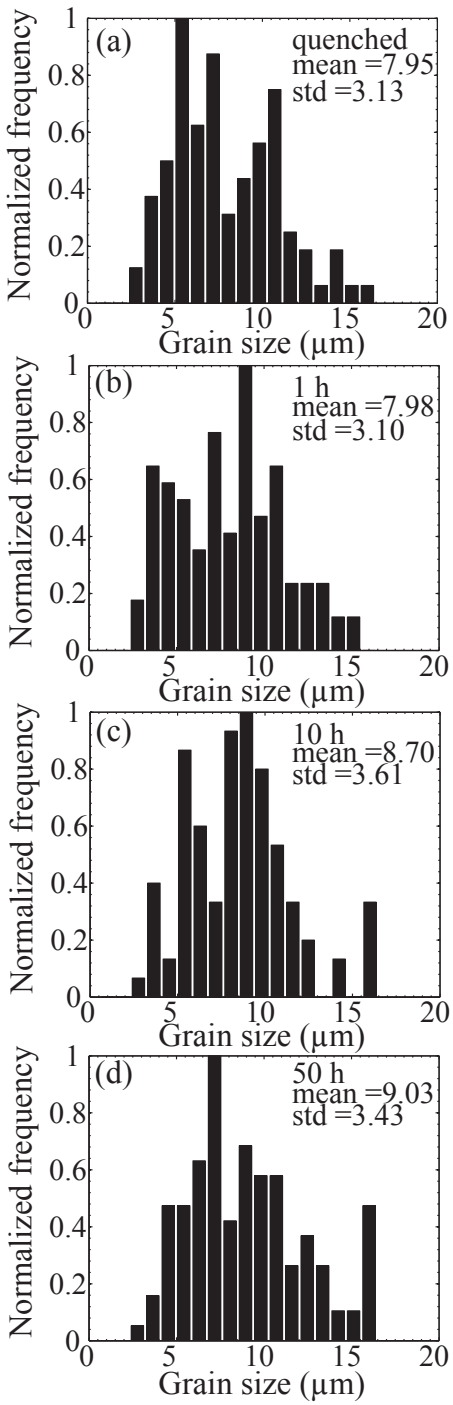

Figure 3.8: Histograms of grain size measured by linear intercept method of (a) quenched sample, (b) 1-h anneal, (c) 10-h anneal, and (d) 50-h anneal. Grain size does not change significantly during the long anneal time, presumably due to the presence of chromite grains as a pinning phase.

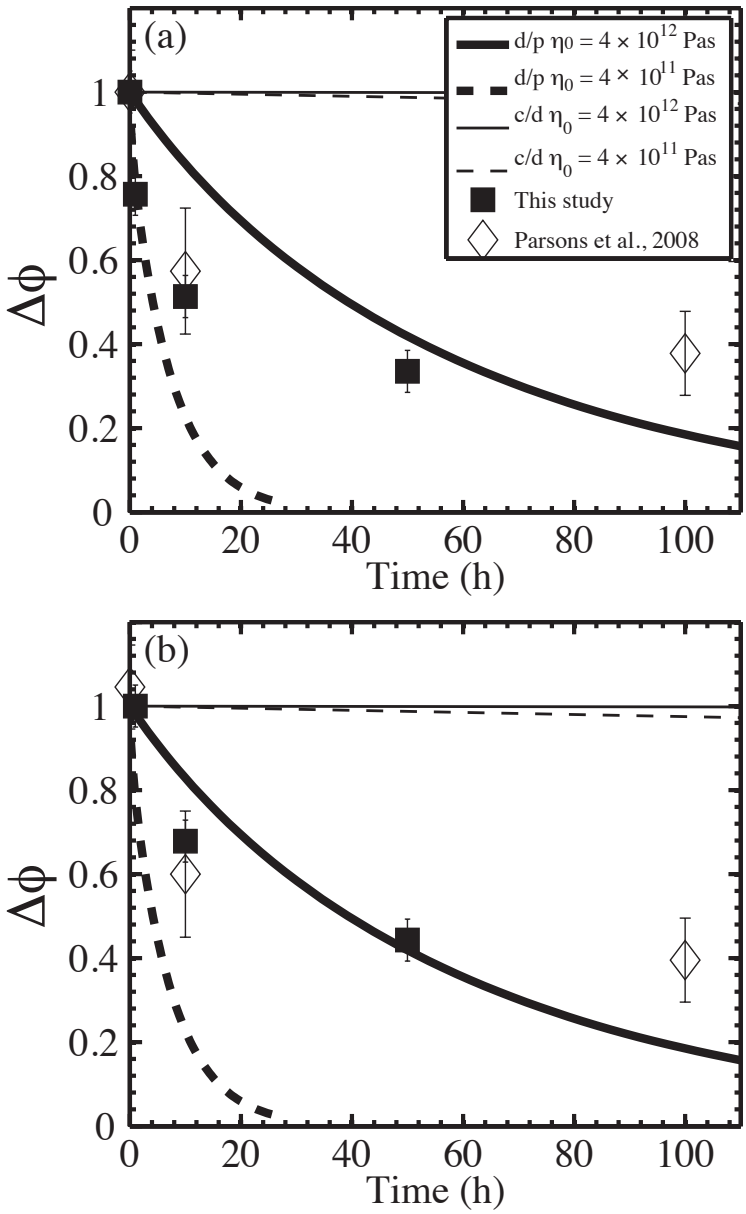

Figure 3.9: (a) Differential melt fraction from this study (solid squares) and from Parsons et al. (2008) (open diamonds) plotted vs anneal time. Model results are plotted for the compaction/decompaction end-member (thin lines) and including dissolution/precipitation (thick lines). For each type of flow model results are plotted for two different reference viscosities. (b) Data from this study normalized to the differential melt fraction in the 1-h anneal compared to model results from (a). The data from Parsons et al. (2008) are normalized to a projected value for $\Delta\phi$ at 1-h using a linear interpolation between the quenched and 10-h values.

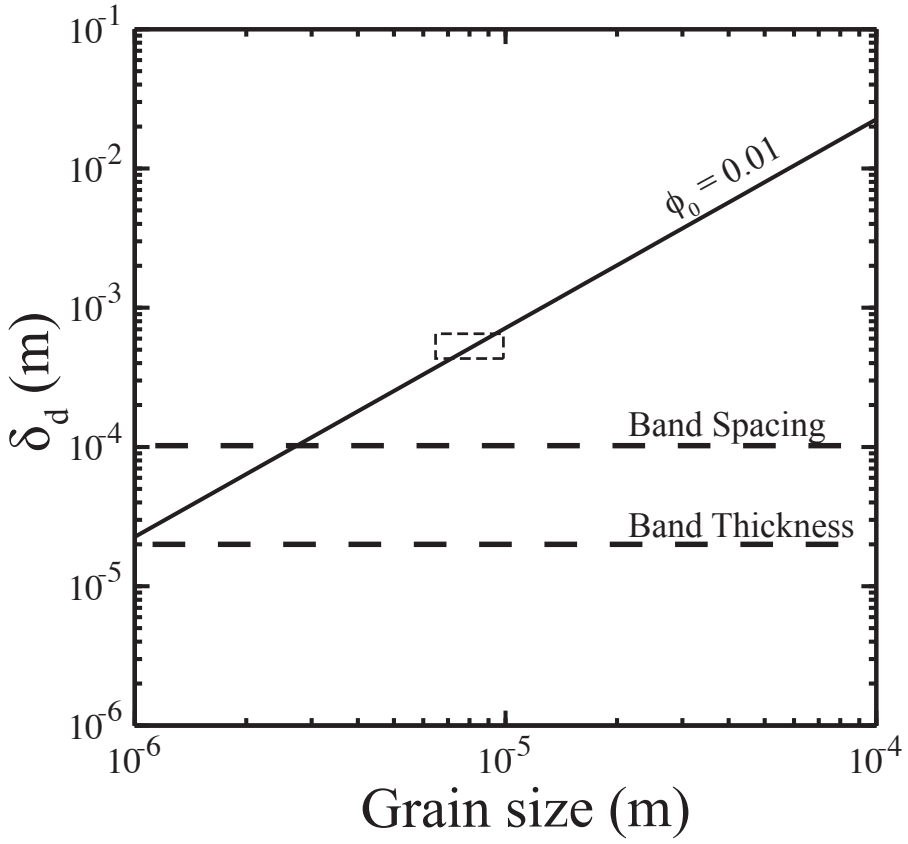

Figure 3.10: Plot of the diffusion length scale (δ_d) vs grain size for $\phi_0 = 0.01$. The horizontal dashed lines indicate the mean band spacing and the mean band thickness (the perturbation length scales) in the sample. The dashed box represent the range in grain size for the sample and the predicted value for δ_d. The band spacing and band thickness are both significantly less than this value of δ_d, suggesting that dissolution/precipitation should be the dominant mechanism of surface tension driven flow.

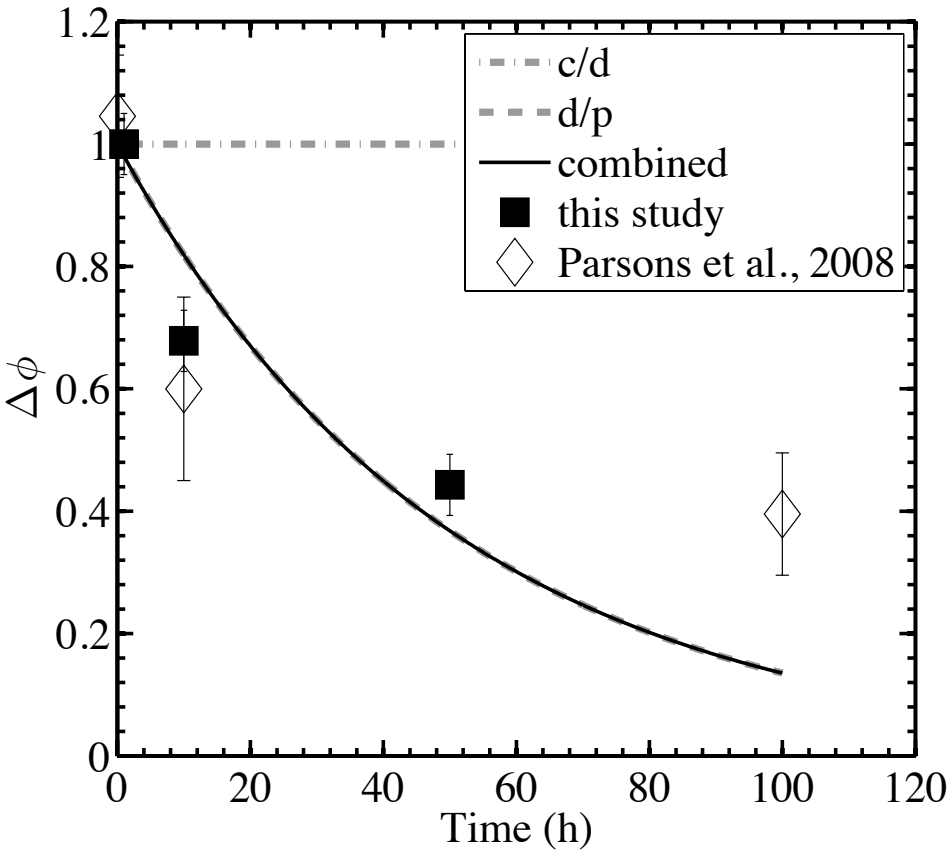

Figure 3.11: Differential melt fraction from this study (normalized to 1 h) and from Parsons et al. (2008) plotted vs time. The dissipation of the perturbation is also plotted for λ corresponding to a perturbation length scale of 4×10^{-4} m, $\phi_0 = 0.01$, and $\eta_0 = 4 \times 10^{12}$ Pa s.

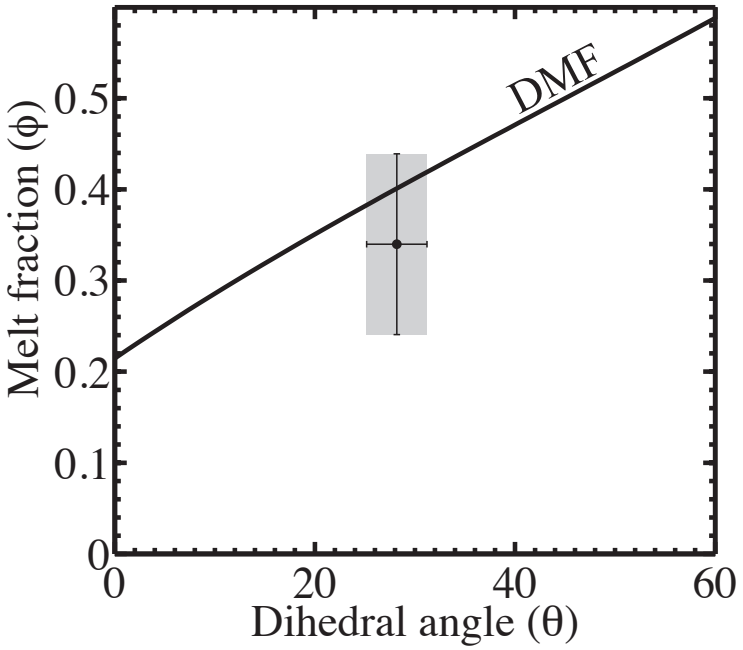

Figure 3.12: Disaggregation melt fraction (DMF) plotted as a function of dihedral angle θ. The height of the gray box represents one standard deviation around the mean of the melt fraction in bands of the quenched sample, and the width of the box represents the range of dihedral angles observed in partially molten samples of olivine by Mei et al. (2002). Note that the bands are mostly below the disaggregation melt fraction (an interconnected network of solid grains exists), but the highest melt fraction bands are above the disaggregation melt fraction.

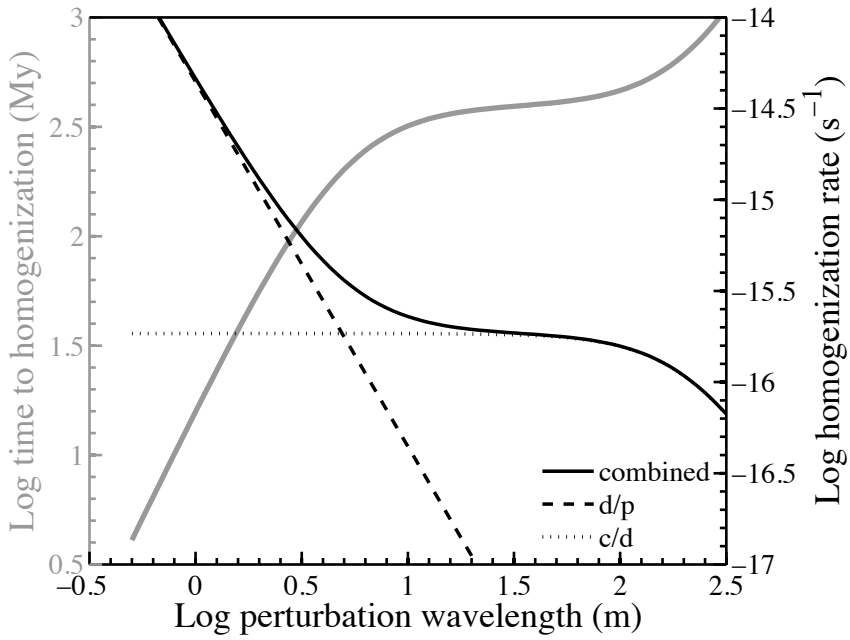

Figure 3.13: Calculations of homogenization of a perturbation in a rock with a 1 mm grain size. The time for dissipation of differential melt fraction to 0.1 (left axis) and the homogenization rate (right axis) for dissolution/precipitation (dashed line), compaction/decompaction (dotted line), and both mechanisms (solid line) as a function of perturbation wavelength.

Chapter 4

Interactions Between Stress-driven and Reaction-driven Melt Segregation

Several different mechanisms of melt segregation and migration may be of importance in extracting melt from Earth's mantle. We present results from experiments investigating the interactions between two mechanisms of melt segregation that have previously been investigated independently of one another, stress-driven and reaction-driven segregation. In the present study, several methods were explored of coupling a melt-rich source in which the basaltic melt is either orthopyroxene-saturated or orthopyroxene-undersaturated with a melt-poor or melt-free olivine + orthopyroxene sink in a geometry that could be deformed in torsion. The basalt in the orthopyroxene-undersaturated melt source will dissolve orthopyroxene and precipitate olivine in the sink leading to reactive infiltration of melt. During reactive infiltration, instabilities can nucleate leading to melt-rich, high-permeability channels penetrating into the sink. With the orthopyroxene-saturated melt source, infiltration still occurs, in this case driven by the reduction of interfacial energy, but reactive infiltration instabilities do not develop. We investigate the interaction between melt-rich channels that form due to reactive instability and melt-rich bands that form as a result of shear deformation. Our experiments

demonstrate (1) that deformation significantly enhances melt migration in all scenarios and (2) that combined reaction and deformation can lead to greater infiltration of melt than does either mechanism alone and enhanced strain localization compared to deformation alone.

4.1 Introduction

The interactions among partial melting, deformation, and melt-rock reactions play an important role in the nature of melt generation and transport in many geological settings including mid-ocean spreading centers, subduction zones, hot spots, and lower crustal migmatites. Based on a variety of geochemical evidence from mid-ocean ridge basalt (MORB), consensus has emerged that, during much of its ascent to the surface, MORB must have traveled through the upper mantle in channels that inhibit the melt from equilibrating with the surrounding peridotite (Johnson et al., 1990; Johnson & Dick, 1992; Spiegelman & Kenyon, 1992; Kelemen et al., 1997). Most notably, erupted MORB sampled from the ocean floor is undersaturated in orthopyroxene (opx) compared to the lherzolite and harzburgite rocks that make up the upper mantle. Geological observations from ophiolites provides additional evidence for channelized flow in the upper mantle. Tabular dunite bodies in ophiolites have been widely interpreted as relict melt channels (e.g., Kelemen & Dick, 1995; Suhr, 1999; Braun & Kelemen, 2002). However, observations of U/Th and Th/Ra isotopic ratios also indicate that a significant amount of melt migration in the mantle must have occurred by diffuse, porous, reactive flow (Lundstrom et al., 1995; Sims et al., 1995; Kelemen et al., 1997). These seemingly conflicting observations lead to the conclusion that an array of melt migration processes are important throughout the upper mantle and lower crust allowing melt to interact with host rock in some places while spending most of its ascent in relative chemical isolation (Kelemen et al., 1997).

Several physical/chemical processes influencing the distribution of melt in a partially molten rock that might provide a mechanistic understanding of these observations have been explored including stress-driven melt segregation, reactive infiltration instabilities, vug waves, hydrofractures, and porosity waves. The focus in this study is on mechanisms of melt migration that apply to the ductile portion of the upper mantle and do

not involve fracture. The reactive infiltration instability is one mechanism capable of inducing melt segregation and channelized flow in the upper mantle (Ortoleva et al., 1987; Aharonov et al., 1995, 1997; Kelemen et al., 1997; Spiegelman et al., 2001). This mechanism is driven by the increasing solubility of pyroxene in basaltic melt with decreasing pressure. Preferential dissolution of opx increases the melt fraction and permeability locally, leading to increased melt flow into these regions, which leads to further dissolution of opx and the propagation of melt-rich fingers upward in the melting column. Reactive infiltration has been demonstrated in experiments in which a pyroxene-undersaturated basaltic melt is coupled with a pyroxene-rich multi-phase rock that acts as a melt sink (Daines & Kohlstedt, 1993, 1994; Morgan & Liang, 2003, 2005). Theoretical studies have also predicted (Stevenson, 1989) and experiments confirmed (Holtzman et al., 2003; Holtzman & Kohlstedt, 2007; Kohlstedt & Holtzman, 2009; King et al., 2010) that an applied shear stress can cause melt to segregate into melt-rich bands. This mechanism of melt segregation leads to an organized network of melt-rich bands oriented $\sim 20^{\circ}$ to the shear plane in an antithetic orientation to the shear direction.

In this study, we present results from experiments designed to investigate the interactions between melt-rock reactions and shear deformation in partially molten harzburgite. Two sets of experiments are discussed. The primary difference between the two sets of experiments is the melt fraction, ϕ, in the source region, so the two sets are referred to as the high-ϕ source series and the low-ϕ source series. In the high-ϕ source series, the melt source has a melt fraction of 0.8-0.9, while in the low-ϕ source series, the melt source has a melt fraction of 0.2. Other less significant differences in sample preparation are discussed in the Methods section. In both series, the microstructures and melt distributions produced by static anneals of source-sink couples are compared with those from torsion deformation experiments of source-sink couples with both opx-saturated and opx-undersaturated melt sources. Also in both series (though more systematically in the low-ϕ series), experiments were performed both with the melt source as an outer ring of the sample and as the core of the sample to explore the situation when reactive segregation and stress-driven segregation propagate in the same and in opposing directions. The results indicate that perturbations in melt fraction and permeability along the interface between source and sink, greater than variations at the grain scale, greatly enhance, and may be necessary for, the development of melt-rich fingers associated with

the reactive infiltration instability. Melt segregation associated with deformation creates such perturbations in melt fraction with a greater amplitude and length scale than variations at the grain scale and leads to significant enhancement in the kinetics of the reaction infiltration instability. In Earth's upper mantle these two mechanisms may work together to promote more efficient extraction of melt than obtained from either mechanism alone.

4.2 Methods

4.2.1 Sample preparation and assembly

Samples were synthesized from fine-grained powders of olivine from San Carlos in Arizona (6 μm), enstatite (opx) from Bamble, Norway (10 μm), chromite from the Semail Ophiolite in Oman (2 μm), and MORB from the Mid-Atlantic Ridge with an olivine tholeite composition (Cooper & Kohlstedt, 1984a). All starting material was prepared by mechanically mixing powders of different combinations of the phases with an agate mortar and pestle. Powders were then cold pressed into a nickel capsule and isostatically hot pressed for at least 2 h at 1200°C and 300 MPa in a gas-medium pressure vessel (Paterson, 1990). At the fine grain size used in these specimens, melt and solid phases rapidly reach chemical and textural equilibrium during hot pressing. The source and sink materials in the two series of experiments are described in the following sections. The nearly 100% melt source coupled with a melt-poor sink in the high-ϕ source series is similar to the configuration used in source-sink couples in static anneal experiments such as Daines & Kohlstedt (1994) and Morgan & Liang (2003, 2005). The high melt fraction in the source ensures a large reservoir of melt. However, the lack of an interconnected solid framework of grains across the source-sink interface is a cause for concern when comparing the results of deformation experiments with prior studies of the distribution of melt in deforming partially molten rocks (e.g., Holtzman et al., 2003; Holtzman & Kohlstedt, 2007; King et al., 2010). The low-ϕ source series resolves this concern while maintaining a sufficiently large reservoir of opx-undersaturated melt for the durations of the experiments.

High-ϕ source series

In this series, a nearly 100% melt source was coupled with a sink containing 5% melt. The sink material used in this series was olivine + opx + chromite + MORB in a 8:8:3:1 volume ratio. This sink material was designed to be similar to the sample material used in prior studies of stress-driven melt segregation (e.g., Holtzman & Kohlstedt, 2007; King et al., 2010) with the addition of opx. The opx-undersaturated melt source material was composed of MORB + olivine in a 9:1 volume ratio, and the opx-saturated melt source was MORB + olivine + opx in an 8:1:1 volume ratio. In the starting sink material used for samples PT0406 and PT0410 some clumps of chromite remained and some pockets of olivine + opx remained chromite-free, but the majority of chromite was well distributed.

After hot pressing separate rods of the source and sink materials, $\sim$ 4 mm long cylinders were cut from each. Cores were taken from each cylinder with an inner diameter of the outer ring and outer diameter in the inner core of 4.25 mm, as depicted in Figure 4.1. Diamond files were used to smooth the nesting surfaces for a snug fit. The final height varied from one sample to the next because it was necessary to remove some material after the couple was assembled in order to achieve flat, uniform surfaces on the top and bottom of the samples. In the high-ϕ source series, all but one of the source-sink samples were prepared with the melt source as the core. One sample was prepared with the melt source as the outer ring. Additionally, one cylinder of sink material was not cored so that it could be deformed without a melt source to investigate only the mechanical effects on melt distribution. Pistons cored from natural dunite placed above and below the samples provide frictional gripping at the interface.

Low-ϕ source series

In this series, a source with a melt fraction of 0.2 was coupled with a nominally melt-free sink. The sink material used in this series was olivine + opx in a 1:1 volume ratio. The purpose of the chromite in the sink material in the high-ϕ source series was to reduce the permeability, which facilitates stress-driven melt segregation. Chromite was left out of the sink material in the low-ϕ source series due to concerns that the reduced permeability would inhibit reactive infiltration. In this series, we studied more

systematically the differences resulting from having the melt source as either the outer ring or the core of the sample. The different ways in which mechanical and chemical processes might interact in the two different geometries are summarized in figure 4.2. The opx-undersaturated melt source was composed of olivine + MORB in an 8:2 volume ratio, and the opx-saturated melt source was olivine + opx + MORB in a 4:4:2 volume ratio.

After hot pressing separate rods of the source and sink material, $\sim$ 4 mm long cylinders were cut from each, similar to the high-ϕ series. Samples were prepared with the melt source both as the core of the sample and as the outer ring in a more systematic way than in the high-ϕ series. Cores were taken out of each cylinder with the inner diameter of the outer ring and outer diameter of the inner core of 6.2 mm, as depicted in Figure 4.1. Diamond files were used to smooth the nesting surfaces for a snug fit. Pistons of porous alumina (0.8 Al_2O_3, 0.2 SiO_2, 0.44 g/cc) with a porosity of $\sim$ 0.20 were placed adjacent to the samples in order to achieve more reliable sample gripping than with the use of dunite spacers as used in the high-ϕ series.

4.2.2 Procedure

The samples were deformed in a gas-medium apparatus equipped with a torsion actuator (Paterson, 1990; Paterson & Olgaard, 2000). The experiments were performed at a constant rate of angular displacement as measured by a rotational variable displacement transducer (RVDT) outside the pressure vessel. Torque was measured by a torque cell housed inside the pressure vessel. Temperature was monitored within 3 mm of the sample using a Pt-Pt/Rh thermocouple. Furnace calibrations confirm variation of $< 1°C$ along the length of the sample. Methods for determining shear stress and shear strain rate from torque and angular displacement as a function of time are described by Paterson & Olgaard (2000).

The samples were deformed at a constant twist rate corresponding to strain rates at the outer radius of the sample given in Table 4.1. Two samples from the high-ϕ series with opx-undersaturated melt cores were deformed to shear strains of $\gamma_{max} = 1.0$ and 2.3 ($\gamma_{max} = \gamma(R)$, where R is the radius of the sample). One sample with an opx-saturated melt core was deformed to a shear strain of $\gamma_{max} = 1.1$. Because of frequent problems involving slipping at the sample dunite boundaries, all of the samples in the

high-ϕ series spent some period of time at high pressure and temperature under static conditions during unsuccessful attempts at deformation. The time of annealing (pre-deformation) and the time during which deformation occurred are noted in Table 4.1. This problem was resolved in the low-ϕ series by using porous alumina pistons adjacent to the sample. The porous alumina prevented the build up of a melt layer along the sample-piston interface, leading to reliable coupling at that interface. By acting as a melt sink, the porous alumina also drew melt out of the source and reduced the overall melt fraction of the sample, but this effect should be the same in samples with opx-saturated and opx-undersaturated sources. In the low-ϕ source series, one sample was statically annealed for 19 h with an opx-undersaturated melt source as the outer ring. Samples with both an opx-saturated and opx-undersaturated melt source as the outer ring were deformed to a shear strain of $\gamma_{max} \approx 2.5$. After deformation samples were polished on the axial section, a longitudinal tangential section, and a transverse section (perpendicular to the axial and tangential sections) using diamond lapping film to 0.5 μm followed by 10 min of polishing with colloidal silica (0.03 μm). The different sections of the sample are depicted in Figure 4.3. To make the melt more visible, samples were then etched with a 50:50 mix of HF and HCl diluted 20:1 with water for 20-30 s, which preferentially etches the quenched melt phase as well as grain and phase boundaries.

4.3 Results

4.3.1 High-ϕ source series

Static anneal with opx-undersaturated source core

The sample statically annealed for 6 h with an opx-undersaturated, high-ϕ source as a core exhibited evidence of uniform reactive infiltration with a few locations where melt had propagated into the sink material significantly farther than the uniform infiltration front. A mosaic image of reflected light micrographs in Figure 4.4a displays the entire axial section. The position of the interface between the high melt fraction core and the low melt fraction sink can be traced by the boundary in the occurrence of chromite. The width of the melt-rich core has not changed significantly, indicating only a small amount of melt infiltration and corresponding limited migration of the source-sink interface.

Along the entire interface, a reactive boundary layer about 45-μm wide exists in which all of the opx in the sink has dissolved into the melt leaving behind only olivine + MORB. This reactive boundary layer (RBL) is visible in the images of Figure 4.5. The RBL is too small to be visible in Figure 4.4, and it is difficult to observe in reflected light images. Along the source-sink interface visible in Figure 4.5, a region of olivine + opx (absent in chromite) intersects the interface. This region is a result of incomplete mixing of the powders during sample preparation. (Other such regions are present within the sink material away from the interface.) Within the olivine + opx region, a finger of high melt fraction is surrounded by a rim of 100% olivine in which all of the opx has dissolved, visible in the Mg x-ray map in Figure 4.5b. Nucleating from this region of 100% olivine within the olivine + opx regions is a finger of melt that extends several hundred microns into the sink, visible in Figure 4.6. Two other such fingers are visible on the axial section, both associated with a chromite-free regions that intersects with the source-sink interface.

Deformation of sink material without a melt core

A sample of the material used as the sink material in all other high-ϕ source experiments was deformed without a melt core to observe the effects of only deformation on melt distribution. This sample was deformed to a shear strain of $\gamma_{max} = 1.2$, which is just above the strain at which stress driven melt segregation becomes visible in similar samples without opx (King et al., 2010). On the tangential section, displayed in Figure 4.7, alignment of melt $\sim 20^{\circ}$ to the shear plane can be clearly observed with minor segregation at length scales greater than the grain scale. On the radial section, a few high-melt fraction bands can be observed extending a few hundred microns toward the center radius of the sample. Consistent with prior observations that melt-rich bands form at a shear strain of $\gamma \approx 1$, the bands extend to approximately the radius at which $\gamma = 1$. Overall, the observed pattern of melt distribution is consistent with the early stages of stress-driven melt-rich band formation.

Deformation with opx-saturated source core

A sample deformed with an opx-saturated melt source acts as a control so that we can determine which features are deformation-related and which features involve melt-rock

reaction. Since the melt source is saturated in opx, melt infiltration should not be driven by dissolution of opx. The axial section of this sample is shown in Figure 4.4b. The most striking feature in this sample is that much more melt has migrated from source to sink than in the statically annealed sample. The melt fraction is significantly greater than the initial value of $\phi = 0.05$ in the sink material, and the diameter of the melt-rich core has been reduced by approximately a factor of two during deformation. These observations indicate that a large amount of melt from the core has infiltrated into the sink, all the way to the outer radius of the sample. Melt infiltration does not appear to be uniform, with greater infiltration near the center of the height of the sample.

Deformation with opx-undersaturated source core

Two samples deformed with opx-undersaturated melt cores were deformed to different total shear strains to explore the evolution of melt distribution with increasing strain. The axial section of the low-strain sample is pictured in Figure 4.4c, and the high-strain sample is pictured in Figure 4.4d. Because of frequent slip at the sample-dunite interface, the samples that were successfully deformed with a melt core spent several hours statically annealing at elevated temperature before being deformed. The two deformed samples spend a total of $\sim$ 8 h at 1200°C (Table 4.1), compared to 6 h for the statically annealed sample. This similarity in the length of time at high temperature allows us to look at the effects of deformation independent of anneal time.

Parallel to the source-sink interface, planar melt-rich regions appear to be propagating out of the sink as waves. The waves are clearly visible in a backscattered electron image and x-ray map of Mg of the source-sink interface of the high strain sample (PT0406) displayed in Figure 4.8. In the low strain sample, the waves of high melt fraction appear to propagate faster near the center of the height of the sample and form chevron shapes moving into the sink material. The waves are narrower and more melt-rich in the high strain sample (PT0406) than in the low strain sample (PT0453). On the axial section of the low strain sample (Figure 4.4c), a region of high melt fraction several hundred microns wide is visible parallel to the source-sink interface with low melt fraction material on either side. On the axial section of the high strain sample (Figure 4.4d and 4.8), the high melt fraction region parallel to the interface is $\sim$10 μm wide. Such discontinuous melt infiltration is also visible on the face perpendicular to

the axial section (i.e., the transverse section) as displayed in Figure 4.9. On the left side of the melt source core is an instance of discontinuous melt infiltration. These features could indicate either waves of melt nucleating from the source or material from the sink "rafting" into the high melt fraction source. As will be discussed more later, the discontinuous melt infiltration, particularly the "rafting" is not interpreted to be related to melt-rock reaction.

Both samples deformed with an opx-undersaturated melt source display evidence of strain localization that was not observed in the opx-saturated melt source sample. The opx-undersaturated source samples both experienced off-axis shearing, as evidenced by the offsets and deflections along the vertical edges of the axial sections in Figure 4.4c and d. High melt fraction bands indicated by arrows in Figure 4.4d extend from the sample-jacket interface toward the center of the sample at an angle to the sample-dunite interfaces. In the high strain sample, the sample-jacket interface is distinctly offset on one side of the axial section. On the other side of the axial section, the sample-jacket interface is deflected in two locations. The low strain sample has one deflection in the sample-jacket interface.

Deformation with opx-undersaturated melt source ring

One experiment was performed with the inverse setup from the rest of the samples, that is, with the melt source at the outside of the torsion sample. One half of the axial section of this sample is shown in Figure 4.10. Similar to the samples described above, the radial section of this sample records waves of melt propagating inward from the melt source into the sink. The waves form a similar chevron shape with melt propagating faster near the center of the sample than near the interfaces with the dunite pistons.

Synthesis and discussion of observations from high-ϕ source series

The high-ϕ, opx-undersaturated source anneal displays some evidence indicating the initiation of reactive infiltration instabilities. Most of the interface visible on the polished section displays uniform infiltration and the formation of a reactive boundary layer absent in opx. However, due to minor inhomogeneities in mixing, a few islands of olivine + opx material absent in chromite are in contact with the source region. Because the fine-grained chromite plugs some triple junction pathways, it reduces the permeability

of the material. Therefore, these islands of olivine + opx (absent of chromite) have a higher permeability, which facilitates more rapid melt infiltration, thus setting up the reactive infiltration instability allowing a melt finger to nucleate and propagate well into the homogeneously mixed sink material as exemplified by the finger in Figures 4.5 and 4.6. This observation was the motivation for leaving chromite out of the sink material in the low-ϕ series.

It is clear from the images of axial sections in Figure 4.4 that much more melt has infiltrated into the sink from the source in samples that were deformed. Figure 4.11 is a plot of the melt fraction as a function of distance from the outer radius for samples with a melt source as a core and for the sample prepared from the sink material without a melt source. The data were collected from a series of images from the axial section; a threshold was applied creating a binary image representing the melt distribution. The area fraction of melt was calculated for a region 100-μm wide (about the width of the symbols on the plot) and 500-μm high. Indeed, the melt fraction profile in the annealed sample drops from $\phi = 0.9$ in the source to the background melt fraction initially present in the sink within < 500 μm, while all of the deformed samples have a melt fraction elevated above the amount initially present in the sink all the way to the outer radius. The melt fraction at the outer radius is particularly high in the sample with an opx-undersaturated source deformed to high strain because part of the area over which the melt fraction was averaged was within a melt-rich band. The variation in the radius at which melt fraction increases dramatically among the deformed samples is primarily a result of imprecision in the centering of the source core and in making the axial cut after deformation. We interpret the plot to indicate a similar magnitude of melt infiltration among all deformed samples, which is much greater than the statically annealed sample.

Figure 4.12 compares representative backscattered electron images of the source-sink boundary within samples in the high-ϕ source series. The sample with an opx-saturated melt source (Figure 4.12a) displays significant melt infiltration past the source-sink interface marked by the presence of chromite, but opx is uniformly present within the sink material. In the samples with an opx-undersaturated melt source, the thickness of the reactive boundary layer increases in width and in variability with increasing strain. The statically annealed sample has a relatively uniform reactive boundary layer 45 μm

in thickness, while the low strain sample has a reactive boundary layer up to 75 μm in thickness, and the high strain sample has a boundary layer up to 130 μm in thickness. The increasing irregularity of the width of the reactive boundary layer is evidence for spatial heterogeneity in the extent of the dissolution of opx.

The dramatic off-axis shearing observed in the deformed samples with an opx-undersaturated source is unexpected in the context of observations from prior experiments investigating stress-driven segregation in torsion (King et al., 2010). The stress-induced melt-rich bands in the high-ϕ source series, such as those visible in Figure 4.4d, are not parallel to the top and bottom of the sample on the axial section as they propagate inward toward the center of the sample. Instead they form an angle of $\sim 20^{\circ}$ to the sample-piston interface. The occurrence of off-axis shearing in both of the samples deformed with an opx-undersaturated melt source, while none is observed in the sample deformed with an opx-saturated melt source, suggests that melt-rock reaction is enhancing melt segregation and strain localization.

Based on the evolution of microstructure recorded in the two opx-undersaturated samples deformed to different strains, we propose the following sequence of events illustrated in a series of sketches in Figure 4.13. (1) Melt-rich waves propagate from the melt source. The waves propagate slower at the dunite interface because the dunite acts as a melt sink, leading to their chevron shape. (2) Stress-driven segregation initiates at the outside edge of the sample at $\gamma = 1$, and bands propagate inward. (3) At some point, a wave intersects a stress-induced melt-rich band resulting in localized deformation on a plane oblique to the horizontal axis of the sample and off-axis shearing due to the chevron shape of the 3D porosity waves. Because of the very high melt fraction in these bands ($> 30\%$), the viscosity is dramatically reduced (Scott & Kohlstedt, 2006).

In summary, there is evidence for instances of a reactive infiltration instability in the statically annealed sample, but only nucleating from perturbations in permeability due to incomplete phase mixing. Fingers of melt nucleating from the source are not observed in the deformed samples, but irregularities in the width of the reactive boundary layer indicate spatial heterogeneity in the extent of opx dissolution. Deformation significantly enhances melt infiltration, and melt infiltration occurs discontinuously with waves propagating into the sink parallel to the source-sink interface. Localization is observed on melt-rich shear bands propagating in from the outer radius of the sample. Localization

and off-axis shearing are more significant and occur at a lower strain in samples with an opx-undersaturated melt-source than with an opx-saturated melt source.

4.3.2 Low-ϕ source series

Static anneal with opx-undersaturated source ring

Static annealing of the low-ϕ source coupled with a melt-free sink did not result in any non-uniform melt infiltration features. One sample with an opx-undersaturated melt source as the outer ring was annealed for 10 h at 1200°C. The entire axial section is pictured in Figure 4.14, and portion of the radial section is shown in Figure 4.15e. After the anneal, the source-sink interface remained sharp in the 2-D cross section of the axial section with only minor irregularities and no significant gradient in melt fraction at length scales greater than the grain size, as shown in the reflected light micrograph of Figure 4.16a. Half of the sample was then rejacketed and annealed for an additional 9 h at 1250°C. The source-sink interface of the sample annealed for longer, pictured in Figure 4.16b, is slightly more irregular, but no significant fingers of melt infiltration were observed.

Deformation with opx-saturated source ring

The sample deformed with an opx-saturated melt source as an outer ring is expected to record melt-redistribution associated with deformation, and not reactive flow. The section pictured in Figures 4.17a and 4.15a displays clear melt segregation features consistent with those from stress-driven melt segregation. The bands appear on the axial section as straight lines propagating inward from the outer radius of the sample. Uniformly spaced melt-rich bands are also visible on the tangential section at a $\sim 20^{\circ}$ angle to the overall shear plane in an antithetic orientation, as pictured in Figure 4.19. Some bands, especially near the vertical center of the sample, propagate well into the initially melt-free sink in the core of the sample. We interpret the variation between the center of the sample and the top and bottom to be a result of the use of porous alumina spacers, which act as melt sinks but are necessary for effective gripping of the sample. The bands penetrate into the sample to the radius at which $\gamma = 1$, which is a robust observation associated with stress-driven melt segregation in torsion samples

(King et al., 2010). No melt is observed in the center of the sample beyond the stress-driven melt segregation band front.

The transverse section of the sample deformed with and opx-saturated melt source ring, displayed in Figures 4.20a and 4.18a, reveals similar features as the axial section with melt-rich pathways penetrating well into the sink material, but consistently stopping at the radius at which $\gamma = 1$. Most of the melt-rich pathways are continuous bands of high melt fraction within the source that penetrate into the sink. However, some regions of high melt fraction in the sink appear not to be connected to the source in the plane of this image, though we expect them to be three dimensionally connected.

Deformation with opx-undersaturated source ring

The sample deformed with an opx-undersaturated melt source as an outer ring not only contains similar evidence for stress-driven melt segregation, but also exhibits distinct features that may be attributed to melt-rock reactions. Bands of a geometry consistent with stress-driven segregation are visible on the tangential section and near the outer radius of the axial section, though they are less distinct than in the opx-saturated melt source case. Many of the bands propagated well past the source-sink interface and are more distinct within the sink material. Most of the bands terminate at the radius at which $\gamma = 1$. However, unlike in the opx-saturated melt source case, a significant amount of melt penetrated farther toward the center of the sample as indicated by arrows in Figure 4.17b. Some of these regions are connected to bands penetrating from the outside, but some appear as 'islands' not clearly connected on this 2-D face to deformation associated bands closer to the outer radius.

The transverse section of the sample deformed with an opx-undersaturated melt source ring is displayed in Figures 4.20b and 4.18b. While fewer melt-rich pathways penetrate into the sink from the source than in the opx-saturated melt-source sample, the pathways in this sample are wider in this view of the transverse section, and they extend farther into the sample, penetrating into the sink past the radius at which $\gamma = 1$. The two major pathways observed to penetrate far into the sink in this image are continuous from the source-sink interface well into the sink. However, on the axial face in Figure 4.17b, the high melt fraction regions in the sink near the center of the sample appear to be disconnected from the source. This geometry suggests that these

melt islands are actually connected out of the plane of the polished axial section and that this melt was transported from the source through a tube-shaped high-permeability pathway rather than a planar high-permeability pathway.

Evidence for irregularities in mineral abundance occur along the source-sink interface. An x-ray map of Mg from the region indicated in Figure 4.17b is displayed in Figure 4.21. The lightest gray represents olivine, the darker gray opx and the darkest shade melt. The boundary between the region of 100% olivine and the opx-bearing region, which was originally planar, is traced with a dashed line. This boundary now contains protrusions ∼100-μm long of 100% olivine into the sink material. The melt-rich band that extends several hundred microns into the sink appears to originate at one of these protrusions. However, toward the bottom of this image, a "finger" of olivine is present with only minor amounts of melt present beyond it.

Deformation with opx-saturated source core

One sample was deformed with a cylinder of opx-saturated source material as the core of the sample. In this sample, pictured in Figure 4.22a and 4.15c, melt-rich bands parallel to the top and bottom of the sample are present on the axial section within the source material, and they terminate at the radius at which $\gamma = 1$. The melt-rich bands have also propagated outward $\sim 100 - \mu$m into the sink material. Because no melt was present initially in the sink material and the bands only occur in conjunction with a melt-rich band in the source, this propagation presumably did not occur until the $\gamma = 1$ front passed the source-sink interface.

The transverse section displayed in Figures 4.23a and 4.18d provides another perspective on the distribution of melt across the source-sink interface. Similar to the axial section, only minor melt-rich pathways are visible penetrating into the sink material, and they are associated with bands of stress-driven segregation within the source material. One such feature with a melt band visible extending into the source to the radius at which $\gamma = 1$ and with melt infiltration into the sink associated with the band is marked with an arrow.

Maps of phase distribution can be obtained from Mg x-ray maps displayed in Figure 4.24b. In the opx-saturated source sample, no regions are absent in pyroxene and phase distribution appears uniform both within the source material and the sink material.

However, the Mg concentration within pyroxene appears to be slightly greater (darker grayscale) in the source material than in the sink.

Deformation with opx-undersaturated source core

The sample deformed with a core of opx-undersaturated source material contains features distinct from the opx-saturated source sample. The distance the bands extend from the source into the sink is significantly greater in the sample with an opx-undersaturated source, as depicted in the comparison of the source-sink boundaries in Figure 4.24a and c. Also, the sample with an opx-undersaturated source exhibits some off-axis shearing, visible in Figure 4.22b, suggesting that the enhanced melt migration into the sink nucleating from deformation-induced bands creates melt-rich shear zones. The observation that off-axis shearing occurs in samples with an opx-undersaturated core, but not with an opx-saturated core, is consistent with the observation in the high-ϕ source series.

In contrast with the sample with an opx-saturated melt source core sample, the transverse section of the sample with an opx-undersaturated source, displayed in Figures 4.22b and 4.15d, reveals many instances of melt-rich pathways penetrating into the sink material. In some cases, these pathways extend >500 μm into the sink. Their occurrence is not uniformly distributed around the sample, with many pathways clumped together in some places and a significant extent of finger-free source-sink interface elsewhere.

A Mg x-ray map of the source-sink interface is displayed in Figure 4.24d. Two relatively small ($\sim$ 150 μm) melt-rich bands extending from the source initiate from slight irregularities in phase distribution. One band near the middle of the image seems to be associated with a slight step in the source-sink boundary, which may indicate localized shear deformation within this band. The band at the top of the x-ray map is associated with a significant ($\sim$ 100 μm) long region of 100% olivine extending into the sink region. This melt-infiltration feature is clearly the largest in Figure 4.24c and deviates significantly from the flat, planar bands expected from stress-driven segregation.

Synthesis and discussion of observations from low-ϕ source series

Results from the low-ϕ source series support the interpretation that instabilities require perturbations greater than produced by the random variability of phase distribution in the sink material or from melt fraction variations at the grain scale. The results

also reveal that deformation is an effective way to create these perturbations. Melt-rich bands that result from deformation create zones of high melt fraction within the source that lead to perturbations in melt fraction along the source-sink interface. The greater difference in melt fraction between the source and sink at these melt-rich bands leads to a greater driving force for surface tension driven flow than along the rest of the interface, causing the melt to flow into the melt-free sink. In the sample with an opx-saturated source as the outer ring (pictured in Figures 4.17a,4.15a, and 4.18a), the bands propagate from the outer edge inward to a shear strain of $\gamma = 1$, consistent with the observation from King et al. (2010). In the sample with an opx-undersaturated source as the outer ring (pictured in Figure 4.17b,4.15b, and 4.18b), many bands terminate at the same radius, that is, $\gamma = 1$; however, the bands that penetrate farther into the sample suggest that reactive instabilities initiated from the perturbations in melt fraction (permeability) induced by the stress-driven melt segregation. Or, in other words, reactive infiltration enhanced the propagation of stress-driven segregation bands into the sink material. The fact that, in the sample deformed with an opx-undersaturated source as a ring, some of the melt-rich regions closer to the center of the sample than the $\gamma = 1$ radius are "islands" that appear to be disconnected from the source in this 2-D cross section supports the interpretation of them as reaction-driven instabilities. The reactive instability should form fingers of melt penetrating into the sink, rather than the planar bands that result from stress-driven segregation. Indeed, the transverse section (Figure 4.20b) reveals that, within the plane parallel to the top and bottom of the sample, the melt pathways are connected to the sink. These differences among the samples are summarized schematically in Figures 4.25 and 4.26.

Observations, particularly from the transverse sections, of the two deformation geometries differ in the extent of melt infiltration in samples with both opx-saturated and opx-undersaturated melt sources. Much greater infiltration is observed in the samples with the melt source as the outer ring. This difference can be explained in terms of the difference in the time of the experiment at which the mechanical instability initiates. In samples with the source as the outer ring, stress-driven segregation begins to occur within the source as soon as the outer radius reaches a shear strain of $\gamma = 1$. These bands then propagate inward as strain increases; they either propagate into the sink mechanically as low-viscosity, low-pressure regions that draw melt out of the source

(opx-saturated source, Figure 4.20a), or they nucleate fingers of reactive infiltration (opx-undersaturated source, Figure 4.20b). In samples with the melt source as the core of the sample, because the outer ring is initially melt-free, stress-driven melt segregation does not initiate until the source-sink interface reaches a shear strain of $\gamma = 1$. Therefore, less time has elapsed (and less strain has accumulated) between the formation of perturbations in melt fraction and the end of the experiment, allowing for less growth of the melt pathways either mechanically or through reactive instabilities. However, within each deformation geometry, samples deformed with an opx-undersaturated melt source display greater infiltration of melt than do samples with an opx-saturated melt source.

Figure 4.26 depicts the results of combined deformation and melt infiltration on the same section as depicted in the sketches demonstrating the motivation for the two geometries (Figure 4.2). In addition to the amount of time between band formation and the termination of the experiment, the propagation direction of the bands could explain the differences in observed melt distribution in the two geometries. Solid arrows represent melt segregation within the melt source and the direction in which melt segregation propagates. Open arrows represent the driving forces for melt infiltration, other than deformation. Dashed arrows represent the observed extent of infiltration into the sink emanating from bands within the source resulting from deformation. The results from the samples with opx-saturated melt source (Figure 4.26 a and c) demonstrate that surface tension alone is not a strong driving force for melt infiltration. Very little infiltration occurred in the sample with a melt source as a core. However, significant infiltration did occur in the sample with a melt source as a ring, suggesting that stress-driven melt-rich bands can continue to propagate into the sink, drawing melt from the source. The opx-undersaturated source counterparts of the two geometries, depicted in Figure 4.26 b and d, demonstrate the enhancing effects of melt-rock reaction on melt infiltration.

In addition to observations of the melt distribution at the time the sample was quenched, observations of the distribution of olivine and opx can reveal the history of melt infiltration. X-ray maps showing the phase distribution demonstrate that many melt-infiltration features in the opx-undersaturated melt source samples initiate at an irregularity along the source-sink interface where a region of 100% olivine

protrudes into the sink material. This observation is evidence for an instability in dissolution/precipitation reactions. However, melt infiltration goes far beyond the region of 100% olivine, some melt bands do not initiate at such a feature (Figure 4.24d), and some fingers of 100% olivine are present without an associated finger (Figure 4.21). These observations all indicate interactions between deformation and reaction. In order for melt-rich bands associated with deformation to maintain a constant geometry relative to the shear plane, they must continually reorganize with respect to the deforming matrix. The fingers of olivine not associated with a melt band represent regions where a melt band existed at a lower strain before reorganization of the band to maintain a constant angle to the shear plane.

Mechanical data for the samples in the low-ϕ source series, plotted in Figure 4.27, can provide insight into the evolution of the strength of the sample as the melt distribution evolves. In Figure 4.27, the shear stress is plotted as a function of shear strain for the outer radius of the sample. Shear stress is calculated from the measured torque using the relationship for shear stress as a function of radius τ_r (Paterson & Olgaard, 2000)

$$\tau_{\mathrm{r}} = M \frac{4(3 + 1/n)}{\pi D^3} \left(\frac{2r}{D} \right)^{1/n}, \tag{4.1}$$

where M is the measured torque, D is the diameter of the sample, n is the stress exponent, and r is the radius for which shear stress is calculated ($D/2$ in this case). This method of calculating shear stress as a function of radius assumes a constant stress exponent and constant phase distribution throughout the sample, which is not the case in these samples. However, since the same stress exponent ($n = 3.5$) was used for all samples, it is useful to compare the different samples in calculated shear stress rather than measured torque because it takes into account the slight variations in sample diameter from one sample to the next.

To compare the strength of samples at the same shear strain, the shear stress is noted on each plot for $\gamma = 2$. For both opx-undersaturated and opx-saturated sources, samples with the source as a ring are weaker than their counterparts with the source as a core (compare Figure 4.27a vs c, and b vs d) . Because the volume of the sample increases at a given radius toward the outside of the sample, the outer portion of the sample has a greater influence on the strength of the sample. Since the samples with

the source as a ring have the high melt fraction near the outer radius of the sample, this geometry is expected to be weaker. Within each geometry the sample with an opx-undersaturated melt source is weaker than the sample with an opx-saturated melt source (compare Figure 4.27a vs b, and c vs d). This observation suggests one of two things: either (1) material composed of olivine + opx + 20% MORB is stronger than material composed of olivine + 20% MORB or (2) the effects of melt-rock reaction in samples with an opx-undersaturated source leads to greater shear localization than occurs in samples with an opx-saturated melt source. Axial compression experiments by Zimmerman & Kohlstedt (2004) demonstrate that, while nominally melt-free olivine is stronger than nominally melt-free lherzolite (olivine + opx + cpx), olivine + 10% MORB is weaker than lherzolite + 10% MORB. These observations support the first possibility as the source of the strength difference. However, in support of the second possibility are the observations of off-axis shearing and offsets in the source-sink interface visible on the axial section that indicate greater shear localization in samples with an opx-undersaturated melt source. Future experiments exploring the the evolution of melt distribution at lower strains could determine if melt bands form at $\gamma < 1$ in samples with an opx-undersaturated source. It could also be possible to include a passive strain marker in the sample assembly to quantify the amount of localization in different samples.

In summary, the results from the low-ϕ source series lead to the interpretation that the coupling of deformation and melt-rock reactions leads to greater infiltation of melt than does either mechanism acting alone. Stress-driven melt segregation provides the perturbations in melt fraction necessary to initiate reactive instabilities, and deformation in the presence of an opx-undersaturated melt leads to greater infiltration of melt into the sink than occurs in a static anneal or due to deformation alone.

4.4 Discussion

From the high-ϕ source series, we learn (i) that deformation significantly enhances melt infiltration in samples both with an opx-saturated and with an opx-undersaturated melt source and (ii) that melt infiltration is discontinuous with waves of melt propagating into the sink. We also observe strain localization and off-axis shearing to be more prominent

in samples with an opx-undersaturated source, suggesting a link between melt-rock reaction and deformation. From the low-ϕ series, we learn that stress-driven melt segregation is an effective way to create perturbations sufficiently large for the nucleation of reactive instabilities. We also observe that melt-rich pathways infiltrate farther into the sample at the same strain in samples with an opx-undersaturated melt source. In the following sections, we explore mechanisms that could explain these observations.

4.4.1 Mechanisms of coupling among deformation, reaction, and melt migration

The results from the two sets of experiments (high-ϕ source and low-ϕ source) suggest more than one mechanism of coupling between deformation and melt migration, depending upon the melt fraction in the source. First, consider the high-ϕ source series. The plot of melt fraction vs radius in Figure 4.11 demonstrates the much steeper gradient in melt fraction across the source-sink interface in the statically annealed sample than in the deformed samples. In the deformed samples, significant radial flow of melt from the source into the sink and corresponding flow of solid from the sink into the source has occurred. Because the grains in the source (initially 0.1-0.2 volume fraction) are completely disaggregated, as soon as the sample is sheared deformation at the source-sink interface is likely accommodated by melt-assisted granular flow (Rutter, 1997). Unlike granular flow of loose hard particles, this type of granular flow does not require dilation and can occur in a fully dense specimen. Consider the cross-sectional view of an aggregate of hexagonal grains coupled with a melt source as in Figure 4.28a. Under static conditions, no differential stress is applied to the grains in the aggregate and melt infiltration occurs through surface tension driven flow within pathways along triple junctions. When the aggregate is sheared in and out of the page as in Figure 4.28b, however, essentially no stress is supporting the grains along the interface with the melt source. Grain boundary sliding can then accommodate a significant portion of the strain. As grains, or chunks of grains as observed in Figure 4.9, raft off of the sink into the source, an equal volume of melt flows into the sink material as the volume of grains that flow into the source region. This intergranular (melt-filled) space can open up within the sink without any volume change of the sample as a whole. Melt-assisted granular flow may be the mechanism through which the melt waves form (as discussed

further below).

The model presented in Figure 4.28 applies both to samples in which the melt source is opx-saturated and to samples opx-undersaturated. Indeed, significant melt infiltration is observed in both cases, and plots of melt fraction as a function of radius yield similar results (Figure 4.11). However, more significant shear localization is observed in samples with an opx-undersaturated melt source, suggesting a link between reaction and deformation. While melt is transported far into the sink in both cases, the interconnected feedback loops represented in Figure 4.29 could lead to enhanced melt segregation and strain localization once the shear strain at the outer radius is greater than $\gamma = 1$.

Now, consider the low-ϕ source series. Although the melt fraction is much higher in the melt source than the sink (20% vs nominally melt-free), solid grains still form an interconnected framework throughout the sample, and the model in Figure 4.28 does not apply. In this case, coupling among deformation, reaction, and melt migration is achieved through stress-driven melt segregation creating perturbations in melt fraction large enough for the reactive instability to initiate, which then leads to the development of melt-rich, high-permeability pathways. These interconnected feedback loops are illustrated in Figure 4.29. But, are there other mechanisms linking melt-rock reaction and deformation? Another mechanistic link between deformation and metamorphism proposed by Rutter & Brodie (1995) that may apply to the scenario in these experiments is the formation of transiently fine-grained reaction products that could lead to weakening through grain size sensitive creep or increased melt fraction in the fine grained region. During dissolution of opx, grain size is reduced due to melting of individual grains. Olivine that is then precipitated nucleates as small grains that grow to some steady-state grain size. In the diffusion creep and grain boundary sliding regimes, this transient grain size reduction would reduce the strength of the fine grained region leading to enhanced strain localization (which in turn would lead to enhanced melt localization through stress-driven melt segregation). Further, the reduced grain size would lead to enhanced concentration of melt due to surface tension driven flow (Wark & Watson, 1998). While the experimental observations do not allow us to separate the effects of stress-driven melt segregation and transient grain size reduction, this mechanism may lead to additional feedbacks between deformation and reaction not included

in Figure 4.29.

4.4.2 Porosity waves in high-ϕ series?

An observation unique to the high-ϕ series is the presence of waves of high melt fraction propagating from the melt-rich core into the sink material. These waves appear to propagate faster near the center of the sample, forming chevron shaped features in the axial section. One interpretation for these waves is that they are porosity waves or magmons (Scott & Stevenson, 1984; Whitehead, 1987; Wiggins & Spiegelman, 1995; Rabinowicz, 2004). Porosity waves are predicted to form at an obstruction to melt flux. The source-sink interface acts as a significant barrier in permeability for the flow of melt into the sink driven by a pressure gradient within the melt with lower pressure at lower melt fractions (Stevenson, 1986). Magmons form when the matrix can deform by creep, compacting and decompacting, in response to spatial variations in melt fraction (Scott & Stevenson, 1984). The mechanism illustrated in Figure 4.28 provides a means for decompaction at the source-sink interface. Once a volume of melt has propagated into the matrix through this mechanism, a wave of compaction and decompaction accommodated by grain boundary sliding could propagate through the sink material.

Although they have been demonstrated in analogue materials (Whitehead, 1987), porosity waves have not been reported in high-pressure, high-temperature experiments on partially molten rocks. Porosity waves are one mechanism capable of creating episodic magmatism and variations in geochemical signatures in melt. In a numerical modeling study of the interactions between stress-driven melt segregation and compaction, Rabinowicz & Toplis (2009) found that the anisotropic permeability associated with stress-driven melt segregation, with low permeability parallel to the melt-rich bands, could nucleate porosity waves in response to buoyancy forces. The observations in these experiments suggest that porosity waves could be an important mechanism of melt transport in situations with a source and sink with dramatically different melt fractions. An applied shear stress appears to facilitate the formation of porosity waves, perhaps by initiating discontinuous melt infiltration along the source-sink interface.

4.4.3 Does the presence of opx help facilitate stress-driven melt segregation?

Stress-driven segregation occurs when the compaction length is less than the height of the sample (Holtzman et al., 2003). Estimates of the compaction length in olivine + MORB samples are on the order of a few millimeters, very close to the height of the samples in this study. In prior studies of stress-driven melt segregation chromite was used to reduce the permeability of the sample, which in turn reduces the compaction length so that it is much less than the height of the sample.

One interesting observation from the low-ϕ source series is that the bands are much more clearly defined in source regions of olivine + opx + MORB than in source regions of just olivine + MORB. This result suggests that the mixture of olivine + opx + MORB has a shorter compaction length than olivine + MORB. The shorter compaction length is likely due to the different interfacial energies and wetting properties at ol-opx-MORB or opx-opx-MORB triple junctions than at ol-ol-MORB triple junctions. Measurements of dihedral angles in statically annealed samples support the interpretation that melt-free triple junctions are more likely and that melt should be less interconnected with the presence of opx. Toramaru & Fujii (1986) found that in samples annealed at 1300°C and 1 GPa ol-opx-melt and opx-opx-melt triple junctions have a dihedral angle of $\sim$ 75°, which is significantly larger than ol-ol-melt dihedral angles reported by Waff & Bulau (1979) and Mei et al. (2002) of $\sim$ 30°. Because melt no longer forms a fully interconnected network when the dihedral angle is greater than 60°, the presence of 50% opx should significantly reduce the permeability of the source region in the opx-saturated source case.

4.4.4 Implications for melt extraction from Earth's mantle

In the experiments presented here, the chemical potential gradient that acts as the driving force for reaction-driven flow was created by coupling a reservoir of opx-undersaturated basaltic melt with an opx-bearing sink. In Earth, the scenario is different. The driving force for reaction-driven flow is the increasing solubility of opx in basaltic melt as pressure decreases, which is predicted to lead to coalescing of channels upward in the mantle (downstream in magma flow) (Spiegelman, 1996). Also, buoyancy effects, which

are negligible at the laboratory sample scale, play a significant role in Earth's mantle. Still, this study provides clues to the influences of deformation on other melt migration processes that can be extrapolated to mantle processes.

Results from the high-ϕ source and low-ϕ source series may apply to different geological scenarios. The very high melt fraction and complete disaggregation of grains in the high-ϕ source series might be most analogous to magma chamber processes. The experiments in the low-ϕ series are probably more appropriate for comparison to magma extraction from the mantle where partial melting produces melt that is extracted before significant amounts can accumulate.

One clear way in which deformation and reaction interact that is demonstrated in this study is that stress-driven segregation is an effective way to generate the perturbations necessary for a reactive instability to develop. In the geological record, tabular dunite bodies are often observed in association with shear zones (Kelemen & Dick, 1995; Webber et al., 2010). This result supports the concept that reaction and deformation lead to interconnected feedback loops. Both processes lead to the growth of a perturbation in melt fraction, though in different ways. Stress-driven melt segregation leads to growth in the amplitude of a perturbation with the geometry of the resulting melt-rich band controlled by the deformation geometry. Reaction-driven segregation leads to the propagation of a perturbation up a solubility gradient in opx. In this way, melt pathways resulting from deformation could facilitate the alignment favorable for focusing melt at a mid-ocean ridge (Katz et al., 2006), and melt-rock reaction could enhance the propagation.

4.5 Conclusions and future directions

The experiments in this study display complex interactions among deformation, melt-rock reaction, and melt migration. These mechanisms have previously been studied independently of one another. We observe many similar phenomena, such as the reactive infiltration instability and stress-driven melt segregation. The experiments demonstrate that, during deformation, these mechanisms can amplify one another. In order to develop a more quantitative understanding of the coupling mechanisms, future studies could explore different aspects of parameter space. In order to vary the reaction driving

force independent of deformation, different melt sources could be used that are undersaturated in opx to various degrees (Shaw et al., 1998). In order to explore the effects of deformation independent of the reactive driving force, a series of deformation experiments could be conducted to different strains and to the same strain at different stresses. The concept that stress-driven segregation nucleates reactive instabilities could also be further tested by first deforming a sample just to the point of creating perturbations in melt fraction along the source-sink interface and then letting the sample anneal to explore the development of the reactive instability under static conditions compared to reaction in the presence of deformation.

Table 4.1: Experiment Details

Sample	Source[1]	Sink[2]	An. (h)[a]	Def. (h)	γ_{max}	$\dot{\gamma}_{max}$	Figs.
High-ϕ source experiments							
PT0403	A_{us} (ring)	a	0	4	1.3	2×10^{-4}	4.10
PT0410	A_{us} (core)	a	6	0	0	0	4.4a, 4.5, 4.64.12b
PT0406	A_{us} (core)	a	4	4.5	2.3	1.4×10^{-4}	4.4d, 4.8, 4.9, 4.12d
PT0453	A_{us} (core)	a	1	7	1	4.0×10^{-5}	4.4c, 4.12c
PT0439	A_{sat} (core)	a	6	5	1.1	6.1×10^{-5}	4.4b, 4.12a
PT0442	none	a	7	6	1.2	5.8×10^{-5}	4.7
Low-ϕ source experiments							
PT0462	B_{us} (ring)	b	10 (19) [b]	0	0	0	4.14, 4.15e, 4.16
PT0472	B_{us} (ring)	b	0	7	2.2	1×10^{-4}	4.15b, 4.17b, 4.18b, 4.20b, 4.21
PT0491	B_{sat} (core)	b	0	7	2.5	1×10^{-4}	4.15c, 4.18c, 4.22a, 4.23a, 4.24a,b
PT0492	B_{sat} (ring)	b	0	7	2.5	1×10^{-4}	4.15a, 4.17a, 4.18a, 4.19, 4.20a
PT0500	B_{us} (core)	b	0	7	2.5	1×10^{-4}	4.15d, 4.18d, 4.22b,, 4.23b, 4.24c,d

[1] Source A_{dis} is 0.9 MORB + 0.1 olivine. Source A_{eq} is 0.8 MORB + 0.1 olivine + 0.1 enstatite. Source B_{dis} is 0.2 MORB + 0.8 olivine. Source B_{eq} is 0.2 MORB + 0.4 olivine + 0.4 enstatite.

[2] Sink a is 0.4 olivine + 0.4 enstatite + 0.15 chromite + 0.05 MORB. Sink b is 0.4 olivine + 0.4 enstatite.

[a] In several samples the specimen was at experimental pressure and temperature conditions for a significant amount of time prior to deformation due to failed attempts at deformation during which the applied angular displacement was accommodated at an interface rather than within the specimen. This anneal time does not include the hot isostatic press of the source and sink material before the couples were assembled.

[b] Sample PT0462 was initially annealed for 10 h at 1200°C. Half of the sample was then annealed for an additional 9 h at 1250°C for a total of 19 hours.

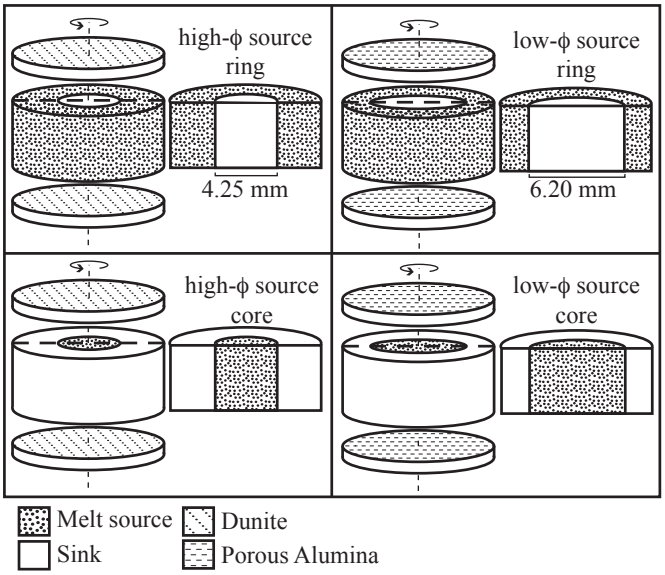

Figure 4.1: Schematic sketch of sample assembly.

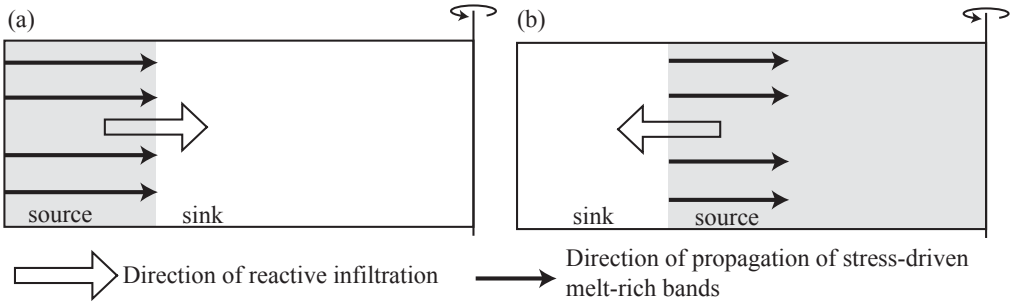

Figure 4.2: Sketch depicting the propagation direction for reactive and mechanical melt segregation processes in samples with the source as an outer ring (a) and as the core of the sample (b).

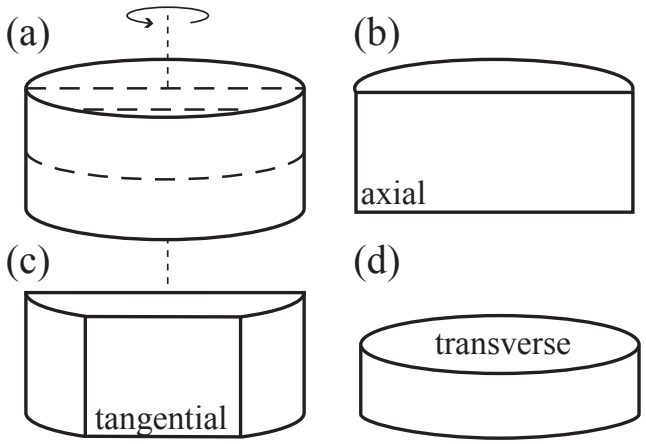

Figure 4.3: (a)Sketch of a cylindrical torsion sample with dashed lines indicating where cuts are made to polish faces for analysis. (b) The axial section (half of this section is referred to as the radial section). (c) The tangential section. (d) The transverse section.

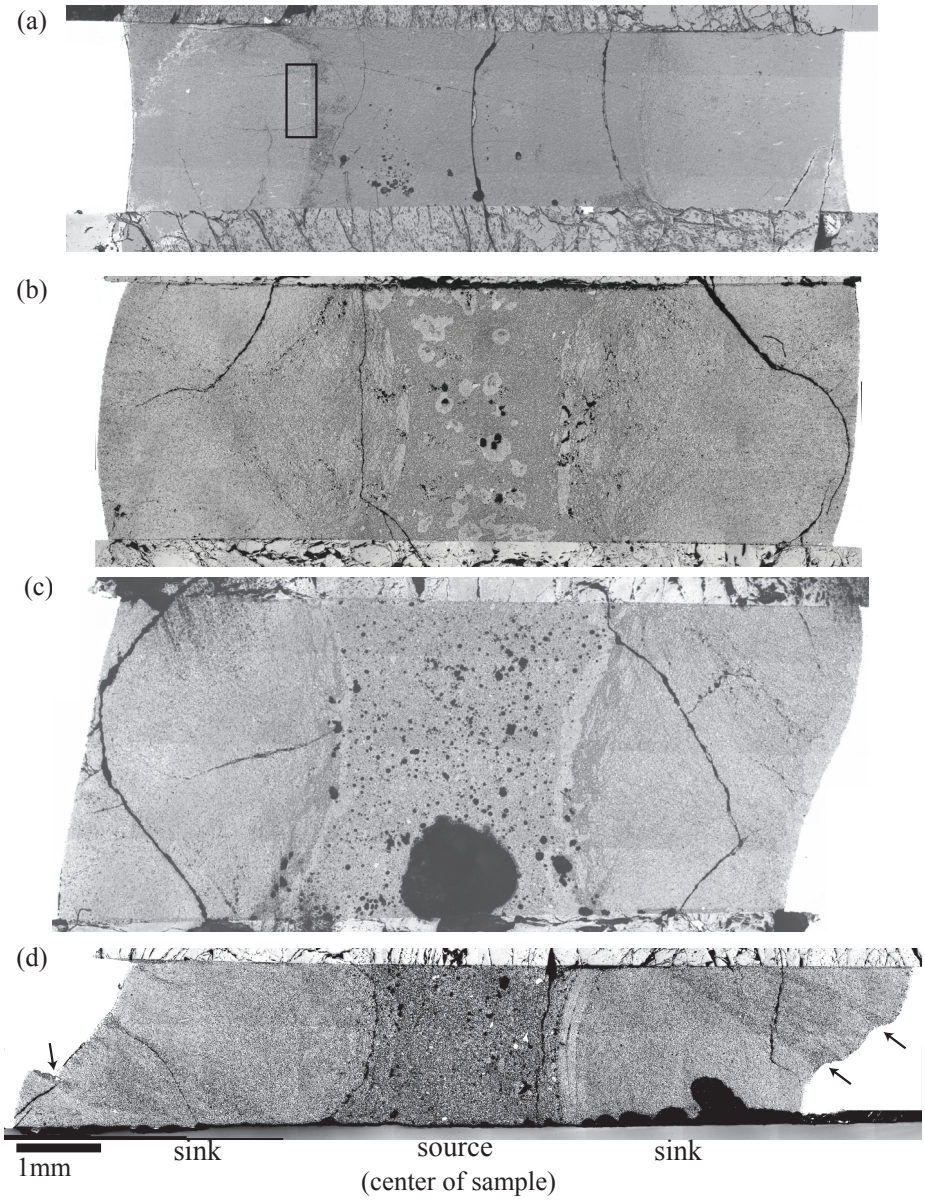

Figure 4.4: Optical reflected light images of polished and chemically etched axial sections. (a) Sample annealed for 6 h with an opx-undersaturated melt core (PT0410), the box indicates the area of detail in Figure 4.5. (b) Sample deformed to $\gamma = 1.1$ with an opx-saturated melt core (PT0439). (c) Sample deformed to $\gamma = 1$ with an opx-undersaturated melt core (PT0453). (d) Sample deformed to $\gamma = 2.3$ with an opx-undersaturated melt core (PT0406), the arrows indicate melt-rich bands that have accommodated shear offset.

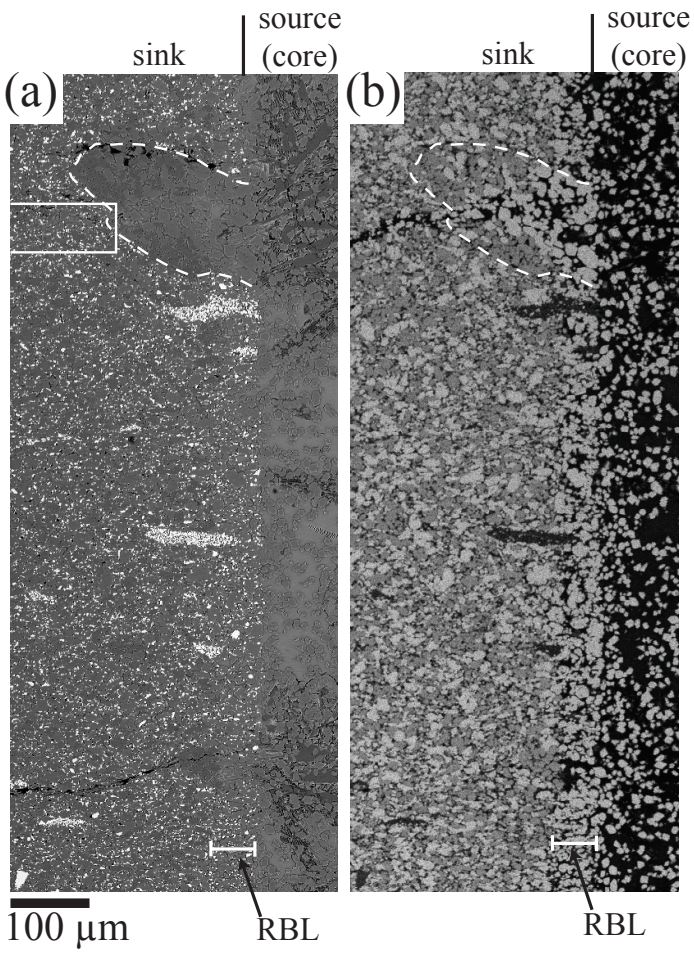

Figure 4.5: Electron microprobe images of a section of the source-sink interface in the statically annealed high-ϕ opx-undersaturated source sample (PT0410). The region in the sink absent in chromite from which a melt-rich finger propagates is outlined in both images. The reactive boundary layer that is the region in the sink from which all opx has been dissolved into the melt is labeled as RBL. (a)Backscattered electron image. Chromite is the brightest phase, olivine is light gray, opx is dark gray. The box indicates the region of detail in Figure 4.6. (b)X-ray map of Mg. Melt appears as purple, olivine appears green, opx, appears yellow.

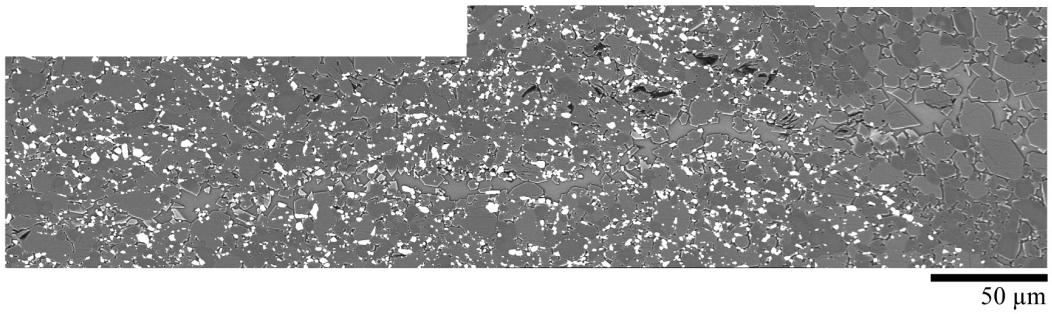

Figure 4.6: Backscattered SEM image of the region indicated in Figure 4.5.

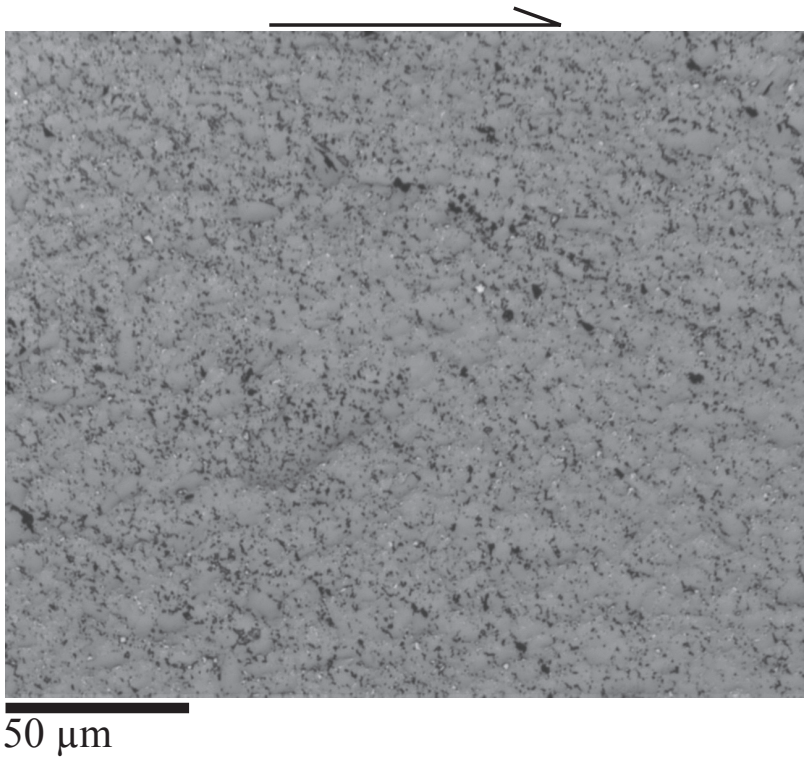

Figure 4.7: Optical reflected light micrograph of a portion of the tangential section of the sink material used in the high-ϕ source series deformed without a melt source. Shear direction is top-to-the-right as indicated by the arrow.

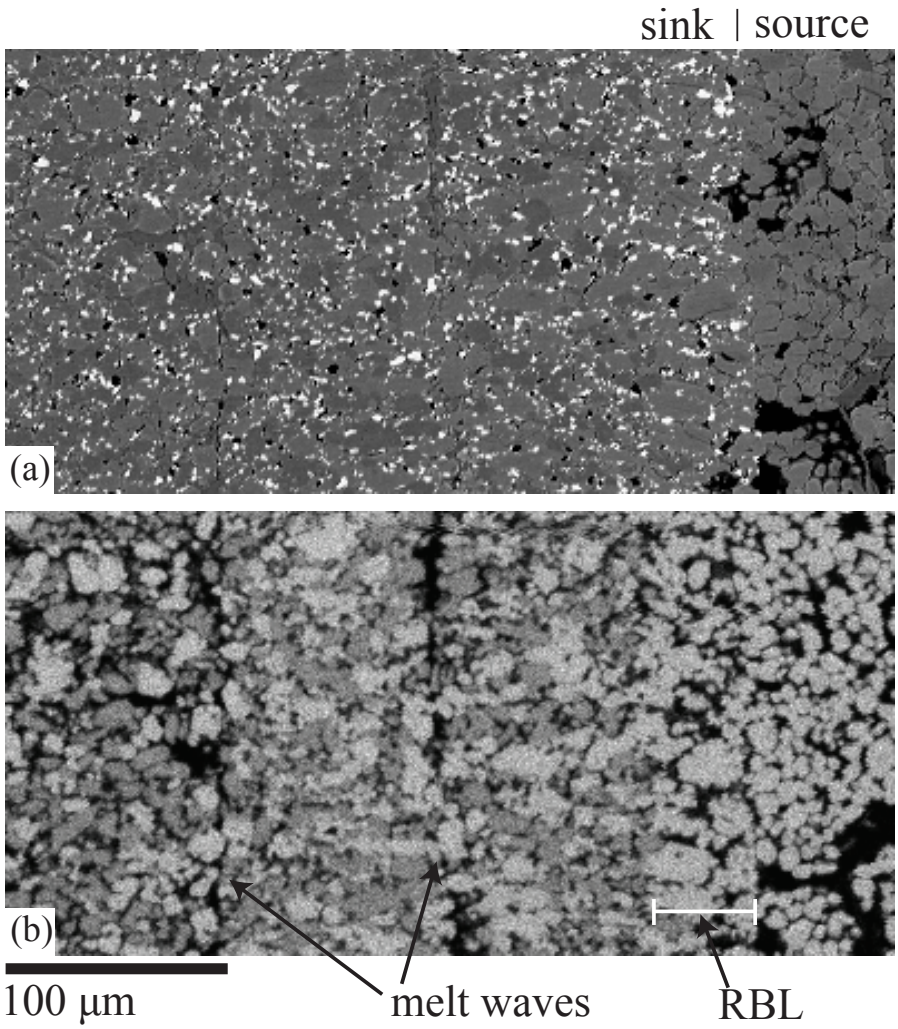

Figure 4.8: (a) BSE image and (b) Mg x-ray map of the source-sink interface in the sample deformed to high strain with opx-undersaturated melt core (PT0406). Note the bands of melt (purple) parallel to the source-sink interface. These images also clearly shows the reactive boundary layer as the region within the chromite-bearing sink absent in olivine (green).

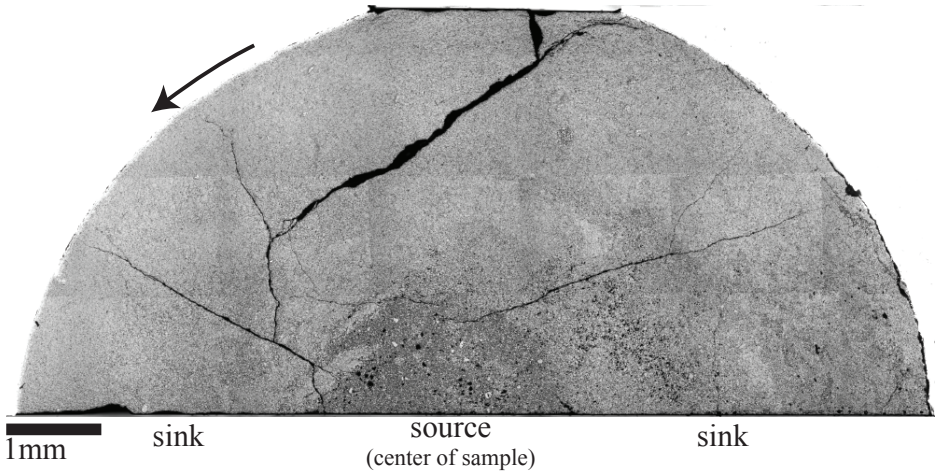

Figure 4.9: Optical reflected light micrograph of the transverse section (parallel to the shear plane) of the opx-undersaturated high-ϕ source sample deformed to high strain (PT0406, Figure 4.4d). The arrow indicated the direction of shear of this plane relative to the material below (into the page).

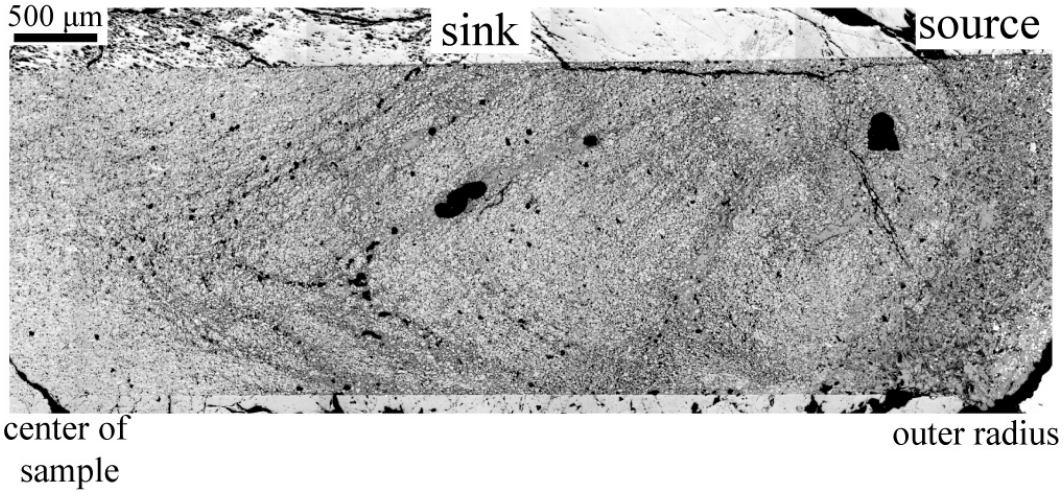

Figure 4.10: One half of the axial section (center of the sample at left of image) of the sample deformed with an opx-undersaturated melt source outside of the sink material. Note the chevron shaped melt waves propagating inward from the melt source.

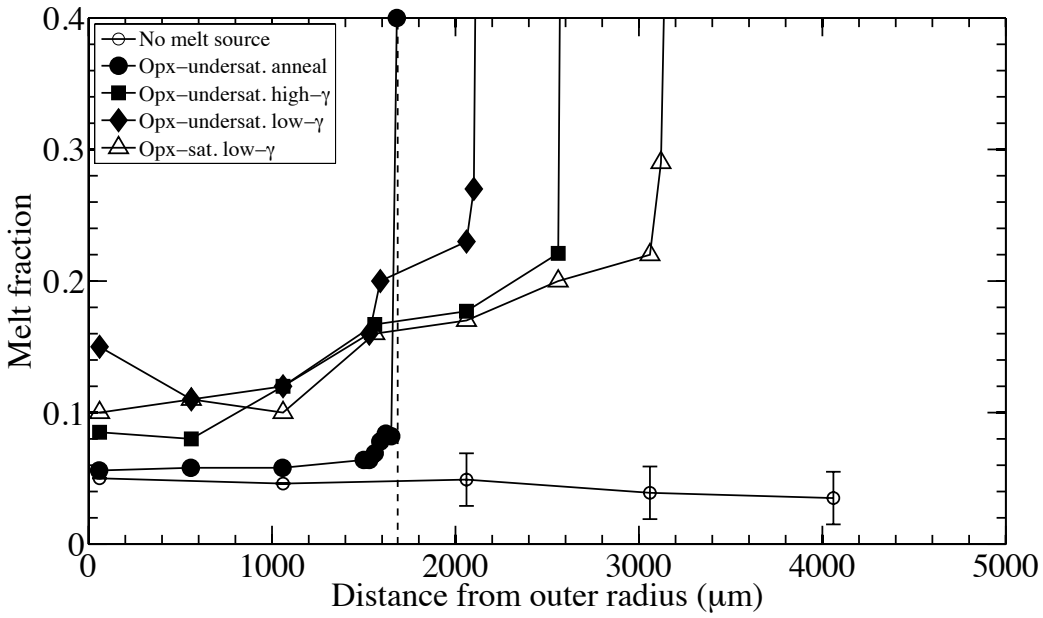

Figure 4.11: Plots of melt fraction as a function of distance from the outer radius of the sample. The vertical line is the location of the interface between source and sink at the beginning of the experiments. Representative error bars are plotted on data points in the transect of the sample with no melt source (deformation of sink material only).

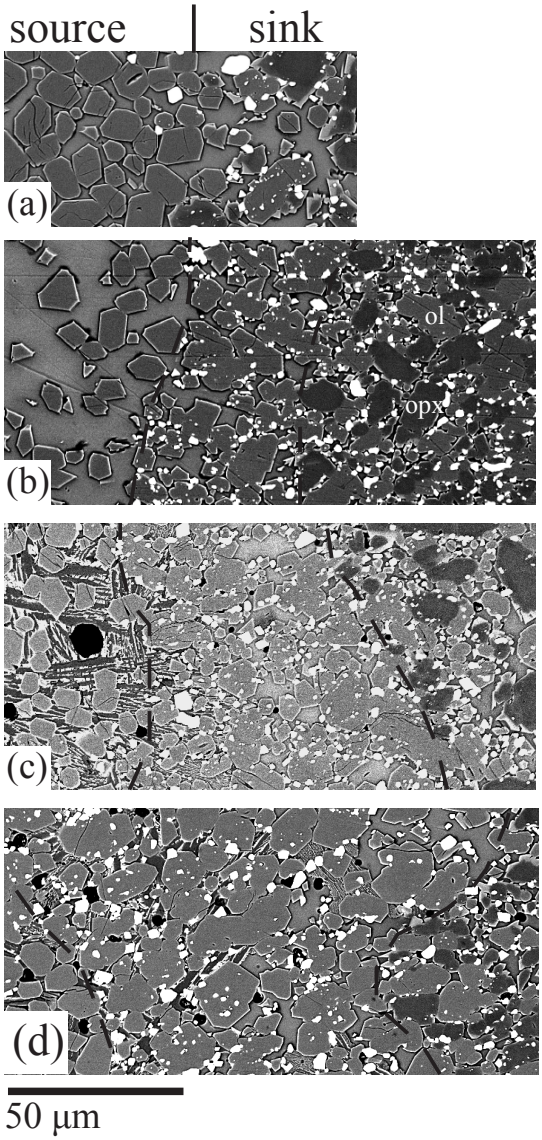

Figure 4.12: SEM backscattered electron images of the source-sink interface from (a) sample deformed with opx-saturated melt core (PT0439) (b) sample statically annealed with opx-undersaturated melt core (PT0410) (c) sample deformed to low strain with opx-undersaturated melt core (PT0453) and (d) sample deformed to high strain with opx-undersaturated melt core (PT0406). Note the absence of an opx-free reaction zone in (a) and the increasing width and irregularity of reaction zone with deformation.

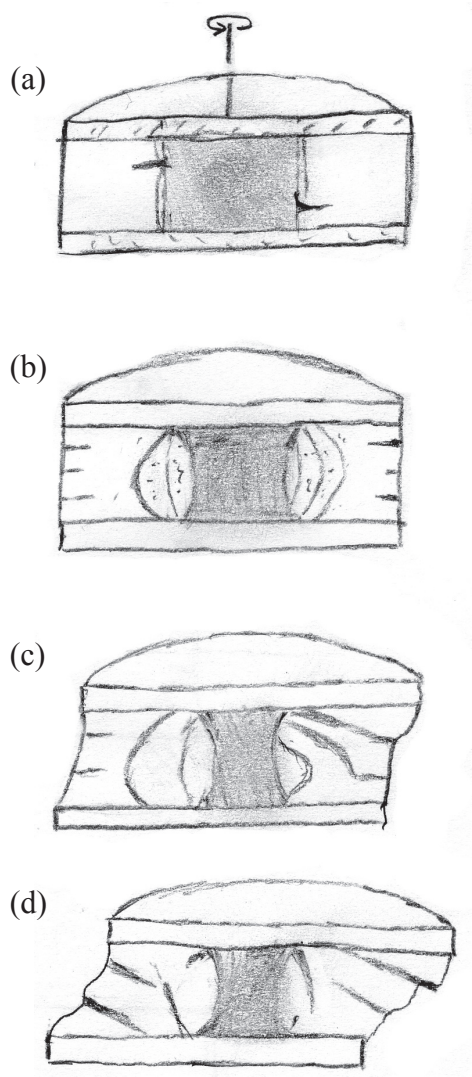

Figure 4.13: Interpretive sketches of the evolution of melt distribution within samples in the high-ϕ source series. (a) In the static anneal, fingers of melt going into the sink nucleate at perturbations in permeability along the source-sink interface. (b) At low strains, waves of melt propagate from the source into the sink as material from the sink rafts off into the source. When the outer radius of the sample reaches a shear strain of $\gamma = 1$, stress-induced melt-rich bands begin to form. (b) At some point as strain increases, some of the waves of melt parallel to the source-sink interface intersect the stress-induced melt-rich bands that propagate inward with increasing strain. (c) The intersection of these melt-rich structures leads to localized deformation within the melt-rich bands and off-axis shearing.

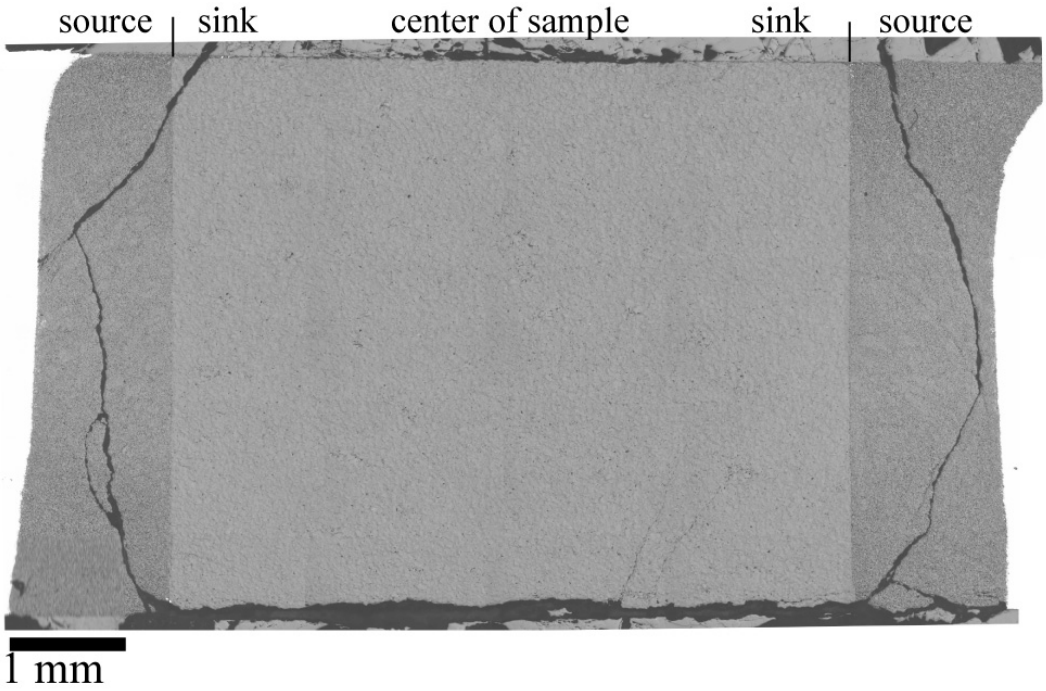

Figure 4.14: Polished axial section of low-ϕ opx-undersaturated source anneal after 10 h at 1200°C.

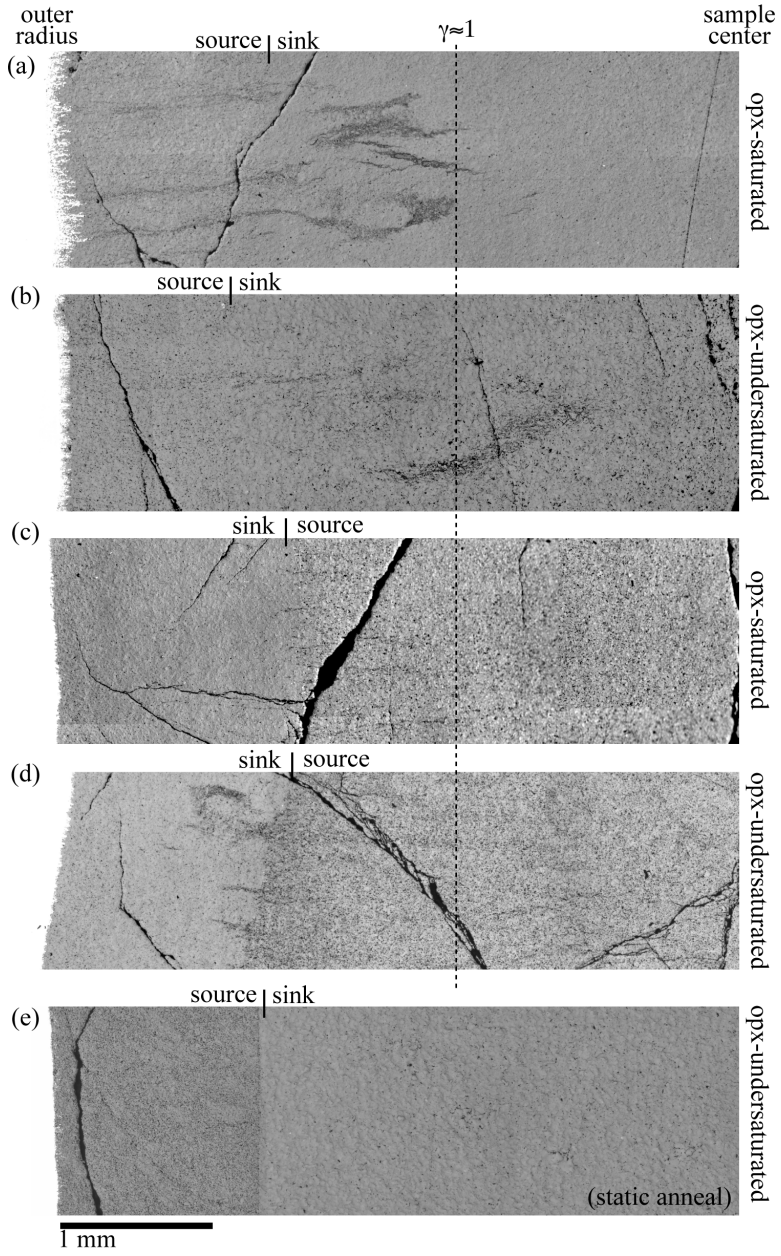

Figure 4.15: Portions of the radial section (center of sample to the right, outer radius to the left) of samples in the low-ϕ source series. Samples with the melt source as an outer ring are shown in a and b for opx-saturated and opx-undersaturated, respectively. Samples with the melt source as a central core are shown in c and d for opx-saturated and opx-undersaturated, respectively. A portion of the statically annealed sample is displayed in e.

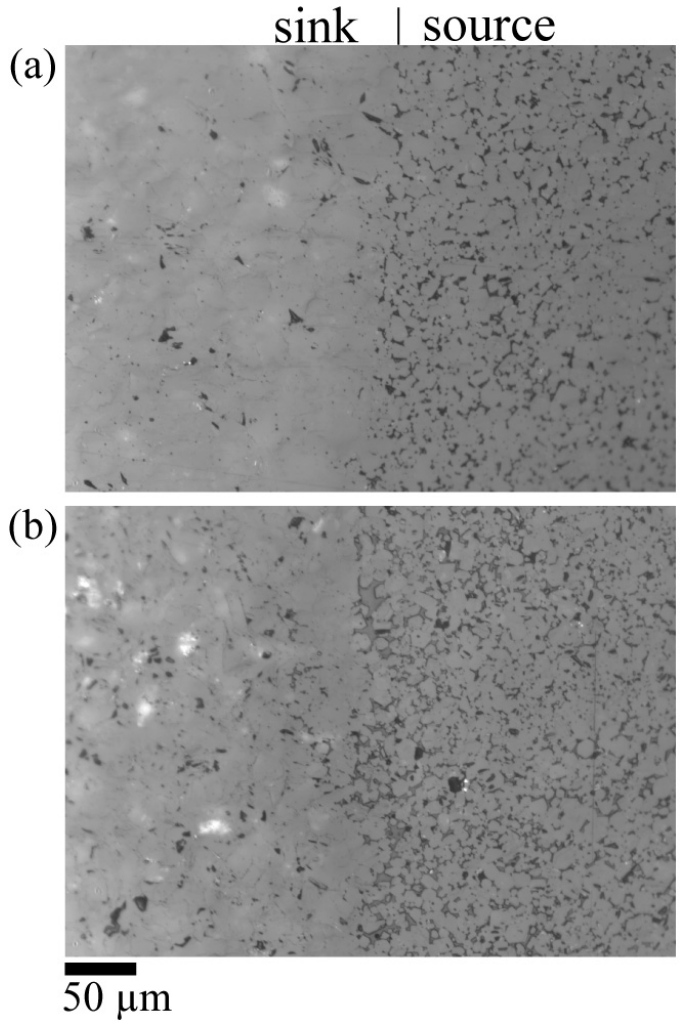

Figure 4.16: Higher resolution images of source-sink interface in low-ϕ opx-undersaturated source anneal (a) at 1200°C for 10 h (b) at 1250°C for an additional 9 h.

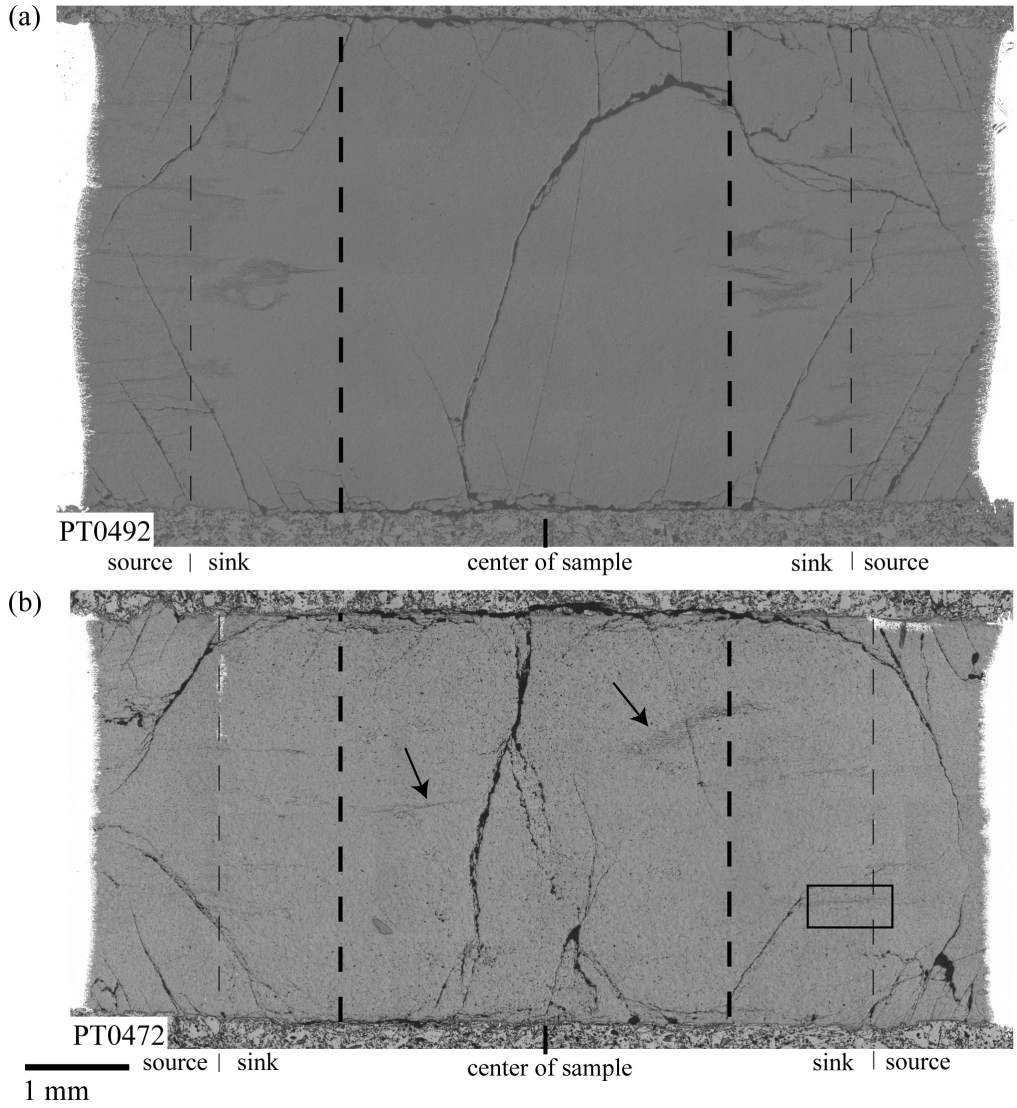

Figure 4.17: Polished axial sections of samples deformed to $\sim \gamma = 2.5$ with a low-ϕ source ring (a) opx-saturated source (PT0492) and (b) opx-undersaturated source (PT0472). Thin dashed lines indicate the original source sink interface. The arrows point to regions of high melt fraction closer to the center than the radius at which $\gamma \approx 1$ (indicated by the thick dashed lines).

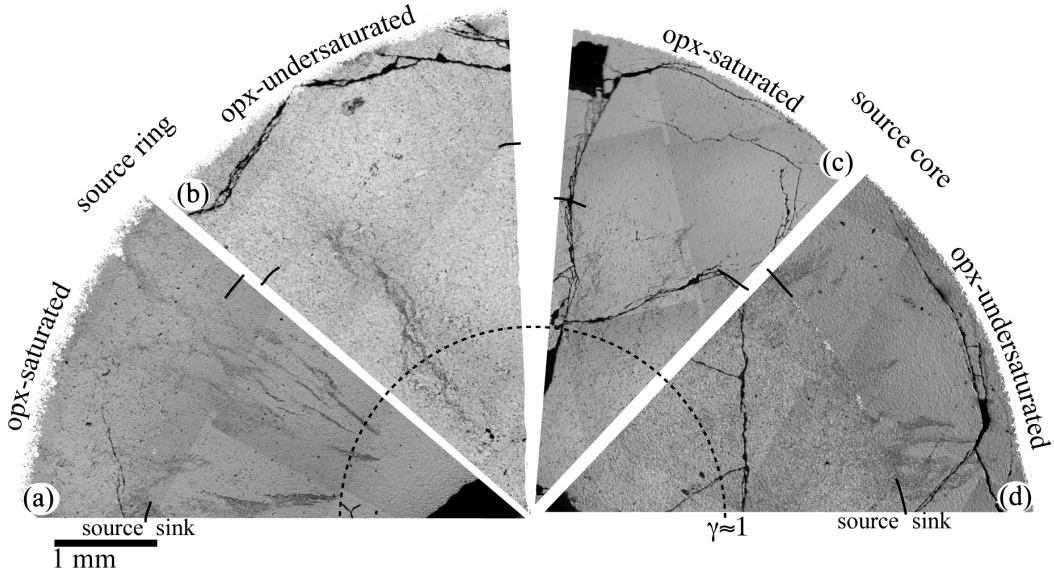

Figure 4.18: Portions of the transverse sections of the samples in the low-ϕ source series. Samples with the melt source as an outer ring are shown in a and b for opx-saturated and opx-undersaturated, respectively. Samples with the melt source as a central core are shown in c and d for opx-saturated and opx-undersaturated, respectively.

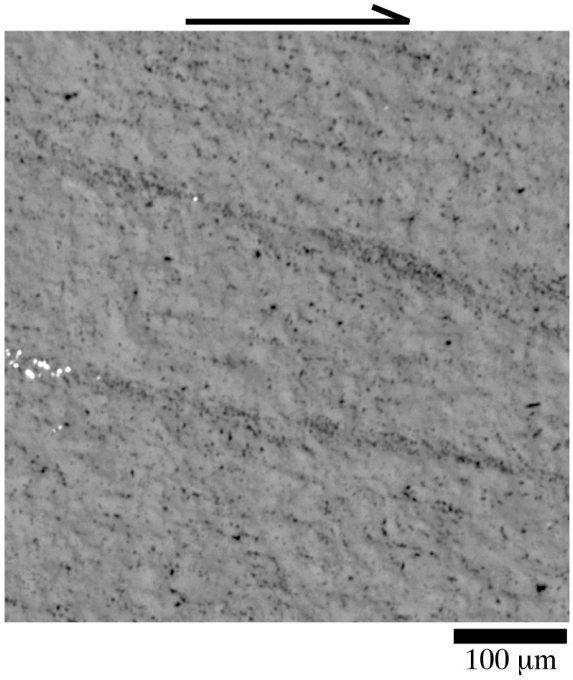

Figure 4.19: Optical reflected light image from the tangential section of the sample deformed with a low-ϕ opx-saturated source as a ring. This image is from within the source material.

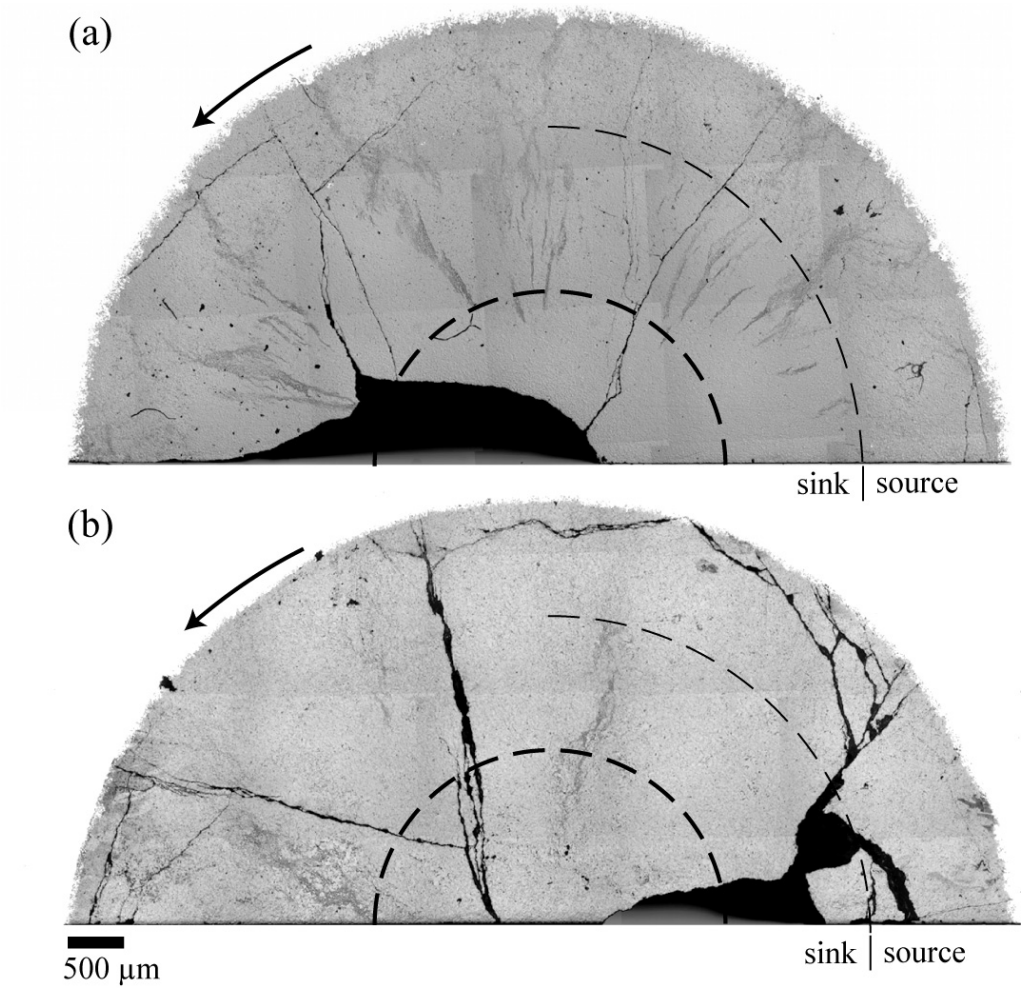

Figure 4.20: Transverse sections (perpendicular to the axial sections of Figure 4.17) of (a) sample deformed with an opx-saturated source ring (PT0492) and (b) sample deformed with an opx-undersaturated source ring (PT0472). The arrow indicates the direction of shear of this plane relative to the plane below (into the page). The thick dashed line indicates the radius of the sample at which $\gamma = 1$. The thin dashed line represents the original boundary between the source and the sink (shown for part of the inerface).

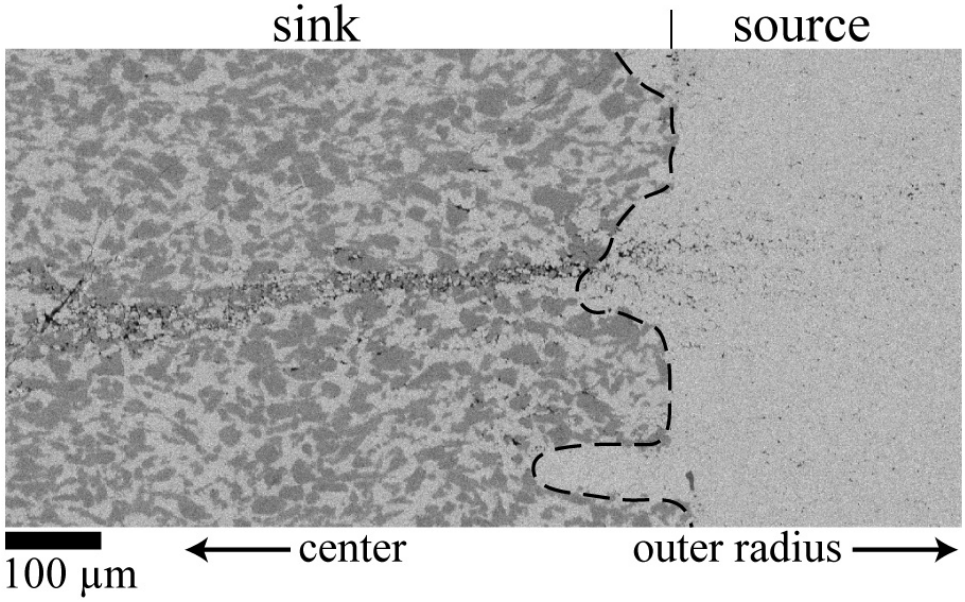

Figure 4.21: X-ray map of Mg of area indicated by the box in Figure 4.17a. The right side is the opx-undersaturated melt source and the left side is the opx-bearing sink. The dashed line indicates the boundary of the opx-bearing region. Melt infiltration is associated with one finger of apparent dissolution/precipitation reaction, while another finger of 100% olivine without melt present at the time of quenching is visible below.

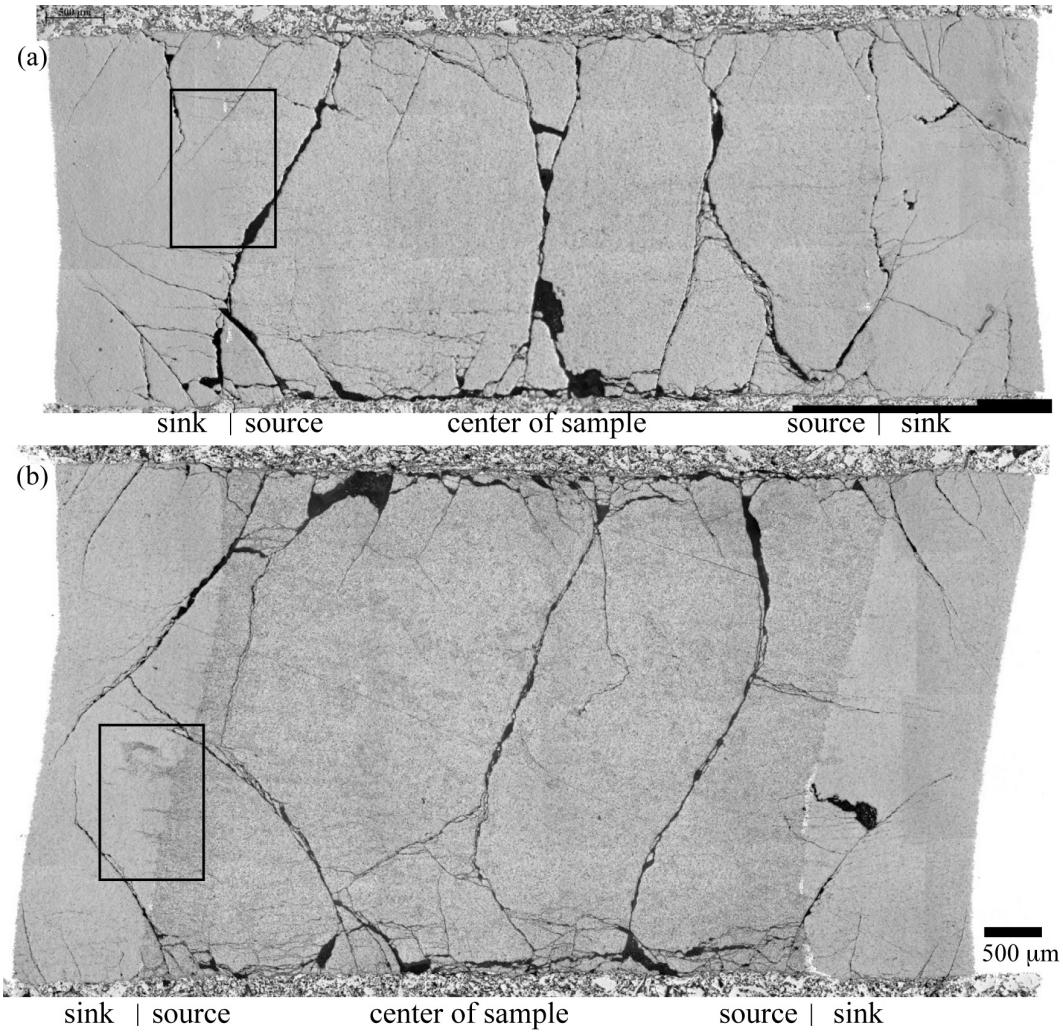

Figure 4.22: Polished axial sections of samples deformed to $\sim \gamma = 2.5$ with a low-ϕ source core. (a)opx-saturated source (PT0491) and (b)opx-undersaturated source (PT0500).

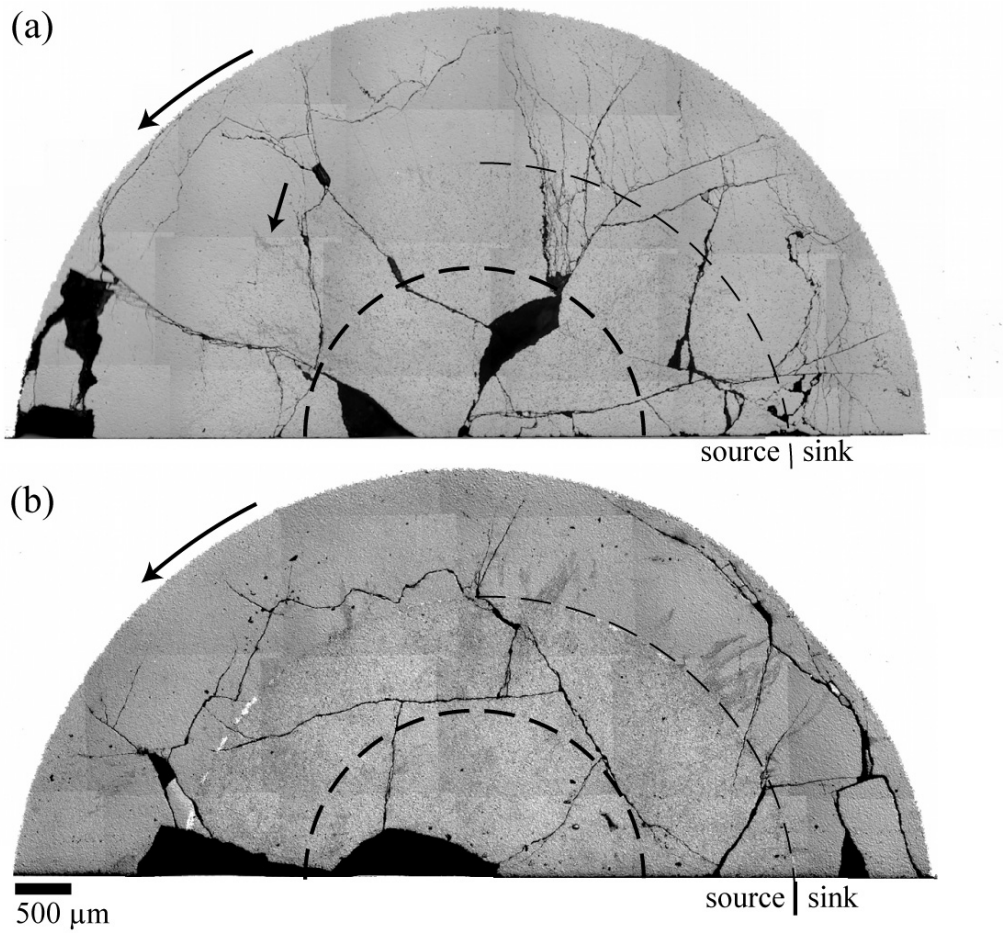

Figure 4.23: Transverse sections (perpendicular to the axial sections of Figure 4.22) of (a) sample deformed with an opx-saturated source core (PT0491) (the arrow indicates a melt infiltration feature) and (b) sample deformed with an opx-undersaturated source core (PT0500). The arrow outside the sample indicates the direction of shear of this plane relative to the plane below (into the page). The thick dashed line indicates the radius of the sample at which $\gamma = 1$. The thin dashed line represents the original boundary between the source and the sink (shown for part of the inerface).

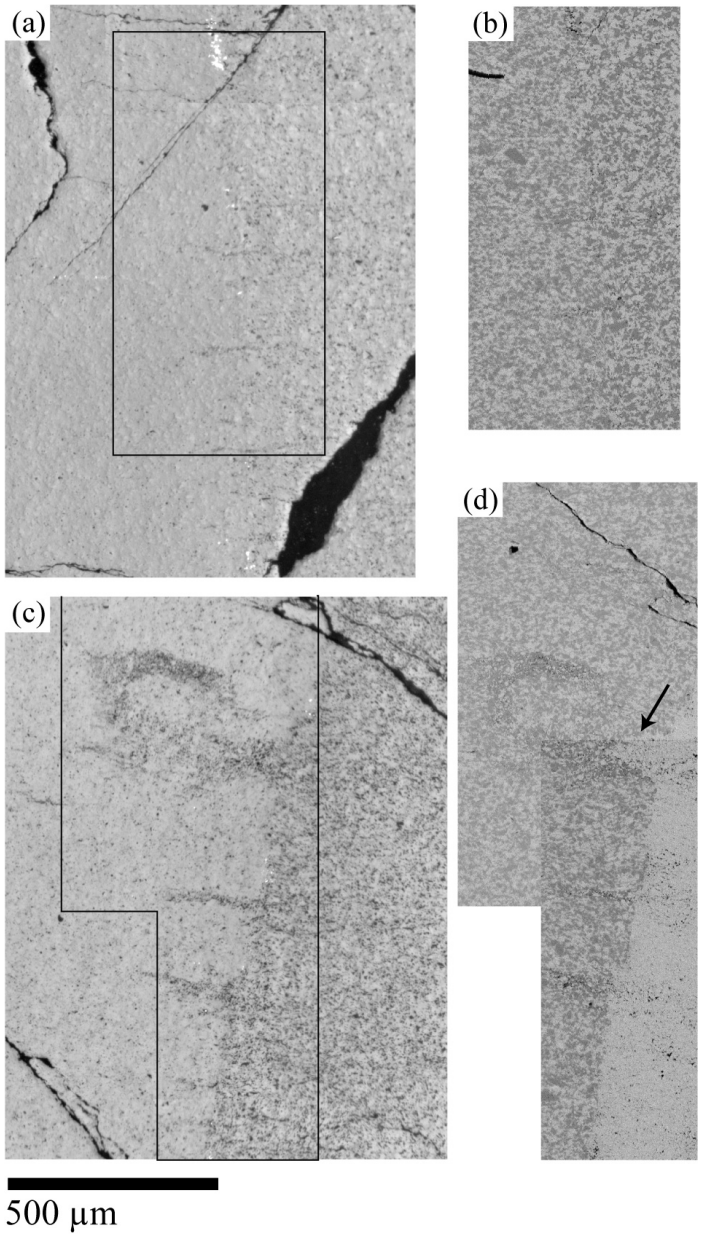

Figure 4.24: Detailed images of areas indicated in Figure 4.22. (a) Reflected light image of low-ϕ opx-undersaturated source. (b) X-ray map of Mg for region indicated in (a). (c) Reflected light image of low-ϕ opx-saturated source. (d) X-ray map of Mg for region indicated in (c). Arrow indicates region within the sink material of 100% olivine associated with melt infiltration.

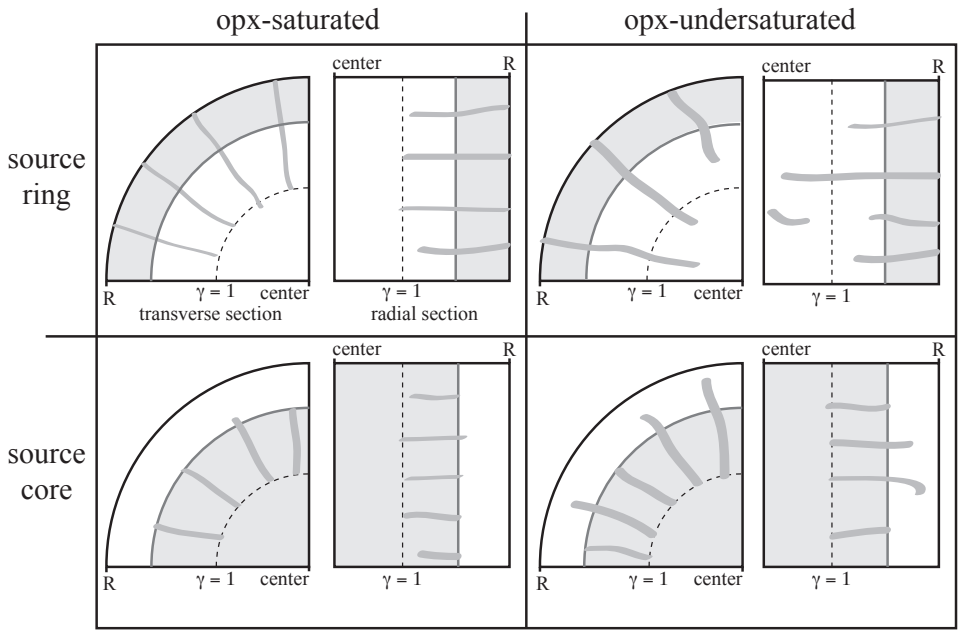

Figure 4.25: Summary of observations from deformed samples in the low-ϕ source series. The original source region is shaded gray, and the sink region is white. Darker gray bands represent high melt fraction channels that develop during deformation.

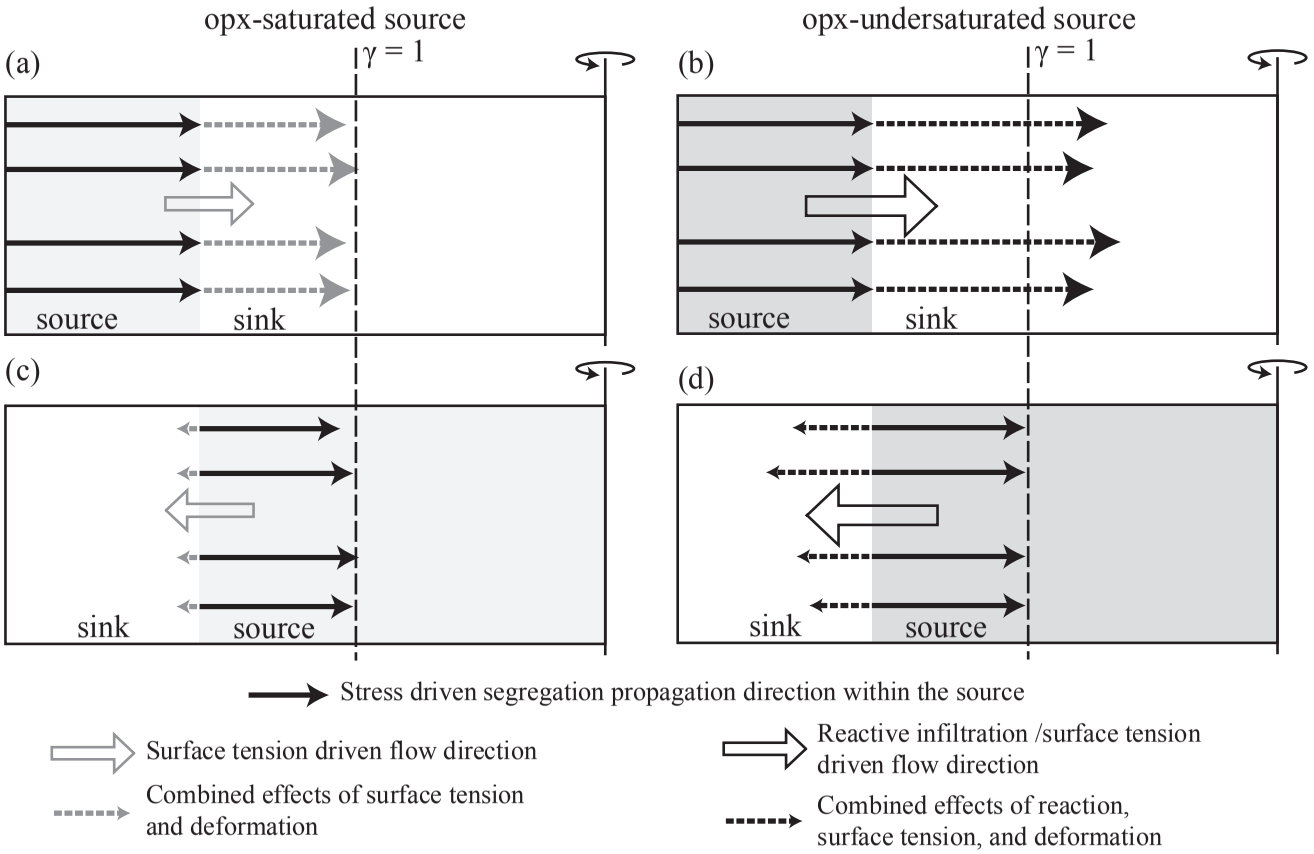

Figure 4.26: Summary of observations from deformed samples in the low-ϕ source series with interpretations of the various combinations of driving forces.

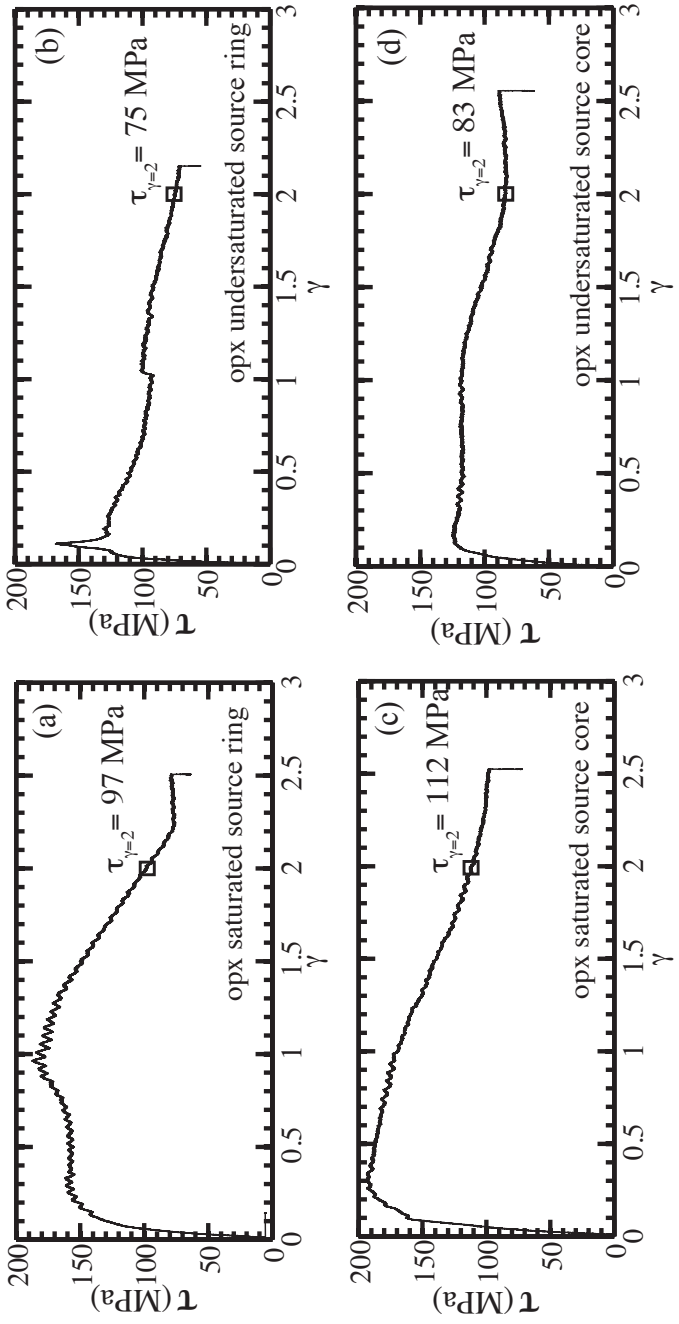

Figure 4.27: Shear stress vs strain for samples in the low-ϕ source series - (a) PT0492,(b) PT0472 ,(c) PT0491, and (d) PT0500. The shear stress at a strain of $\gamma = 2$ is noted on each plot.

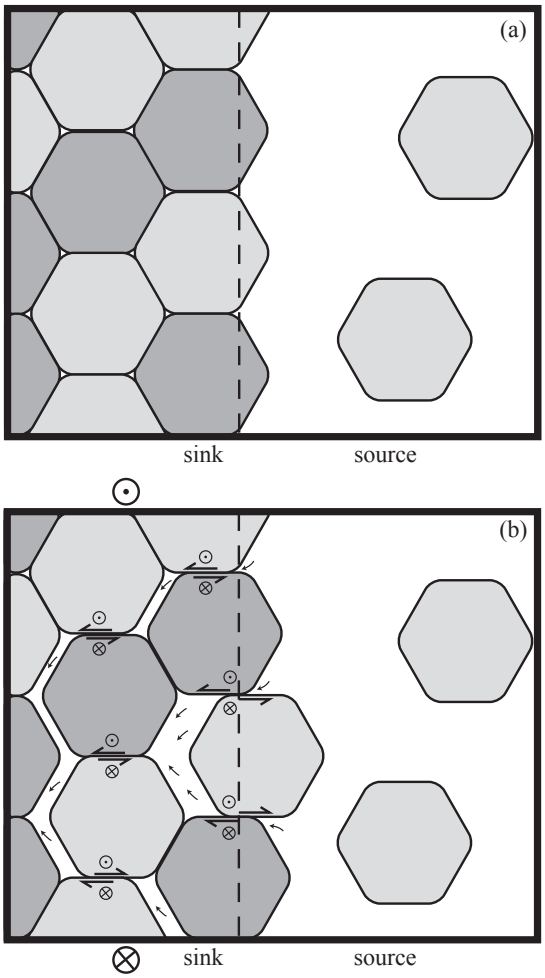

Figure 4.28: Conceptual model for enhanced melt infiltration due to shear deformation in the high-ϕ source series. (a) The source-sink couple under static conditions. Melt can infiltrate into the sink through interconnected pathways along triple junctions. (b) When the sample is sheared (top out of the page) deformation is accommodated through grain boundary sliding. Grains are unconstrained from sliding into the melt-rich source and as grains do so melt flows into the sink to conserve volume within the sample.

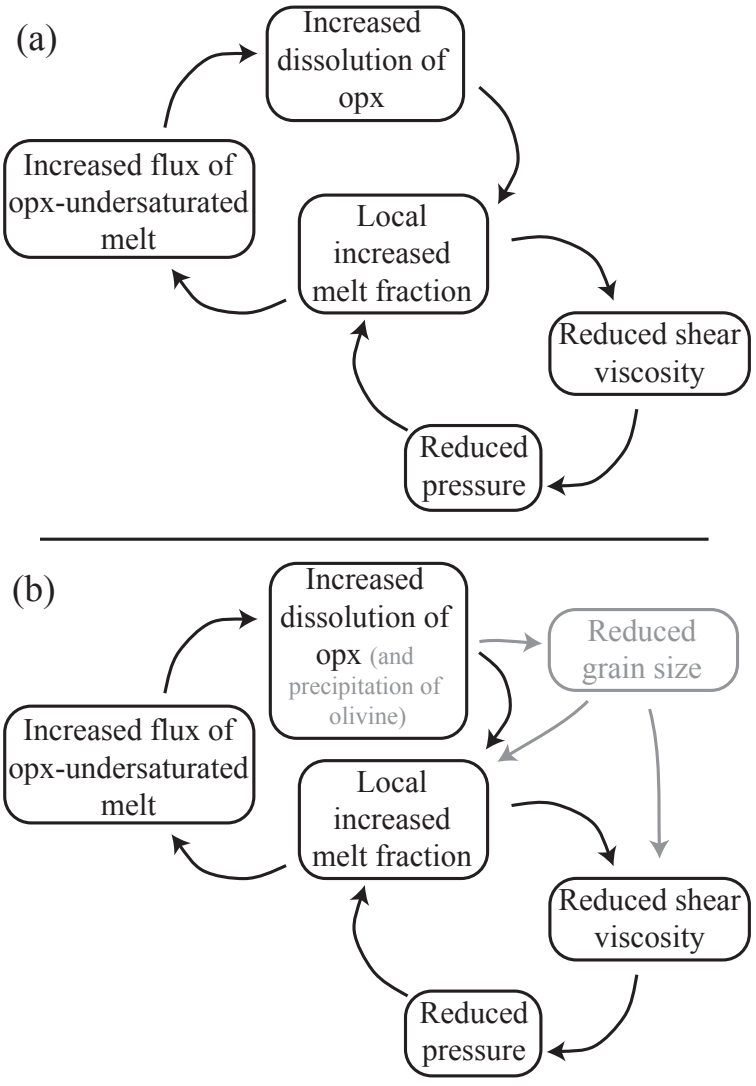

Figure 4.29: Schematic diagram of interconnected feedback loops that lead to the growth of a perturbation in melt fraction.

Chapter 5

Conclusions and Discussion

5.1 Summary of results

The experiments presented in the preceding chapters were designed to investigate the effects of deformation, melt-rock reaction, and surface tension on the distribution of melt in olivine-rich partially molten rocks. Some of the main conclusions are outlined here:

- **Chapter 2: Torsion experiments exploring stress-driven melt segregation demonstrate that the constant angle of $\sim 20^{\circ}$ to the shear plane, antithetic to the shear direction, is maintained to high shear strain ($\gamma > 7$), though this angle appears to become slightly smaller with increasing strain. The melt-rich bands accommodate significant strain localization, as evidenced by offsets in strain markers. Transient 'kinks' at high-angle to the shear plane may provide a mechanism for the redistribution of melt.**

- **Chapter 3: Static annealing experiments on samples in which melt has previously been segregated into melt-rich bands allow us to quantify the rate of homogenization of melt distribution. Comparison of the experimental results with numerical models of coupled fluid flow, matrix compaction/decompaction, and dissolution/precipitation with diffusive**

mass transport provides insight into the physical mechanisms of surface tension driven flow. At the sample scale, dissolution/precipitation allows for faster flux of solid material than viscous flow and is the rate controlling mechanism. This mechanism may also be important to consider at the grain size and perturbation length scales of the upper mantle in order to accurately quantify the effects of surface tension driven flow.

- **Chapter 4: Coupled deformation and reactive infiltration of melt facilitates greater melt transport than does either mechanism alone. Melt segregation resulting from deformation creates perturbations in melt fraction that initiate the reactive infiltration instability.**

5.1.1 Implications

Melt extraction at ridge systems

The vast majority of magma in Earth's mantle is associated with the production of new oceanic crust at mid-ocean ridges. Though the ocean-floor expression of mid-ocean ridges is on the order of kilometers, seismic studies have demonstrated that melt is produced within a several hundred kilometer wide region to depths of 150 km below spreading centers (Forsyth et al., 1998). A fundamental question that still does not have a complete answer is how the melt is extracted from this wide region of the mantle and focused within the width of the mid-ocean ridge.

The mechanism of stress-driven melt segregation explored here may play an important role in focusing melt. Numerical modeling has demonstrated that in a corner-flow geometry beneath a mid-ocean spreading center, stress-driven alignment and segregation of melt is predicted to have a focussing effect on the melt (Katz et al., 2006; Katz, 2008). Results presented in Chapter 2 support prior findings of deformation-induced melt-rich pathways at a consistent orientation relative to the shear geometry. The mechanism of reorganization of the network of melt bands through high-angle 'kinks' could be a way that these high permeability pathways remain focused toward a mid-ocean ridge in Earth. The torsion experiments provide compelling evidence that the onset of melt-rich bands is linked to achieving a critical shear strain of $\gamma = 1$. There does

not appear to be a minimum yield stress (within the range of stresses explored, > 10 MPa) needed to overcome interfacial tension forces. This result, along with the results presented in Chapter 3, suggest that melt-rich bands could be stable in Earth across a wide range of length scales at very low differential stresses. The interactions between reactive infiltration and stress-driven melt segregation presented in Chapter 4 demonstrate that melt transport is more effective when both mechanisms are combined than with either mechanism alone. Further experiments to explore the physics of coupling between deformation and reaction along with extended numerical models that combine both processes will lead to a greater understanding of melt migration in Earth's upper mantle.

Strain localization at plate boundaries

One of the goals of studying mantle convection through numerical modeling has been to determine the conditions necessary for the formation of lithospheric plates (e.g., Tackley, 2000a,b). These studies have demonstrated that the formation and continued existence of lithospheric plates requires strain localization. Continental rifting generally requires that strain be localized within a detachment zone that is large-scale ($\sim$ 1 km wide) and long-lived (millions of years) (e.g., Hopper & Buck, 1993, 1998). Extrapolation from experiments shows that deformation in the lithospheric mantle occurs primarily in the dislocation creep regime ($n = 3 - 5$ in equation 1.1). In this regime, although shear viscosity ($\eta = \tau/\dot{\gamma}$) becomes smaller at higher stress due to the power law dependence of strain rate on stress, stress still increases with increasing strain rate preventing localization. Shear zones occur as a result of a plastic instability involving a process that leads to strain-rate-weakening conditions in which stress decreases with increasing strain rate. Constitutive equations required to create plastic instabilities and plate-like behavior differ from those extrapolated from laboratory experiments on homogeneous material, such as equation 1.1 (e.g., Tackley, 2000b).

The rheological implication of a partial melt indicate that magma could play a significant role in facilitating strain localization at plate boundaries. In the introduction, the observed exponential dependence of viscosity on melt fraction (Equation 1.3) was discussed. This formulation works well for melt with a homogeneous distribution, but rocks in which melt has segregated into melt-rich bands display much greater weakening.

One hypothesis is that the stress and strain rate within a sample should vary spatially depending upon local melt fraction according to Equation 1.3 such that

$$\dot{\varepsilon}_{\phi_{seg}} = V_b \dot{\varepsilon}_0 \exp[-\alpha\phi_b] + V_{nb} \dot{\varepsilon}_0 \exp[-\alpha\phi_{nb}] \tag{5.1}$$

where V_b and V_{nb} represent the volume fraction of band and non-band regions within the sample and ϕ_b and ϕ_{nb} represent the melt fraction within band and non-band regions.

We can test this formulation in a series of samples deformed in torsion prepared similarly to those discussed in Chapter 2, but with a range of chromite fractions (0.02, 0.06, 0.1 and 0.2). We compare the rheological data from these samples to that from a nominally melt-free sample and a sample with melt, but no chromite. The melt within the samples segregates to different extents. From images of the samples we can observe the area fraction of bands (which should correspond to the volume fraction) and the melt fraction in the band and non-band regions. The rheological data from this series of experiments is plotted in Figure 5.1. Curves are also plotted for a combined flow law (diffusion creep, grain boundary sliding, and dislocation creep) using the volume weighting of Equation **??**. The data demonstrate and the formulation predicts modest weakening associated with a few percent melt homogeneously distributed. The formulation using the observed melt distributions in the samples predicts a smooth decrease in strength, ultimately leading to an increase in strain rate by nearly an order of magnitude for a given stress. However, the data demonstrate that all of the samples in which some amount of segregation is observed, the samples are significantly weaker than a homogeneously distributed melt. That is, there is not a smooth transition from homogeneously distributed melt to segregated melt.

The lithosphere-asthenosphere boundary (LAB)

In addition to the formation of lateral plate boundaries, strain localization is also crucial for decoupling at the lower boundary of lithospheric plates. Earth's lithosphere, or mechanical boundary layer, lies above the convecting mantle and follows the plate motions we observe at Earth's surface. To a first order the mechanical boundary layer coincides with the thermal boundary layer, which is the conductive lid above the adiabatically cooling mantle, and with the chemical boundary layer, which is the chemically depleted region that lies above fertile mantle. Though the concept of localized deformation at

the base of the lithosphere is fundamental to plate tectonics, many specific traits of the lithosphere-asthenosphere boundary (LAB) remain unclear. Among the key questions are the depth (and variability of depth) of the LAB, the magnitude of rheological contrast, and the mechanism for producing the rheological contrast.

Several mechanisms are likely to play a role in creating the LAB. The colder temperature within the thermal boundary layer should result in a higher viscosity within the conductive lid, and this effect certainly plays a role in creating the mechanical boundary layer. However, temperature effects alone do not result in a dramatic enough rheological contrast to produce plates. The chemical depletion of mantle peridotite, most importantly dehydration of olivine, through partial melting and removal of the melt provides additional means of increasing the viscosity of the lithosphere relative to the more fertile, and hydrated, asthenosphere (Hirth & Kohlstedt, 1996). Viscosity contrast imposed by the chemical boundary layer amplifies the effects of temperature and could provide a mechanism for a narrow region across which viscosity is reduced.

The presence of partial melt may also play a role in reducing the viscosity of the upper portion of the asthenosphere. Among other lines of evidence, the presence of a partial melt in the asthenosphere has been inferred from geochemical signatures suggesting an asthenospheric sources (Hirano et al., 2006) and from a predicted minimum in water solubility at the LAB due to a sharp decrease in water solubility in aluminous orthopyroxene (Mierdel et al., 2007). In a recent study by Kawakatsu et al. (2009), the large shear wave velocity reduction at the LAB was interpreted to require horizontal melt-rich layers in an otherwise melt-free mantle. Stress-driven melt segregation provides an attractive mechanism to account for this observation. However, the balance of rates of melt production and melt extraction from the upper asthenosphere remains poorly constrained.

5.2 Remaining questions - Future directions

5.2.1 Scaling to Earth

The experimental results presented in Chapter 2 support the previously published result that band spacing is $\sim 0.2\delta_c$; however, significant uncertainty remains in extrapolating this result to the length scales and strain rates appropriate for Earth's mantle. The

linear relationship observed across the limited range of compaction lengths tested experimentally may not apply when extrapolating to the length and time scales of the mantle. The compaction length scaling argument provides a prediction for the maximum band spacing, while a scaling approach centered on band thickness was presented by Takei & Hier-Majumder (2009). The formulation of surface tension driven flow allowed the authors to identify a perturbation length scale below which the homogenization rate from surface tension driven flow exceeds the segregation rate from stress-driven melt segregation.

5.2.2 Interactions between deformation and reaction

The results presented in Chapter 4 are groundbreaking from the standpoint of experimental design, and they demonstrate that stress-driven and reaction-driven mechanisms can work in concert. This study suggests that it would be useful to explore reaction/deformation interactions systematically throughout a broader range of the parameter space. A series of experiments exploring the distance that instabilities grow into the sink as a function of stress and finite strain could yield the results that are essential for including this mechanism in numerical models that can be applied to Earth's mantle. The concept that deformation creates perturbations in melt fraction that can then initiate into reactive channels could be tested by coupling opx-undersaturated source material that has been deformed to create melt-rich bands with sink material rich in opx. More detailed observations of the grain-scale processes occurring within melt-infiltration features could provide insight into the physics of the links between melt-rock reaction and deformation. For example, does grain size change systematically during the melt-rock reaction process?

5.2.3 Quantification of rheological implications

While the torsion deformation geometry has proven to be powerful for investigating microstructural evolution within samples deformed to high strains, it is more difficult to achieve the rigor of uniaxial compression tests in a gas-medium apparatus in obtaining high-precision rheological data. However, the results presented in Figure 5.1 and a compilation of data on samples of fine-grained lherzolite in Figure 5.2 demonstrate that

results consistent with other deformation geometries can be obtained. In the compilation of lherzolite data, rheological data obtained through different methods is compared. Data from one sample deformed in torsion at a constant torque in which torque steps were taken to measure the dependence of strain rate on stress is compared with unpublished data from two samples deformed in direct shear by Mark Zimmerman and a series of samples deformed in uniaxial compression (Zimmerman & Kohlstedt, 2004). The data agree quite well, suggesting that rheological data from torsion tests can be useful in probing the evolution of rheological properties of rocks deformed to high shear strain. Determining methods of quantifying the viscosity reduction associated with melt segregation is critical for the incorporation of robust flow laws into numerical models. In ongoing efforts with Ben Holtzman, we explore such formulations as Equation **??** to represent the rheological implications of stress-driven melt segregation.

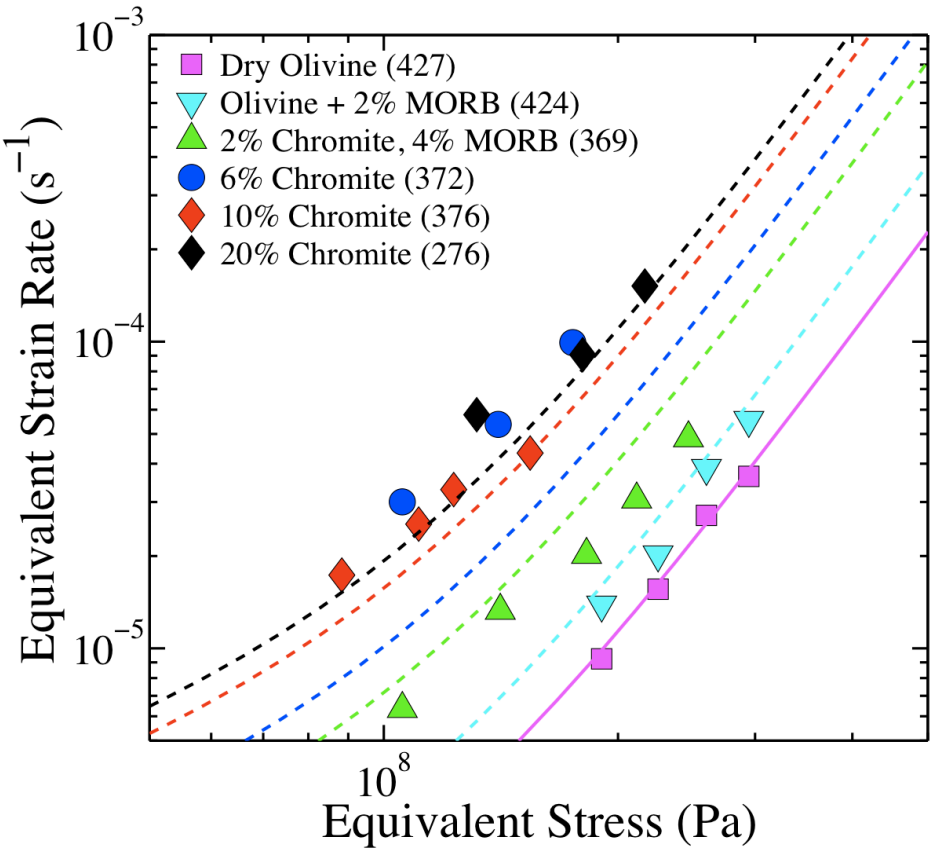

Figure 5.1: Log log plot of equivalent stress vs equivalent strain rate for melt-free olivine (squares) and partially molten olivine with various chromite fractions deformed in torsion at constant torque.

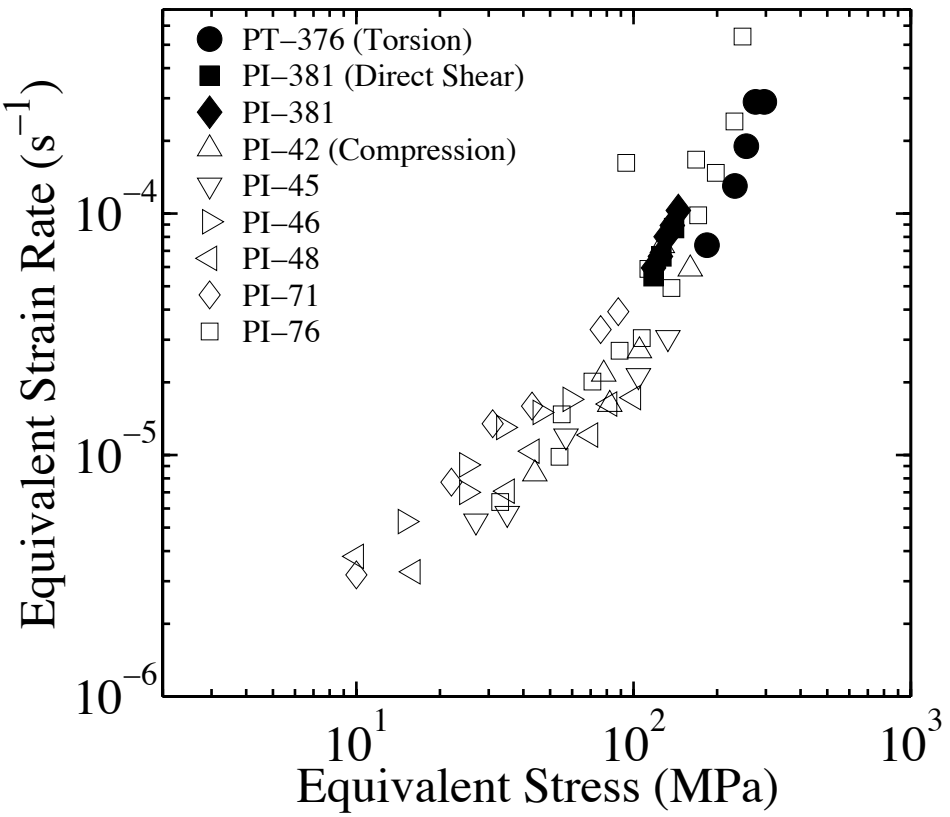

Figure 5.2: Compilation of creep data from samples of partially molten lherzolite deformed in uniaxial compression (open symbols), direct shear (filled diamonds and squares), and torsion (filled circles).

Bibliography

Aharonov, E., Spiegelman, M., & Kelemen, P. B. (1997). Three-dimensional flow and reaction in porous media: Implications for the earth's mantle and sedimentary basins. *Journal of Geophysical Research-Solid Earth*, *102*(B7), 14821–14833.

Aharonov, E., Whitehead, J., Kelemen, P. B., & Spiegelman, M. (1995). Channeling instability of upwelling melt in the mantle. *Journal of Geophysical Research-Solid Earth*, *100*(B10), 20433–20450.

Bercovici, D., & Ricard, Y. (2003). Energetics of a two-phase model of lithospheric damage, shear localization and plate-boundary formation. *Geophysical Journal International*, *152*(3), 581–596.

Bercovici, D., Ricard, Y., & Schubert, G. (2001). A two-phase model for compaction and damage 1. general theory. *Journal of Geophysical Research-Solid Earth*, *106*(B5), 8887–8906.

Boudier, F., Ceuleneer, G., & Nicolas, A. (1988). Shear zones, thrusts and related magmatism in the oman ophiolite - initiation of thrusting on an oceanic ridge. *Tectonophysics*, *151*(1-4), 275–296.

Boudier, F., Nicolas, A., & Ildefonse, B. (1996). Magma chambers in the oman ophiolite: Fed from the top and the bottom. *Earth and Planetary Science Letters*, *144*(1-2), 239–250.

Braun, M., & Kelemen, P. (2002). Dunite distribution in the oman ophiolite: Implications for melt flux through porous dunite conduits. *Geochem Geophy Geosy*, *3*, 8603.

Brown, M. (2006). Melt extraction from the lower continental crust of orogens: the field evidence. In M. Brown, & T. Rushmer (Eds.) *Evolution and Differentiation of the Continental Crust*, (pp. 331–376). Cambridge University Press.

Bussod, G., & Christie, J. (1991). Textural development and melt topology in spinel lherzolite experimentally deformed at hypersolidus conditions. *Journal of Petrology*, *Special Lherzolite Issu*, 17–39.

Butler, S. L. (2009). The effects of buoyancy on shear-induced melt bands in a compacting porous medium. *Physics of the Earth and Planetary Interiors*, *173*(1-2), 51–59.

Ceuleneer, G., Nicolas, A., & Boudier, F. (1988). Mantle flow patterns at an oceanic spreading center - the oman peridotites record. *Tectonophysics*, *151*(1-4), 1–26.

Cooper, R. F., & Kohlstedt, D. L. (1984a). Sintering of olivine and olivine-basalt aggregates. *Phys Chem Miner*, *11*(1), 5–16.

Cooper, R. F., & Kohlstedt, D. L. (1984b). Solution-precipitation enhanced diffusional creep of partially molten olivine-basalt aggregates during hot-pressing. *Tectonophysics*, *107*(3-4), 207–233.

Cooper, R. F., & Kohlstedt, D. L. (1986). Rheology and structure of olivine-basalt partial melts. *J Geophys Res-Solid*, *91*(B9), 9315–9323.

Cooper, R. F., Kohlstedt, D. L., & Chyung, K. (1989). Solution-precipitation enhanced creep in solid-liquid aggregates which display a non-zero dihedral angle. *Acta Metallurgica*, *37*(7), 1759–1771.

Daines, M., & Kohlstedt, D. L. (1993). A laboratory study of melt migration. *Philos T Roy Soc A*, *342*(1663), 43–52.

Daines, M., & Kohlstedt, D. L. (1994). The transition from porous to channelized flow due to melt/rock reaction during melt migration. *Geophys. Res. Lett.*, *21*(2), 145–148.

Daines, M., & Kohlstedt, D. L. (1997). Influence of deformation on melt topology in peridotites. *Journal of Geophysical Research-Solid Earth*, *102*(B5), 10257–10271.

Debacker, T., Seghedi, A., Belmans, M., & Sintubin, M. (2008). Contractional kink bands formed by stress deflection along pre-existing anisotropies? examples from .... *J Struct Geol*.

DellAngelo, L., & Tullis, J. (1988). Experimental deformation of partially melted granitic aggregates. *Journal of Metamorphic Geology*, *6*(4), 495–515.

Elthon, D. (1983). Isomolar and isostructural pseudo-liquidus phase-diagrams for oceanic basalts. *American Mineralogist*, *68*(5-6), 506–511.

Fischer, K. M., Ford, H. A., Abt, D. L., & Rychert, C. A. (2010). The lithosphere-asthenosphere boundary. *Annu Rev Earth Pl Sc*, *38*(1), 551–575.

Forsyth, D. W., Scheirer, D., Webb, S., Dorman, L., Orcutt, J., Harding, A., Blackman, D., Morgan, J., Detrick, R., Shen, Y., Wolfe, C., Canales, J., Toomey, D., Sheehan, A., Solomon, S., & Wilcock, W. (1998). Imaging the deep seismic structure beneath a mid-ocean ridge: The melt experiment. *Science*, *280*(5367), 1215–1218.

Gifkins, R. (1970). *Optical Microscopy of Metals*. Elsevier.

Gourlay, C., & Dahle, A. (2007). Dilatant shear bands in solidifying metals. *Nature*.

Hall, C., & Parmentier, E. (2000). Spontaneous melt localization in a deforming solid with viscosity variations due to water weakening. *Geophys. Res. Lett.*, *27*(1), 9–12.

Hier-Majumder, S., Leo, P., & Kohlstedt, D. L. (2004). On grain boundary wetting during deformation. *Acta Materialia*, *52*(12), 3425–3433.

Hier-Majumder, S., Ricard, Y., & Bercovici, D. (2006). Role of grain boundaries in magma migration and storage. *Earth and Planetary Science Letters*, *248*(3-4), 735–749.

Hirano, N., Takahashi, E., Yamamoto, J., Abe, N., Ingle, S. P., Kaneoka, I., Hirata, T., Kimura, J.-I., Ishii, T., Ogawa, Y., Machida, S., & Suyehiro, K. (2006). Volcanism in response to plate flexure. *Science*, *313*(5792), 1426–1428.

Hirth, G., & Kohlstedt, D. L. (1995a). Experimental constraints on the dynamics of the partially molten upper-mantle - deformation in the diffusion creep regime. *Journal of Geophysical Research-Solid Earth*, *100*(B2), 1981–2001.

Hirth, G., & Kohlstedt, D. L. (1995b). Experimental constraints on the dynamics of the partially molten upper-mantle .2. deformation in the dislocation creep regime. *Journal of Geophysical Research-Solid Earth*, *100*(B8), 15441–15449.

Hirth, G., & Kohlstedt, D. L. (1996). Water in the oceanic upper mantle: Implications for rheology, melt extraction and the evolution of the lithosphere. *Earth and Planetary Science Letters*, *144*(1-2), 93–108.

Hirth, G., & Kohlstedt, D. L. (2003). Rheology of the upper mantle and the mantle wedge: A view from the experimentalists. In J. Eiler (Ed.) *Inside the Subduction Factory, Geophysical Monograph 138*, (pp. 83–105). AGU, Washington, DC.

Holtzman, B. K., Groebner, N., Zimmerman, M. E., Ginsberg, S., & Kohlstedt, D. L. (2003). Stress-driven melt segregation in partially molten rocks. *Geochem Geophy Geosy*, *4*, 8607.

Holtzman, B. K., & Kohlstedt, D. L. (2007). Stress-driven melt segregation and strain partitioning in partially molten rocks: Effects of stress and strain. *Journal of Petrology*, *48*(12), 2379–2406.

Holtzman, B. K., Kohlstedt, D. L., & Morgan, J. (2005). Viscous energy dissipation and strain partitioning in partially molten rocks. *Journal of Petrology*, *46*(12), 2569–2592.

Hopper, J., & Buck, W. R. (1993). The initiation of rifting at constant tectonic force - role of diffusion creep. *Journal of Geophysical Research-Solid Earth*, *98*(B9), 16213–16221.

Hopper, J., & Buck, W. R. (1998). Styles of extensional decoupling. *Geology*, *26*(8), 699–702.

Hustoft, J., & Kohlstedt, D. L. (2006). Metal-silicate segregation in deforming dunitic rocks. *Geochem Geophy Geosy*, *7*, Q02001.

Johnson, K., & Dick, H. J. B. (1992). Open system melting and temporal and spatial variation of peridotite and basalt at the atlantis-ii fracture-zone. *Journal of Geophysical Research-Solid Earth*, *97*(B6), 9219–9241.

Johnson, K., Dick, H. J. B., & Shimizu, N. (1990). Melting in the oceanic upper mantle - an ion microprobe study of diopsides in abyssal peridotites. *J Geophys Res-Solid*, *95*(B3), 2661–2678.

Katz, R. F. (2008). Magma dynamics with the enthalpy method: Benchmark solutions and magmatic focusing at mid-ocean ridges. *Journal of Petrology*, *49*(12), 2099–2121.

Katz, R. F., Spiegelman, M., & Holtzman, B. K. (2006). The dynamics of melt and shear localization in partially molten aggregates. *Nature*, *442*(7103), 676–679.

Kawakatsu, H., Kumar, P., Takei, Y., & Shinohara, M. (2009). Seismic evidence for sharp lithosphere-asthenosphere boundaries of oceanic plates. *Science*.

Kelemen, P., Hirth, G., Shimizu, N., Spiegelman, M., & Dick, H. J. B. (1997). A review of melt migration processes in the adiabatically upwelling mantle beneath oceanic spreading ridges. *Philos T R Soc A*, *355*(1723), 283–318.

Kelemen, P. B., & Dick, H. J. B. (1995). Focused melt flow and localized deformation in the upper-mantle - juxtaposition of replacive dunite and ductile shear zones in the josephine peridotite, sw oregon. *Journal of Geophysical Research-Solid Earth*, *100*(B1), 423–438.

Kelemen, P. B., Whitehead, J., Aharonov, E., & Jordahl, K. (1995). Experiments on flow focusing in soluble porous-media, with applications to melt extraction from the mantle. *Journal of Geophysical Research-Solid Earth*, *100*(B1), 475–496.

King, D. S. H., Zimmerman, M. E., & Kohlstedt, D. L. (2010). Stress-driven melt segregation in partially molten olivine-rich rocks deformed in torsion. *Journal of Petrology*, *51*(1-2), 21–42.

Kirschner, D., & Teixell, A. (1996). Three-dimensional geometry of kink bands in slates and its relationship with finite strain. *Tectonophysics*.

Kohlstedt, D. L., & Holtzman, B. K. (2009). Shearing melt out of the earth: An experimentalist's perspective on the influence of deformation on melt extraction. *Annu Rev Earth Pl Sc*, *37*, 561–593.

Kohlstedt, D. L., & Zimmerman, M. E. (1996). Rheology of partially molten mantle rocks. *Annu Rev Earth Pl Sc*, *24*, 41–62.

Kohlstedt, D. L., Zimmerman, M. E., & Mackwell, S. J. (2010). Stress-driven melt segregation in partially molten feldspathic rocks. *Journal of Petrology*, *51*(1-2), 9–19.

Lundstrom, C., Gill, J., Williams, Q., & Perfit, M. (1995). Mantle melting and basalt extraction by equilibrium porous flow. *Science*, *270*(5244), 1958–1961.

McKenzie, D. (1984). The generation and compaction of partially molten rock. *Journal of Petrology*, *25*(3), 713–765.

Mei, S., Bai, W., Hiraga, T., & Kohlstedt, D. L. (2002). Influence of melt on the creep behavior of olivine-basalt aggregates under hydrous conditions. *Earth and Planetary Science Letters*, *201*(3-4), 491–507.

Mierdel, K., Keppler, H., Smyth, J. R., & Langenhorst, F. (2007). Water solubility in aluminous orthopyroxene and the origin of earth's asthenosphere. *Science*, *315*(5810), 364–368.

Morgan, Z., & Liang, Y. (2003). An experimental and numerical study of the kinetics of harzburgite reactive dissolution with applications to dunite dike formation. *Earth and Planetary Science Letters*, *214*(1-2), 59–74.

Morgan, Z., & Liang, Y. (2005). An experimental study of the kinetics of lherzolite reactive dissolution with applications to melt channel formation. *Contrib Mineral Petr*, *150*(4), 369–385.

Nicolas, A., & Boudier, F. (1995). Mapping oceanic ridge segments oman ophiolite. *Journal of Geophysical Research-Solid Earth*, *100*(B4), 6179–6197.

Ortoleva, P., Merino, E., Moore, C., & Chadam, J. (1987). Geochemical self-organization .1. reaction-transport feedbacks and modeling approach. *American Journal of Science*, *287*(10), 979–1007.

Parsons, R. A., Nimmo, F., Hustoft, J., Holtzman, B. K., & Kohlstedt, D. L. (2008). An experimental and numerical study of surface tension-driven melt flow. *Earth and Planetary Science Letters*, *267*(3-4), 548–557.

Paterson, M., & Olgaard, D. (2000). Rock deformation tests to large shear strains in torsion. *J Struct Geol*, *22*(9), 1341–1358.

Paterson, M. S. (1990). Rock deformation experimentation. In A. Duba, W. Durham, J. Handin, & H. Wang (Eds.) *The Brittle-Ductile Transition in rocks. The Heard Volume, American Geophysical Union Geophysical Monograph, 56.*, (pp. 187–194). AGU, Washington, DC.

Rabinowicz, M. (2004). Melt segregation under compaction and shear channeling: Application to granitic magma segregation in a continental crust. *J. Geophys. Res*, *109*(B4), 20.

Rabinowicz, M., & Toplis, M. J. (2009). Melt segregation in the lower part of the partially molten mantle zone beneath an oceanic spreading centre: Numerical modelling of the combined effects of shear segregation and compaction. *Journal of Petrology*, *50*(6), 1071–1106.

Rabinowicz, M., & Vigneresse, J. (2004). Melt segregation under compaction and shear channeling: Application to granitic magma segregation in a continental crust. *Journal of Geophysical Research-Solid Earth*, *109*(B4), B04407.

Riley, G., & Kohlstedt, D. L. (1991). Kinetics of melt migration in upper mantle-type rocks. *Earth and Planetary Science Letters*, *105*(4), 500–521.

Riley, G., Kohlstedt, D. L., & Richter, F. (1990). Melt migration in a silicate liquid-olivine system - an experimental test of compaction theory. *Geophys. Res. Lett.*, *17*(12), 2101–2104.

Rosenberg, C., & Handy, M. (2001). Mechanisms and orientation of melt segregation paths during pure shearing of a partially molten rock analog (norcamphorbenzamide). *J Struct Geol*, *23*, 1917–1932.

Rutter, E. (1997). The influence of deformation on the extraction of crustal melts: a consideration of the role of melt-assisted granular flow. In M. Holness (Ed.) *Deformation-enhanced Fluid Transport in the Earth's Crust and Mantle*, (pp. 82–110). Chapman & Hall.

Rutter, E., & Brodie, K. (1995). Mechanistic interactions between deformation and metamorphism. *Geol J*, *30*(3-4), 227–240.

Rutter, E., & Neumann, D. (1995). Experimental deformation of partially molten westerly granite under fluid-absent conditions, with implications for the extraction of granitic magmas. *Journal of Geophysical Research-Solid Earth*, *100*(B8), 15697–15715.

Rychert, C. A., & Shearer, P. M. (2009). A global view of the lithosphere-asthenosphere boundary. *Science*, *324*(5926), 495–498.

Saar, M., Manga, M., Cashman, K., & Fremouw, S. (2001). Numerical models of the onset of yield strength in crystal-melt suspensions. *Earth Planet Sc Lett*, *187*(3-4), 367–379.

Scott, D., & Stevenson, D. J. (1984). Magma solitons. *Geophys. Res. Lett.*, *11*(11), 1161–1164.

Scott, D., & Stevenson, D. J. (1986). Magma ascent by porous flow. *J Geophys Res-Solid*, *91*(B9), 9283–9296.

Scott, T., & Kohlstedt, D. L. (2006). The effect of large melt fraction on the deformation behavior of peridotite. *Earth and Planetary Science Letters*, *246*(3-4), 177–187.

Shaw, C., Thibault, Y., Edgar, A., & Lloyd, F. (1998). Mechanisms of orthopyroxene dissolution in silica-undersaturated melts at 1 atmosphere and implications for the origin of silica-rich glass in mantle xenoliths. *Contrib Mineral Petr*, *132*(4), 354–370.

Sims, K., DePaolo, D., Murrell, M., Baldridge, W., Goldstein, S., & Clague, D. (1995). Mechanisms of magma generation beneath hawaii and midocean ridges - uranium/thorium and samarium/neodymium isotopic evidence. *Science*, *267*(5197), 508–512.

Spiegelman, M. (1993). Flow in deformable porous-media .1. simple analysis. *J Fluid Mech*, *247*, 17–38.

Spiegelman, M. (1996). Geochemical consequences of melt transport in 2-d: The sensitivity of trace elements to mantle. *Earth and Planetary Science Letters*, *139*(1-2), 115–132.

Spiegelman, M. (2003). Linear analysis of melt band formation by simple shear. *Geochem Geophy Geosy*, *4*, 8615.

Spiegelman, M., Kelemen, P. B., & Aharonov, E. (2001). Causes and consequences of flow organization during melt transport: The reaction infiltration instability in compactible media. *Journal of Geophysical Research-Solid Earth*, *106*(B2), 2061–2077.

Spiegelman, M., & Kenyon, P. (1992). The requirements for chemical disequilibrium during magma migration. *Earth and Planetary Science Letters*, *109*(3-4), 611–620.

Stevenson, D. J. (1986). On the role of surface-tension in the migration of melts and fluids. *Geophys. Res. Lett.*, *13*(11), 1149–1152.

Stevenson, D. J. (1989). Spontaneous small-scale melt segregation in partial melts undergoing deformation. *Geophys. Res. Lett.*, *16*(9), 1067–1070.

Stewart, K., & Alvarez, W. (1991). Mobile-hinge kinking in layered rocks and models. *J Struct Geol*, *13*(3), 243–259.

Stolper, E. (1980). A phase-diagram for mid-ocean ridge basalts - preliminary-results and implications for petrogenesis. *Contrib Mineral Petr*, *74*(1), 13–27.

Suhr, G. (1999). Melt migration under oceanic ridges: Inferences from reactive transport modelling of upper mantle hosted dunites. *Journal of Petrology*, *40*(4), 575–599.

Tackley, P. (2000a). Self-consistent generation of tectonic plates in time-dependent, three-dimensional mantle convection simulations, 1. pseudoplastic yielding. *Geochem. Geophys. Geosyst*, *1*(8), 200GC000036.

Tackley, P. (2000b). Self-consistent generation of tectonic plates in time-dependent, three-dimensional mantle convection simulations 2. strain weakening and asthenosphere. *Geochem Geophy Geosy*, *1*, 2000GC00043.

Takei, Y., & Hier-Majumder, S. (2009). A generalized formulation of interfacial tension driven fluid migration with dissolution/precipitation. *Earth and Planetary Science Letters*, *288*(1-2), 138–148.

Takei, Y., & Holtzman, B. K. (2009a). Viscous constitutive relations of solid-liquid composites in terms of grain boundary contiguity: 1. grain boundary diffusion control model. *J. Geophys. Res.*, *114*, B06205.

Takei, Y., & Holtzman, B. K. (2009b). Viscous constitutive relations of solid-liquid composites in terms of grain boundary contiguity: 3. causes and consequences of viscous anisotropy. *J. Geophys. Res.*, *114*, B06207.

Toramaru, A., & Fujii, N. (1986). Connectivity of melt phase in a partially molten peridotite. *J Geophys Res-Solid*, *91*(B9), 9239–9252.

von Bargen, N., & Waff, H. (1986). Permeabilities, interfacial-areas and curvatures of partially molten systems - results of numerical computation of equilibrium microstructures. *J Geophys Res-Solid*, *91*(B9), 9261–9276.

Waff, H., & Bulau, J. (1979). Equilibrium fluid distribution in an ultramafic partial melt under hydrostatic stress conditions. *Journal of Geophysical Research*, *84*, 6209–6224.

Wark, D., & Watson, E. (1998). Grain-scale permeabilities of texturally equilibrated, monomineralic rocks. *Earth and Planetary Science Letters*, *164*(3-4), 591–605.

Webber, C., Newman, J., Iii, C. W. H., Little, T., & Tikoff, B. (2010). Fabric development in cm-scale shear zones in ultramafic rocks, red hills, new zealand. *Tectonophysics*, *489*(1-4), 55–75.

White, R., & Powell, R. (2002). Melt loss and the preservation of granulite facies mineral assemblages. *Journal of Metamorphic Geology*, *20*(7), 621–632.

Whitehead, J. (1987). A laboratory demonstration of solitons using a vertical watery conduit in syrup. *American Journal of Physics*, *55*(11), 998–1003.

Wiggins, C., & Spiegelman, M. (1995). Magma migration and magmatic solitary waves in 3-d. *Geophys. Res. Lett.*, *22*(10), 1289–1292.

Zimmerman, M. E., & Kohlstedt, D. L. (2004). Rheological properties of partially molten lherzolite. *Journal of Petrology*, *45*(2), 275–298.

Zimmerman, M. E., Zhang, S., Kohlstedt, D. L., & Karato, S. (1999). Melt distribution in mantle rocks deformed in shear. *Geophys. Res. Lett.*, *26*(10), 1505–1508.

Appendix A

A.1 Governing equations for surface tension driven flow

Mass conservation of the liquid and solid phases are given by

$$\frac{\partial(\rho_L \phi)}{\partial t} + \nabla \cdot (\rho_L \phi \mathbf{v}^L) = \Gamma \tag{A.1}$$

$$\frac{\partial(\rho_S (1-\phi))}{\partial t} + \nabla \cdot (\rho_S (1-\phi) \mathbf{v}^S) = -\Gamma \tag{A.2}$$

where Γ (kg/m^3/s) is the mass exchange rate between solid and liquid due to dissolution/precipitation (dissolution positive), ρ_S and ρ_L are the solid and liquid densities, $\mathbf{v}^L$ and $\mathbf{v}^S$ are the solid and liquid velocities, and ϕ is the liquid volume fraction.

Mass conservation of component A is given by

$$\frac{\partial(\rho_L c \phi)}{\partial t} + \nabla \cdot (\rho_L c \phi \mathbf{v}^L) = -\nabla \cdot (\phi \mathbf{J}) + \Gamma \tag{A.3}$$

where c is the concentration of component A in the liquid phase and the density of diffusive flux of component A in the liquid phase is given by

$$\mathbf{J} = -\rho_L D_L \nabla c \tag{A.4}$$

When interfacial tension, γ_{sl}, exists the pressure field is discontinuous at the solid-liquid interface. This discontinuity p (in Pa) for a medium in which grains are in contact is given by

$$p = \frac{2\gamma_{sl}}{r} \tag{A.5}$$

where r represents the mean curvature radius (positive when center of radius of curvature is on the solid side of the interface).

$$r = \frac{2\phi^{1/2}d}{f(\theta)} \tag{A.6}$$

where d is the grain size, θ is the dihedral angle, and $f(\theta)$ is given by

$$f(\theta < \frac{\pi}{3}) = \left[8\cos\frac{\phi}{2}\sin(\frac{\pi}{6} - \frac{\phi}{2}) - 2\sqrt{3}(\frac{\pi}{3} - \phi)\right]^{\frac{1}{2}}. \tag{A.7}$$

Substituting (A.6) into (A.5) gives

$$p = \frac{\gamma_{sl} f(\theta)}{\phi^{1/2} d} \tag{A.8}$$

Momentum conservation of liquid and solid are given by

$$0 = -\nabla(\phi P^L) + \phi\rho_L \mathbf{g} - \frac{\eta_L \phi^2}{k_\phi}(\mathbf{v}^L - \mathbf{v}^S) + P^L \nabla\phi \tag{A.9}$$

$$0 = -\nabla[(1-\phi)\sigma^s_{ij}] + (1-\phi)\rho_S \mathbf{g} - \frac{\eta_L \phi^2}{k_\phi}(\mathbf{v}^L - \mathbf{v}^S) + (P^L + p)\nabla\phi \tag{A.10}$$

where P^L and σ^S_{ij} are liquid pressure and solid stress, k_ϕ is permeability, η_L is liquid viscosity, and $\mathbf{g}$ is gravitational acceleration. The viscous constitutive relation for the solid framework is given by

$$\dot{\varepsilon}_{ij} = \frac{1}{3\xi}\left(\frac{\sum_k \sigma^S_{kk}}{3} + P^L + p\right) + \frac{1}{2\eta}\left(\sigma^S_{ij} - \frac{\sum_k \sigma^S_{kk}}{3}\delta ij\right) \tag{A.11}$$

where $\dot{\varepsilon}_{ij}$ is the strain rate tensor, ξ is the bulk viscosity, and η is the shear viscosity.

The dissolution/precipitation rate Γ is taken to be linearly dependent upon the driving force resulting from the chemical potential difference,

$$\Gamma = -K\left[\mu^L_A(P^L, T, c) - \mu^S_A(P^L + p, T)\right] \tag{A.12}$$

where K is a constant that is taken to be infinitely high, so that Equation A.11 becomes

$$\mu^L_A(P^L, T, c) = \mu^S_A(P^L + p, T) \tag{A.13}$$

Let c_0 be the equilibrium concentration of component A in the liquid with a planar solid-liquid interface ($r \to \infty, p = 0$), then

$$\mu^L_A(P^L, T, c_0) = \mu^S_A(P^L, T) \tag{A.14}$$

If $|c - c_0|/c_0 << 1$, then

$$\mu_A^L(P^L, T, c) = \mu_A^{L_0}(P^L, T) + RT \ln a(c) \tag{A.15}$$

where $a(c)$ is an activity of component A in the liquid phase, which is a function of c.

$$\mu_A^S(P^L + p, T) = \mu_A^S(P^L, T) + p\Omega \tag{A.16}$$

where Ω (m^3/mol) is the molar volume of component A in the solid phase. We then obtain

$$c = c_0 \left(1 + \frac{p(\phi)\Omega}{E}\right) \tag{A.17}$$

where E is a constant defined by

$$E = RT \left(\frac{c_0}{a(c_0)} \frac{da}{dc}|_{c_0}\right). \tag{A.18}$$

A.2 Dependence of viscosity upon melt fraction

Equation A.10 requires a formulation for the shear and bulk viscosities of the solid phase. In Chapter 3, we use a constant shear viscosity and a bulk viscosity that depends upon melt fraction given non-dimensionally by

$$\xi^* = \frac{1}{\phi^2} \tag{A.19}$$

similar to that used by Spiegelman et al. (2001) and others.

This formulation is a slight variation to that used by Takei & Hier-Majumder (2009) in which the shear viscosity of the solid is taken to be a function of melt fraction, and a different form of melt fraction dependence is used for the bulk viscosity. The empirically-determined exponential dependence of shear viscosity on melt fraction is used, and the non-dimensional bulk viscosity is some multiple of the shear viscosity.

$$\begin{cases} \eta^* = e^{-\Lambda\phi} \\ \xi^* = \alpha e^{-\Lambda\phi} \end{cases} \tag{A.20}$$

In this formulation the characteristic length scale L is given by

$$L = \left(\frac{\eta_0(\xi_0^* + \frac{4}{3}\eta_0^*)k_0}{\eta_L}\right)^{\frac{1}{2}} \tag{A.21}$$

and the characteristic velocity v_o is defined by

$$v_0 = \frac{\gamma_{\rm sl}}{d}\frac{L}{\eta_0}. \tag{A.22}$$

A.3 First-order growth rate of perturbations

In solving set of equations, the constant reference melt fraction ϕ_0 is perturbed to obtain (for a case in which buoyancy is neglected)

$$\phi = \phi_0 + \epsilon\tilde{\phi}e^{\lambda^* t^*}e^{-ik^* x^*} \quad (\epsilon << 1) \tag{A.23}$$

(Takei & Hier-Majumder, 2009, Equation 37) where t^* is nondimensional time and $t = t^*\frac{v_0}{L}$. In the full numerical solution, ϵ is solved at each time step, but we can obtain a first order approximation of the growth rate of a perturbation without solving the full set of equations by taking ϵ to be constant.

At time $t = 0$, Equation A.15 becomes

$$\phi|_{t_0} = \phi_0 + \epsilon\tilde{\phi}e^{-ik^* x^*}. \tag{A.24}$$

The differential melt fraction $\Delta\phi$ is given by

$$\Delta\phi = \frac{\phi_{max} - \phi_{min}}{\phi^0_{max} - \phi^0_{min}}. \tag{A.25}$$

Solving Equation **??** at any given time gives

$$\Delta\phi = \frac{\phi_0 + \epsilon\tilde{\phi}e^{\lambda^* t^*}e^{-ik^* x^*} - \phi_0}{\phi_0 + \epsilon\tilde{\phi}e^{-ik^* x^*} - \phi_0} = e^{\lambda^* t^*}. \tag{A.26}$$

The first order growth rate

$$\Delta\phi = e^{\lambda^* t^*}. \tag{A.27}$$

is used in Chapter 3 in the analysis of the perturbation wavelength that best fits the experimental data and in extrapolating dissipation rate to geologically relevant time scales.